

MERIS ATBD 2.6

Case II.S Bright Pixel Atmospheric Correction

Document change log

Version	Date	Authors	Change
4.1	18.02.2000	Jim Aiken, Gerald Moore (PML)	MERIS 1 st and 2 nd reprocessing version
5.0	30.06.2011	Gerald Moore (Bio-Optika), Samantha Lavender (Argans)	MERIS 3 rd reprocessing version with new marine model
5.1	15.07.2014	Gerald Moore (Bio-Optika), Constant Mazeran (Solvo), Jean-Paul Huot (ESA)	Updated numerical inversion
5.2	28.09.2015	Gerald Moore (Bio-Optika), Constant Mazeran (Solvo), Jean-Paul Huot (ESA)	Update of first guess retrieval and input uncertainty of the χ^2 minimisation
5.3	31.03.2017	Gerald Moore (Bio-Optika), Constant Mazeran (Solvo), Jean-Paul Huot (ESA)	MERIS 4 th reprocessing version: Handling of the smile and pressure correction, updated Case2_S threshold.

Table of Contents

1. Introduction	10
2. Algorithm Overview.....	10
3. Algorithm Description.....	11
3.1 Theoretical Description	11
3.1.1 Hydrological Model	11
3.1.2 Implementation of the Hydrological Model.....	14
3.1.3 Atmospheric model	15
3.2 Hydrological Model Parameters.....	17
3.2.1 Pure Water Absorption.....	17
3.2.2 Pure Water Scattering	19
3.2.3 Particulate Absorption.....	19
3.2.4 Particulate Scattering	20
3.3 Model Sensitivity.....	20
3.3.1 Similarity and Optimal Band Choice	20
3.3.2 Temperature and Smile	22
3.3.3 MERIS radiometric sensitivity and Aerosol retrieval error.....	23
3.4 Pre-processing	25
3.4.1 Rayleigh correction and smile effect	25
3.4.2 Optional temperature and Smile Offsets	25
3.4.3 Choice of IOPs.....	25
3.5 Inversion	27
3.5.1 Strategy for numerical inversion	27
3.5.2 χ^2 minimisation	35
3.5.3 Final marine reflectance output.....	40
3.5.4 Input uncertainty estimate.....	40
3.5.5 First guess retrieval.....	42

3.5.6	Determination of bb from $\rho_w(\lambda)$	49
3.6	Validation	49
3.6.1	Numerical check against simulated data.....	49
3.6.2	Visual inspection over MERIS scenes.....	51
3.6.3	Validation against in-situ data	61
3.6.4	Discussion	68
4.	Parameter Description	69
4.1.1	Error Budget Estimates.....	69
4.1.2	Practical Considerations	70
4.1.3	Sensitivity to IOPs	70
4.1.4	Output Product.....	70
4.1.5	Derived flags	70
5.	Assumptions and Limitations	72
6.	Acknowledgements	73
7.	References	74
8.	Appendix A - Chlorophyll Absorbance and Fluorescence	77

Figures

Figure 1: The (a) relationship between suspended sediment and reflectance and (b) relationship between the reciprocals of suspended sediment and reflectance. Data taken from Lavender (2006).12

Figure 2: F' vs. η and $bb/(a+bb)$14

Figure 3: Variation in Water absorption from literature.....18

Figure 4: Temperature dependence of water absorption19

Figure 5: Reflectance saturation - Severn Estuary20

Figure 6: Similarity spectrum for low band set21

Figure 7: Similarity spectrum for high band set.....22

Figure 8: Sensitivity to Temperature - low band set.....22

Figure 9: Sensitivity to 1 nm smile low band set.....23

Figure 10: MERIS Counts vs. sediment load24

Figure 11: Aerosol retrieval errors vs. MERIS Counts24

Figure 12: White scatter Flag26

Figure 13: Comparative scattering in Severn Estuary and Barents Sea27

Figure 14 Validation of marine reflectance at AAOT with MERIS 3rd reprocessing when vicarious calibration is deactivated.....28

Figure 15 Validation of marine reflectance at AAOT with MERIS 3rd reprocessing when activating the NIR vicarious calibration29

Figure 16 Sensitivity of the TOA signal $\rho_{RC\lambda}$ to a relative change $\Delta\tau\lambda_0\tau\lambda_0$ of +100% around $\tau\lambda_0=0.1$ and $f\omega\alpha=0.8$, for several sediment concentrations (colours). Air mass is 2.431

Figure 17 Sensitivity of the TOA signal $\rho_{RC\lambda}$ to a relative change of +100% respectively on $\Delta b_{bp\lambda_0} b_{bp\lambda_0}$ (top left), on ΔS_{bSb} (top right), on $\Delta a_p * \lambda_{0ap} * \lambda_0$ (bottom left) and ΔS_{aSa} (bottom right) for several sediment concentrations from 0 to 100 g/m³ (colours). Air mass is 2.434

Figure 18 Water vapour transmittance at 709 nm over Rio de la Plata, as from MERIS 3rd reprocessing41

Figure 19 Multiple-minima issue of the 3-band iterative scheme over a turbid pixel. Blue curves displays χ^2 constructed by 3 bands (709, 779, 865) as function of TSM. Red curve is the associated aerosol content at 779 nm.43

Figure 20 Domain of validity of $\rho_{a\lambda}$, in grey, as a function of wavelength, in log/log scale, due to bounds in $\rho_{a\lambda 0}$ and α44

Figure 21 Range of admissible TSM (x-axis) found by the first guess retrieval for a clear pixel (left) and a turbid pixel (right). Blue curve represents the χ^2 on five bands as function of TSM, red curves is the associated aerosol signal. Grey dots is the first guess value, averaged from TSM extrema. Blue and red dots correspond to the χ^2 minimum.....45

Figure 22 Comparison of retrieved marine reflectance (y-axis) with reference reflectance (x-axis) at 779 nm for simulated TOA spectra perfectly fitting the model. Color is TSM (from blue 10^{-2} to brown 100 g/m^3). Rows from top to bottom are respectively for $\alpha=-0.5, -1.5, -2.5$ and columns from left to right are respectively for $\rho_{a\lambda 0}=0.005, 0.08, 0.15$ 50

Figure 23 Angstrom exponent over the Mediterranean Sea with standard 3rd reprocessing BPAC (top) and present evolution (bottom), without vicarious calibration (left) and with NIR vicarious calibration (right)52

Figure 24 Marine reflectance at 443 nm over the Mediterranean Sea with standard 3rd reprocessing BPAC (top) and present evolution (bottom), without vicarious calibration (left) and with NIR vicarious calibration (right) ..53

Figure 25 Chlorophyll_1 concentration over the Mediterranean Sea with standard 3rd reprocessing BPAC (top) and present evolution (bottom), without vicarious calibration (left) and with NIR vicarious calibration (right) ..54

Figure 26 Angstrom exponent over the English Channel/Brittany with standard 3rd reprocessing BPAC (top) and present evolution (bottom), without vicarious calibration (left) and with NIR vicarious calibration (right) ..55

Figure 27 Chlorophyll_1 concentration over the English Channel/Brittany with standard 3rd reprocessing BPAC (top) and present evolution (bottom), without vicarious calibration (left) and with NIR vicarious calibration (right).....56

Figure 28 Marine reflectance at 443 nm over the English Channel/Brittany with standard 3rd reprocessing BPAC (top) and present evolution (bottom), without vicarious calibration (left) and with NIR vicarious calibration (right).....57

Figure 29 Angstrom exponent over the Amazon River with standard 3rd reprocessing BPAC (top) and present evolution (bottom), without vicarious calibration (left) and with NIR vicarious calibration (right).....58

Figure 30 Marine reflectance at 443 nm over the Amazon River with standard 3rd reprocessing BPAC (top) and present evolution (bottom), without vicarious calibration (left) and with NIR vicarious calibration (right)59

Figure 31 Chlorophyll_1 concentration over the Amazon River with standard 3rd reprocessing BPAC (top) and present evolution (bottom), without vicarious calibration (left) and with NIR vicarious calibration (right)60

Figure 32 Validation of marine reflectance at AAOT with new implementation when vicarious calibration is deactivated.....62

Figure 33 Validation of marine reflectance at AAOT with new implementation when activating NIR vicarious calibration63

Figure 34 Validation of marine reflectance at MOBY, BOUSSOLE and AAOT with 3rd reprocessing implementation when vicarious calibration is deactivated64

Figure 35 Validation of marine reflectance at MOBY, BOUSSOLE and AAOT with 3rd reprocessing implementation when activating NIR vicarious calibration65

Figure 36 Validation of marine reflectance at MOBY, BOUSSOLE and AAOT with new implementation when vicarious calibration is deactivated.....66

Figure 37 Validation of marine reflectance at MOBY, BOUSSOLE and AAOT with new implementation when activating NIR vicarious calibration.....67

Figure 38 Example of BPAC inversion over the South Pacific Gyre. Top left: RGB image of the Level-1 data. Top right: water vapour transmittance at 709 nm. Bottom: TSM retrieved by 3rd (left) and 4th (right) reprocessing BPAC.....71

Figure 39 TSM computed by 4th reprocessing BPAC over the MOBY (left) and BOUSSOLE (right) sites. Colours depict the 4th reprocessing flags (see legend).72

Figure 40: Chlorophyll fluorescence and absorption for MERIS Bands.....77

Figure 41: Effects of natural fluorescence on BPAC78

Tables

Table 1: Fluorescence height and phytoplankton absorption79

Nomenclature

Δ_ϕ	Sun-sensor viewing azimuth difference	degrees
λ	Wavelength	nm
θ_v	Sensor viewing zenith angle (the satellite “look angle”)	degrees
θ_s	Solar zenith angle	degrees
ρ	Fresnel reflectance at normal incidence	dimensionless
ρ_a	Multiple scattering aerosol reflectance	dimensionless
ρ_{as}	Single scattering aerosol reflectance	dimensionless
ρ_g	Reflectance due to sun glitter	dimensionless
ρ_r	Rayleigh reflectance	dimensionless
ρ_{ra}	Reflectance due to Rayleigh-aerosol interaction	dimensionless
ρ_t	Top of atmosphere reflectance	dimensionless
ρ_w	Water reflectance (above surface)	dimensionless
$\tilde{\rho}$	Fresnel reflectance for sun and sky irradiance	dimensionless
τ_{oz}	Ozone optical thickness	m^{-1}
τ_{wv}	Water vapour optical thickness	m^{-1}
τ_r	Rayleigh optical thickness	m^{-1}
a	Total absorption coefficient	m^{-1}
a_{bb}^*	Sediment absorption to backscatter ratio	dimensionless
a_p	Combined (phytoplankton, detritus, sediment and gelbstoff) absorption coefficient	m^{-1}
a_s	Particulate specific absorption	m^{-1}
a_w	Water absorption coefficient	m^{-1}
b	Total scattering coefficient	m^{-1}
bb	Total backscattering coefficient	m^{-1}
bb_p	Particulate (phytoplankton, detritus and sediment) backscattering coefficient	m^{-1}
bb_w	Water scattering coefficient	m^{-1}
\tilde{b}	Particulate backscattering ratio	dimensionless
c	Variable given in Gordon and Wang (1994)	dimensionless
f	Empirical factor relating IOPs to R	dimensionless
f'	Empirical factor relating IOPs to R	dimensionless

F	Empirical factor relating IOPs to ρ_w	dimensionless
F'	Empirical factor relating IOPs to ρ_w	dimensionless
n_w	Refractive index of seawater	dimensionless
r	Air-water reflectance for diffuse irradiance	dimensionless
t	Total (direct+diffuse) atmospheric transmittance	dimensionless
Q	Ratio of upwelling irradiance to radiance	dimensionless
R	Irradiance reflectance	dimensionless

1. Introduction

The successful exploitation of remotely sensed water colour observations requires the development of atmospheric correction methods in coastal waters, and the determination of total suspended matter (TSM) concentrations in gravimetric units for use in mass flux studies and hydrodynamic models. By definition, Case I waters (stratified shelf seas and the deep ocean) are coloured by biogenic materials alone (phytoplankton, its pigments, dissolved organic exudates and detritus). Coastal waters are usually termed Case II because the major influence on the water colour is TSM (primarily tidally stirred sediments or riverine fluvial muds) or gelbstoff (yellow substances). Gelbstoff is mainly dissolved coloured organic material (CDOM), consisting of humic and flavic compounds of terrestrial origin that are transported into marine waters by river/estuary systems.

With even modest concentrations of TSM ($>0.2 \text{ g m}^{-3}$), there is significant backscatter that results in reflectance at near infra-red wavelengths (NIR) that negates the 'dark pixel' atmospheric correction (AC) procedures, which assume zero water leaving at NIR wavelengths ($> 700 \text{ nm}$). These are termed 'bright pixel' waters and require a modified bright pixel atmospheric correction (BPAC). In addition, when phytoplankton such as coccolithophores are abundant the water can also be highly reflective (at visible and NIR wavelengths) due to backscatter from detached coccoliths and the BPAC is also invoked. Very high concentrations of any phytoplankton particles will also give significant backscatter and again the BPAC will be required to correct for the resultant NIR reflectance.

Gelbstoff has little effect on the atmospheric correction ('dark pixel'), as it primarily absorbs due to its dissolved nature, but Case 2 algorithms are needed for the retrieval of the concentrations of gelbstoff and other optically active components of the water such as TSM and chlorophyll-a (Chl-a).

2. Algorithm Overview

In waters dominated by sediment there is significant water leaving radiance at both visible and NIR wavelengths. An AC based on the concept of zero NIR water leaving radiance (dark pixel model) will fail because the extrapolation of aerosol path reflectance into visible bands will result in apparent negative reflectance at visible wavelengths; overcorrection due to an overestimation of the aerosol scattering.

The conventional AC procedures that were applied to CZCS and SeaWiFS (e.g. Antoine and Morel, 1991 and Gordon and Wang, 1994) assumed a dark pixel; zero NIR water reflectance. To undertake the bright pixel component SeaWiFS initially used an iterative method (Siegel *et al.* 2000) to correct for non-negligible water reflectance in the NIR arising from moderate to high phytoplankton abundances (chlorophyll concentrations greater than $\sim 2 \text{ mg m}^{-3}$) and so independent research was applied to correct for the effects of TSM (e.g. Ruddick *et al.* 2000 and Lavender *et al.* 2005), but the processing software has now been updated so that it takes non-phytoplankton scattering (Arnone *et al.* 1998) into account for both MODIS and SeaWiFS (Stumpf *et al.* 2002). In addition, research has investigated longer wavelengths where the water signal can still be assumed to be negligible (Wang and Shi, 2005).

The MERIS BPAC assumes there is significant water reflectance, as detected by the Case II.S Turbid Water flag ATBD 2.5, and partitions the top of the atmosphere reflectance, ρ , into components due to aerosols and in-water

particles (TSM) using a coupled hydrological and atmospheric model. The hydrological model assumes that the surface water reflectance, $\rho_w(\theta_s, \theta_v, \Delta\phi)$, can be determined by the absorption of water together with the absorption and scattering of particles. Reflectance has an angular dependence described by the solar zenith angle (θ_s), viewing zenith angle (θ_v) and difference (solar versus viewing) in the azimuth angles ($\Delta\phi$).

The atmosphere is modelled using a simple single scattering model, which assumes that the atmospheric path radiance and absorption can be separated into the Rayleigh and aerosol components. The aerosol component is modelled by a simple angstrom exponent.

3. Algorithm Description

3.1 Theoretical Description

3.1.1 Hydrological Model

The hydrological optics depends on the inherent optical properties (IOPs) of the TSM, which varies according to wavelength (λ). Parameterisation of reflectance for waters dominated by TSM involves knowledge of three IOPs and their spectral properties: particulate specific absorption, $a_s(TSM, \lambda)$; particulate specific scattering, $b_s(TSM, \lambda)$; particulate backscattering ratio, \tilde{b} . The sensitivity of these IOPs with regard to sediment type has been investigated, under laboratory conditions, using measurements of reflectance with a spectroradiometer above a 2m depth tank (Bale *et al.*, 1994). The tank depth simulated optically deep water, as pure water at NIR wavelengths has a high attenuation coefficient; 1.53 m^{-1} at 700 nm and 0.20 m^{-1} at 865 nm.

Figure 1a shows the relationship between reflectance and TSM (termed Suspended Particulate Matter, SPM, in Lavender 2006) for sediments collected around the UK (primarily the east and south coasts). The reflectance shows high variation between sediment types, but each curve shows a non-linear relationship between sediment concentration and reflectance. Figure 1b shows the relationship between the reciprocal of sediment concentration and the reciprocal of remote sensed reflectance. It can be observed that this is a quasi-linear within relationship. This relationship can be explored further by considering the theoretical relationship with reflectance, $\rho_w(\theta_s, \theta_v, \Delta\phi)$, expressed as:

$$\rho_w = \pi \Re \frac{f(\theta_s, \theta_v, \Delta\phi)}{Q(\theta_s, \theta_v, \Delta\phi)} \left(\frac{bb_w + bb_{pds}}{a_w + a_{pds}} \right)$$

(1a)

or alternatively:

$$\rho_w = \pi \Re \frac{f'(\theta_s, \theta_v, \Delta\phi)}{Q(\theta_s, \theta_v, \Delta\phi)} \left(\frac{bb_w + bb_p}{a_w + a_p + bb_w + bb_p} \right) \quad (1b)$$

Where \Re is defined as:

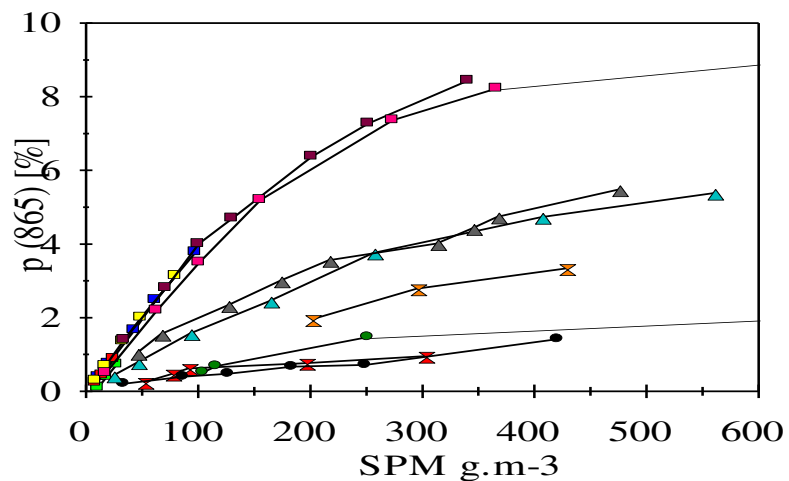
$$\mathfrak{R} = \left[\frac{(1 - \rho)(1 - \tilde{\rho})}{n_w^2} \right] \quad (2)$$

n_w is the refractive index of seawater, ρ is the Fresnel reflectance at normal incidence, $\tilde{\rho}$ is the Fresnel reflectance for sun and sky irradiance, r is the air-water reflectance for diffuse irradiance; these reflectances are dependent on the sea state for which wind speed is taken as a proxy.

Q is the ratio of upwelling irradiance to radiance, while f and f' are quasi constants for case 1 waters; all of these are dependent on the viewing geometry.

a_w , bb_w are the absorption and backscatter of water, bb_p is the combined backscatter of phytoplankton, detritus and sediment; a_p is the combined absorption of phytoplankton, detritus, sediment and gelbstoff (CDOM).

a)



b)

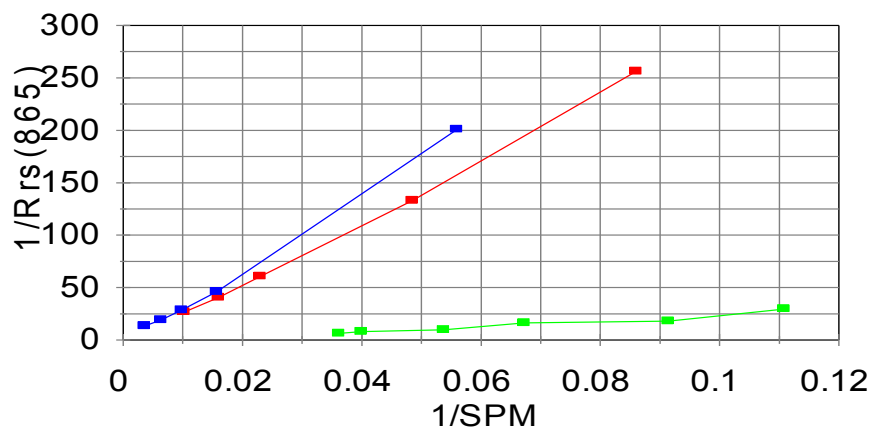


Figure 1: The (a) relationship between suspended sediment and reflectance and (b) relationship between the

reciprocals of suspended sediment and reflectance. Data taken from Lavender (2006).

If a fixed viewing geometry and wind speed are chosen the (1a) and (1b) can be expressed as:

$$\rho_w = F \left(\frac{bb_w + bb_p}{a_w + a_p} \right) \quad (3a)$$

$$\rho_w = F' \left(\frac{bb_w + bb_p}{a_w + a_p + bb_w + bb_p} \right) \quad (3b)$$

F and F' are functions that include the terms Q , \mathfrak{R} and π and imply geometry. Both bb/a and $bb/(a+bb)$ are variants of the f factor have been used in a hydro-optical modelling with the latter preferred for case 2 waters.

As the BPAC aims to include waters with very high turbidities and thus reflectances. The limiting values for these alternative reflectance expressions are important in terms of numerical stability. For a non or very low absorbing sediment, such as coccoliths, the limits are:

$$\lim_{bb_{pds} \rightarrow \infty} F \left(\frac{bb_w + bb_p}{a_w + a_p} \right) = \infty \quad \text{and} \quad \lim_{bb_{pds} \rightarrow \infty} F' \left(\frac{bb_w + bb_p}{a_w + a_p + bb_w + bb_p} \right) = F' \quad (4a,b)$$

Thus, the $bb/(a+bb)$ variant is more useable since it provides a defined limiting reflectance of F' for high reflectance waters, which can be used as an error check for computing look-up tables (LUT's) and for their implementation.

The limit for absorbing sediment is also of interest. Here, a_{bb}^* is defined as the specific absorption of the sediment backscatter, or the absorption to backscatter ratio, for a particular sediment and in this case (3b) becomes:

$$\rho_w = F' \left(\frac{bb_w + bb_p}{a_w + bb_w + bb_p (1 + a_{bb}^*)} \right) \quad (5)$$

And the limiting value becomes:

$$\lim_{bb_{pds} \rightarrow \infty} F' \left(\frac{bb_w + bb_p}{a_w + bb_w + bb_p (1 + a_{bb}^*)} \right) = \frac{F'}{(1 + a_{bb}^*)} \quad (6)$$

This limit permits the estimation of sediment absorption from above water reflectance in tank experiments and highly turbid water where analytical and *in-situ* methods may be problematic.

3.1.2 Implementation of the Hydrological Model

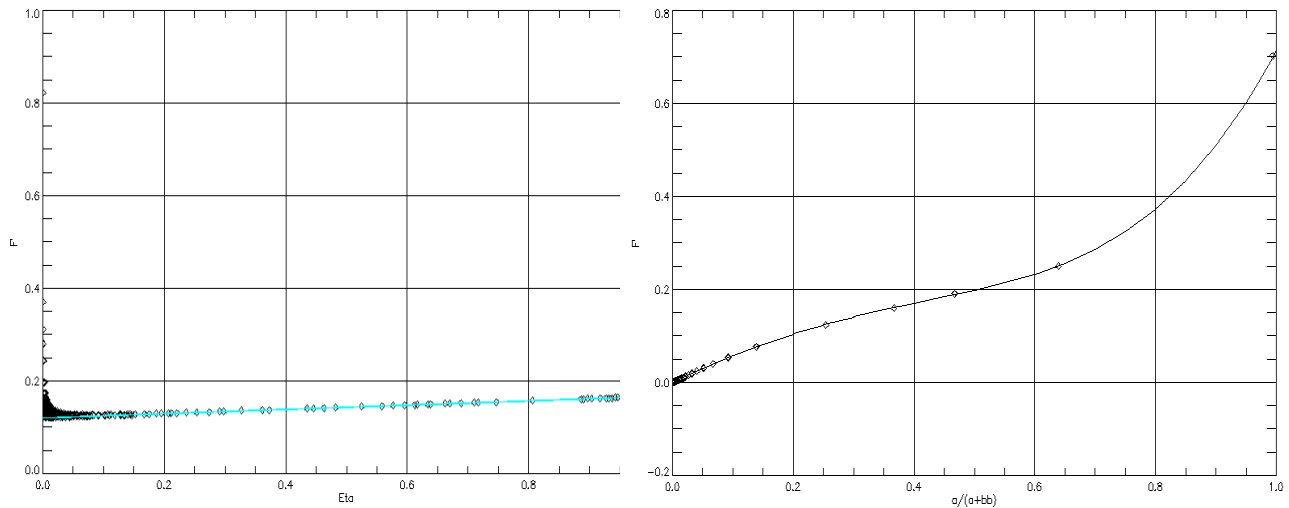
The F' values were computed using Hydrolight 3.0 (Mobley, 1995). The refractive index used was as specified in the MERIS RMD (MERIS Reference Model Document (RMD): Third Reprocessing, PO-TN-MEL-GS-0026), as were the phase functions of pure water and particles. The tables were run for four wind speeds (0.25 ms^{-1} , 1.00 ms^{-1} , 2.75 ms^{-1} and 5.00 ms^{-1}) corresponding to sea-state values recorded in MERMAID (MERIS MAtchup In-situ Database, <http://hermes.acri.fr/mermaid/home/home.php>) metadata, and for solar angles (θ_s) of 0, 15, 30, 45 and 60 degrees that encompasses the MERIS useful viewing geometry. θ_v and $\Delta\phi$ are implicit in the Hydrolight runs and the ‘quads’ were set to give the following viewing geometry:

$$\theta_v = \{0,15,30,45,60\}$$

$$\Delta\phi = \{0,15,30,45,60,75,90,105,120,135,150,165,180\}$$

The absorption values were run from a range of a_w values that were below the minimum found in literature, when adjusted for smile and temperature effects, and to the similar greatest value. Thereafter, a log ramp was applied to an absorption value of 30.0 m^{-1} . From the absorption, scattering values were calculated according to a ramp of single scattering albedo (ω) from zero to 0.9999 with the highest density of values at the high ω . In all, for each band around 10,000 table runs were computed according to the number of candidate a_w values. The f' determined from the Hydrolight runs was then fitted to η , where:

$$\eta = \frac{bb_w}{bb_w + bb_p} \tag{7}$$



a) Relationship between F' and η

b) Relationship between F' and $bb/(a+bb)$

Figure 2: F' vs. eta and $bb/(a+bb)$

The relationship with η proved to be linear for low turbidities (Figure 2). The residuals from the fit to η , were expected to relate to ω from previous work on Case I waters (Morel and Gentili, 1993). This however proved unsuccessful, and instead a polynomial relationship was fitted with F' being a function of $bb/(a+bb)$.

Thus for any view geometry F' can be expressed as:

$$F' = A0 + C \cdot \eta + \sum a_i \{bb/(a+bb)\}^i \quad (8)$$

where $A0$ and C are the linear coefficients for η , and a_i represents the coefficients of a 4th order polynomial. The F' factors are provided as LUTs containing the polynomials for each band, based on wind speed and viewing geometry, with the terms varying slowly so that a simple nearest neighbour lookup is sufficient.

3.1.3 Atmospheric model

For the basic AC the total reflectance at the top of the atmosphere can be written as:

$$\rho_t(\lambda) = \rho_r(\lambda) + \rho_a(\lambda) + \rho_{ra}(\lambda) + \rho_g(\lambda) + t \cdot \rho_w(\lambda) \quad (8)$$

Where $\rho_r(\lambda)$ is the Rayleigh scattering reflectance, $\rho_a(\lambda)$ is the aerosol scattering reflectance, $\rho_{ra}(\lambda)$ is the reflectance resulting from the interaction of $\rho_r(\lambda)$ and $\rho_a(\lambda)$, $\rho_g(\lambda)$ is the sun glitter and t is the total atmospheric transmission (direct+diffuse, downward+upward). If data are screened for sun glint, the term $\rho_g(\lambda)$ can be ignored. In the CZCS approximation, the term $\rho_{ra}(\lambda) + \rho_a(\lambda)$ can be approximated by the single scattering approximation $\rho_{as}(\lambda)$. Equation (8) thus becomes:

$$\rho_t(\lambda) = \rho_r(\lambda) + \rho_{as}(\lambda) + t \cdot \rho_w(\lambda) \quad (9)$$

In Case I waters the term $t \cdot \rho_w(\lambda_{NIR})$, NIR water reflectance at the satellite, becomes zero. The term $\rho_r(\lambda_{NIR})$ can be calculated and thus the term $\rho_{as}(\lambda_{NIR})$ determined. Given two wavebands in the NIR it's possible to extrapolate $\rho_{as}(\lambda)$ using either the conventional Angstrom exponent or a variable c given in Gordon and Wang (1994). Gordon and Wang (1994) indicated that the c extrapolation provides a superior fit for the SeaWiFS bands. In both these cases:

$$\varepsilon_{as}(\lambda_{NIR}(1), \lambda_{NIR}(2)) = \rho_{as}(\lambda_{NIR}(1)) / \rho_{as}(\lambda_{NIR}(2)) \quad (10)$$

is used to calculate either c or the Angstrom exponent, α , where:

$$\alpha = \ln[\varepsilon_{as}(\lambda_{NIR}(1), \lambda_{NIR}(2))] / \ln[\lambda_{NIR}(1) / \lambda_{NIR}(2)] \quad (11)$$

or

$$c = \ln[\varepsilon_{as}(\lambda_{NIR}(1), \lambda_{NIR}(2))] / [\lambda_{NIR}(1) / \lambda_{NIR}(2)] \quad (12)$$

In the case of the Angstrom exponent, $\rho_w(\lambda)$ is calculated as:

$$\rho_w(\lambda) = [\rho_t(\lambda) - \rho_r(\lambda) - \rho_{as}(\lambda_{NIR}(2)) \cdot (\lambda/\lambda_{NIR}(2))^\alpha] / t \quad (13)$$

and in the case of c , $\rho_w(\lambda)$ is calculated as:

$$\rho_w(\lambda) = \{\rho_t(\lambda) - \rho_r(\lambda) - \rho_{as}(\lambda_{NIR}(2)) \cdot \exp[c(\lambda/\lambda_{NIR}(2))]\} / t \quad (14)$$

Note that other modelling of the aerosol residual $\rho_t - \rho_r - t \cdot \rho_w$ could be more appropriate, e.g. consider a polynomial law to better take into account multiple scattering; this is under study for future version and for present implementation we consider modelling in term of α .

The transmission can be approximated as:

$$t = e^{-(0.5\tau_r + (1 - \omega_a f_a)\tau_a + \tau_{oz} + \tau_{wv})M} \quad (15)$$

Where τ_r is the Rayleigh optical thickness, τ_a the aerosol optical thickness and $\omega_a f_a$ the product of aerosol single scattering albedo with forward scattering probability, τ_{oz} is the ozone optical thickness, τ_{wv} is the ozone optical thickness and M is the air mass fraction of the pathlength, i.e.:

$$M = \frac{1}{\cos \theta_s} + \frac{1}{\cos \theta_v}$$

In Case 2 waters, $\rho_w(\lambda_{NIR})$ is no longer zero and the observed $\varepsilon(\lambda_{NIR}(1), \lambda_{NIR}(2))$ becomes:

$$\varepsilon[\lambda_{NIR}(1), \lambda_{NIR}(2)] = \{\rho_{as}[\lambda_{NIR}(1)] + t \cdot \rho_w[\lambda_{NIR}(1)]\} / \{\rho_{as}[\lambda_{NIR}(2)] + t \cdot \rho_w[\lambda_{NIR}(2)]\} \quad (16)$$

This epsilon can be expressed as:

$$\varepsilon[\lambda_{NIR}(1), \lambda_{NIR}(2)] = \varepsilon_{as}[\lambda_{NIR}(1), \lambda_{NIR}(2)] + t \cdot \{\rho_w[\lambda_{NIR}(1)] - \varepsilon[\lambda_{NIR}(1), \lambda_{NIR}(2)] \cdot \rho_w[\lambda_{NIR}(1)]\} / \rho_{as}[\lambda_{NIR}(2)] \quad (17)$$

Equation (3) shows that the ratio $\rho_w(\lambda_{NIR}(1))/\rho_w(\lambda_{NIR}(2))$ will always be greater than unity, given $a_w(\lambda_{NIR}(1)) > a_w(\lambda_{NIR}(2))$. If the MERIS NIR bands are used then the value of $\rho_w(\lambda_{NIR}(1))/\rho_w(\lambda_{NIR}(2))$ will be approximately 2, and $\varepsilon[\lambda_{NIR}(1), \lambda_{NIR}(2)]$ will be close to 1. Equation (17) may thus be approximated as:

$$\varepsilon[\lambda_{NIR}(1), \lambda_{NIR}(2)] = \varepsilon_{as}[\lambda_{NIR}(1), \lambda_{NIR}(2)] + 0.5t \cdot \{\rho_w[\lambda_{NIR}(1)]\} / \rho_{as}[\lambda_{NIR}(2)] \quad (18)$$

If the NIR reflectance is not taken into account, equation (18) shows that any NIR water leaving reflectance will result in the observed $\varepsilon(\lambda_{NIR}(1), \lambda_{NIR}(2))$ being greater than the true $\varepsilon_{as}[\lambda_{NIR}(1), \lambda_{NIR}(2)]$. This will result in overestimation of the Angstrom exponent or c parameter in bright pixel waters. The overestimation will then result in an overestimation of the extrapolated $\rho_{as}(\lambda)$ and therefore underestimate or create negative values for the resultant $\rho_w(\lambda)$ with the error being greater at shorter wavelengths. In areas of moderately high particles, where the atmospheric correction does not actually fail (negative $\rho_w(\lambda)$ values), the blue / green ratio will be increased and result in anomalously high retrievals of biogeochemical parameters. In multiple scattering algorithms (e.g. Gordon & Wang, 1994 or Antoine & Morel, 1998) the erroneous estimation of $\varepsilon(\lambda_{NIR}(1), \lambda_{NIR}(2))$ will result in the choice of the incorrect atmosphere model, with similar but less predictable results.

In order to solve this problem in bright pixel waters, it's necessary to solve a coupled hydrological and atmospheric optical model in the NIR (700 - 900 nm) that provides estimates of $\rho_{as}(\lambda)$ that can be used in either a single scattering or multiple scattering model.

It should be noted that in the case of the MERIS atmospheric correction that the Top of Atmosphere (TOA) reflectances are 'pre-corrected' for gaseous absorption, and thus Equation (15) becomes:

$$t = e^{-(0.5\tau_r + (1 - \omega_{af_a})\tau_a)M} \quad (19)$$

3.2 Hydrological Model Parameters

Given the F' tables, the BPAC is parameterised entirely using particulate IOPs. The algorithm uses the IOPs of pure water (a_w and bb_w) and particulates (bb_p and a_p) with the final value of bb_p used to estimate TSM for Case 2 flagging and as a potential MERIS product. The model runs used the F' polynomial tables, with the parameters as described in this section. A simple atmosphere model is used at the moment with typical values of ρ_{as} taken from MERIS images, and a value of alpha as described. At present no account is taken of the effect of increased surface albedo on the atmospheric path radiance. In terms of the accuracy of the BPAC, the figure of merit is the correct retrieval of the $\rho_w(NIR)$. The TSM product is qualitative since it's a scaled $bb_p(NIR)$ product and the relationship between TSM and $bb_p(NIR)$ is known to be highly variable; actual sediment concentrations may vary by over +/-50%. Since, in the NIR, there is little difference between the optical properties of phytoplankton, detritus and TSM for Case 1 waters the TSM figures will represent a dry weight or organic material that is closely coupled to chlorophyll concentration.

3.2.1 Pure Water Absorption

Figure 3 shows the absorption of pure water from a number of sources. Although there is good agreement in the 680-700 nm range, there is considerable disagreement at wavelengths greater the 700 nm and especially at the MERIS 775 nm and 865 nm bands. For the BPAC, the final choice of values (Kou et al, 1993) was determined by observed similarity spectra in the NIR (Ruddick et al 2006) from Wetlabs technical reports. In the visible region, the values of Pope and Fry (1997) were chosen. In the region where the Pope and Fry and Kou *et al* values overlapped, the values were combined by giving a weighed window towards the visible for the Pope vales and toward the NIR for the Kou values. Both absorption and error estimates were combined and the full table is supplied in the current MERIS RMD. Both the Kou and Pope values are estimated at a temperature of 22 °C.

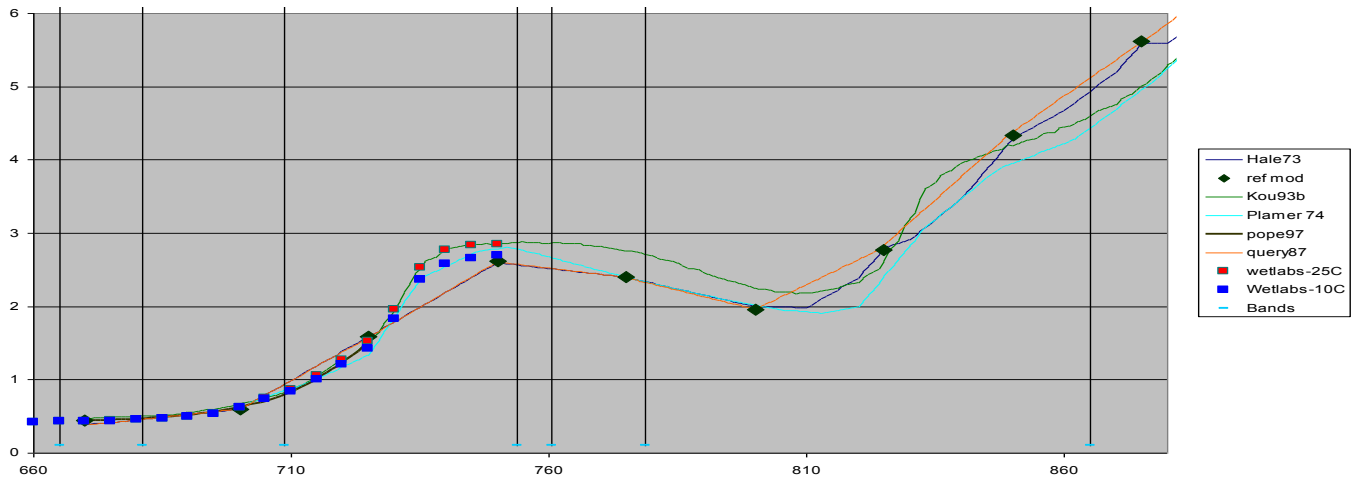


Figure 3: Variation in Water absorption from literature

It should also be noted that both the Kou and Pope absorption values are estimated at a temperature of 22 °C. Temperature effects are more difficult to determine, but Wetlabs provide good figures up to 750 nm and a set of Gaussian decompositions that can enable extrapolation. At wavelengths higher than this there are only brief technical reports. Figure 4 shows one illustration and there are similar data that are in qualitative agreement. In brief, all the NIR bands are to some extent influenced by temperature, but the greatest magnitude is at 753 nm that will make interpretation of data from this band difficult without temperature correction. Preliminary coefficients for the variation of absorption with temperature are provided in the MERIS RMD.

From measures taken by Wetlabs to correct the hyper-spectral AC instrument, salinity effects have been determined and found to be at least an order or magnitude less than temperature effects. They may be influenced by instrument artefacts since it's difficult to discriminate between changes in absorption due to salinity and those caused by changes in the refractive index of water.

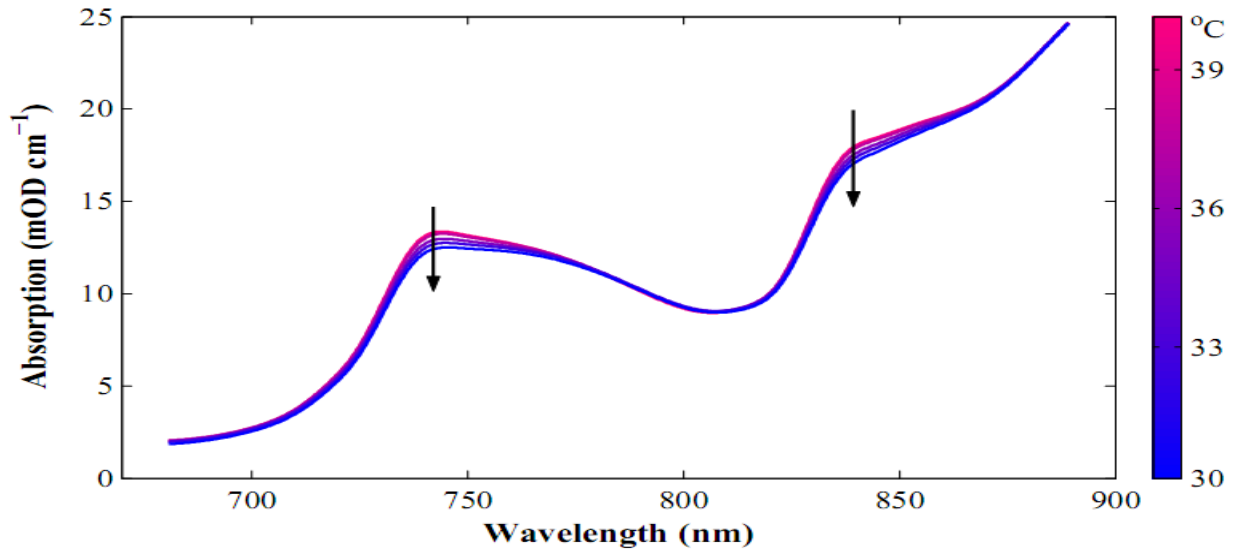


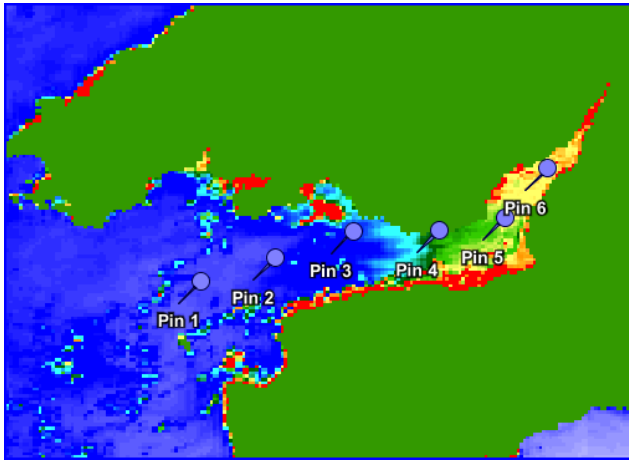
Figure 4: Temperature dependence of water absorption

3.2.2 Pure Water Scattering

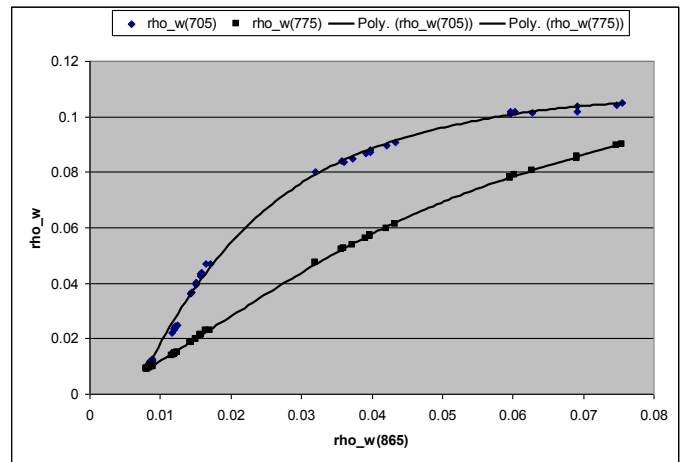
The values of pure water backscatter are chosen according to the MERIS RMD for seawater. There is a change in seawater backscatter according to salinity, and sensitivity to this will be examined in a later ATBD release. This is only expected to affect Case 1 waters and may require flagging in mesotrophic lakes; the current F' formulation permits this change of bb_w .

3.2.3 Particulate Absorption

NIR sediment properties at high concentrations are difficult to determine. In order to provide a preliminary set of coefficients to drive the BPAC, the equation for the limiting reflectance described in section 3.1.1 was used on a MERIS image of the Severn estuary. Figure 5 shows a set of points along the Severn estuary against scaled TOA 705 nm reflectance; the image was ICOL processed (code for adjacency correction, http://www.brockmann-consult.de/beam-wiki/download/attachments/13828113/ICOL_ATBD_1.1.pdf) in order to remove any adjacency effects. The data for the points were extracted from MEGS and were Rayleigh and gaseous absorption corrected. The atmosphere was assumed to be homogenous over the area and a simple AC was performed by extrapolating the points to zero reflectance and assuming that this intercept was the true ρ_{as} . The value for alpha was obtained from the Level 2 image for pin 1 and pin2. This ρ_{as} was subtracted from all the pin points and the saturation radiance obtained by fitting a Gompertz curve to Figure 5b. The absorption obtained is given in the MERIS RMD, and showed a weak exponential decline with wavelength.



a) Severn estuary pin set



b) reflection saturation at the Severn estuary pin set

Figure 5: Reflectance saturation - Severn Estuary

This exercise will be completed on further images and complemented by Mie modelling. Specifically this needs to be done for white scatters.

3.2.4 Particulate Scattering

The present values for particulate scattering are those specified in the MERIS RMD for Case 2 waters. As such, the BPAC is internally consistent with the neural network and protocol values. This is expected to evolve when white scatterers are accounted for as their spectral slope is known to approach 1 rather than the 0.4 as specified in the MERIS RMD.

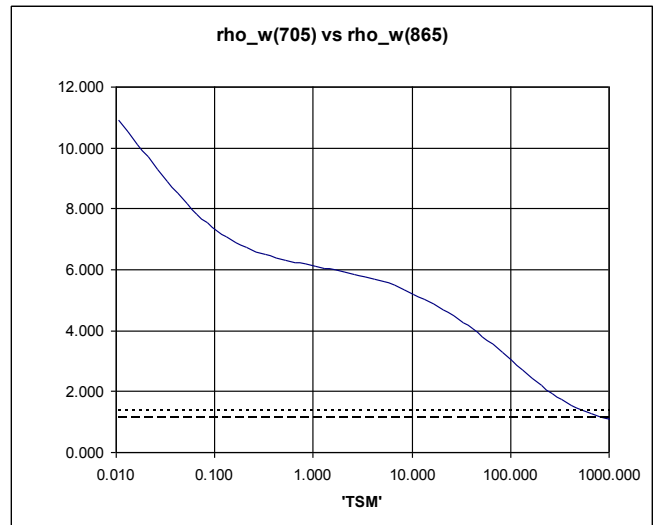
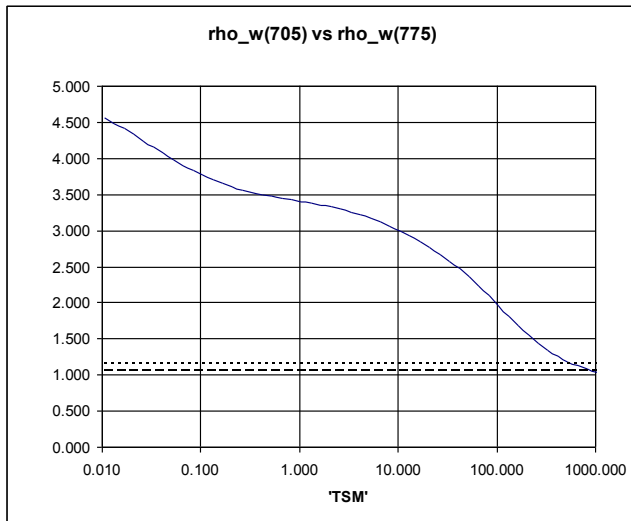
3.3 Model Sensitivity

3.3.1 Similarity and Optimal Band Choice

Figure 6 shows the expected similarity spectrum derived from the hydro-optical model, together with the expected ratios for an alpha of 0.5 and 1.5. For all the band pairs it can be seen that there are no problems discriminating between the slope of path radiance and the slope of water reflectance up to a nominal TSM value of around 500 g.m⁻³, although the actual in *in situ* gravimetric values may be as low as 100 g.m⁻³. The problem is using the 705 nm band for the variable sediment absorption.

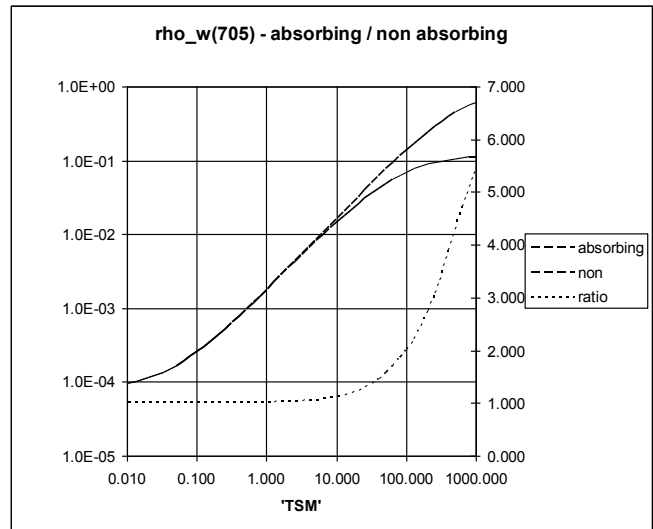
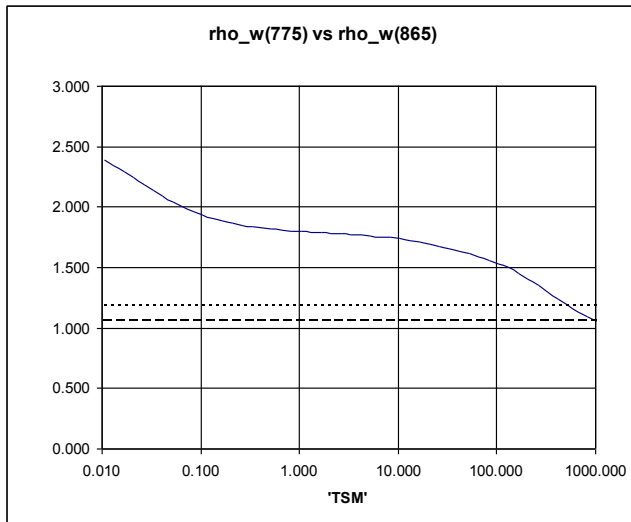
Figure 6d shows the hydro-optical model run for an absorbing and non-absorbing sediment. There is a clear change in the ratio between the absorbing and non-absorbing reflectance at concentrations greater than 10 g.m⁻³, and although the studies on the Severn estuary (see section 3.2.3) can to some extent account for this, a method needs to be developed to estimate sediment absorption from images; perhaps using the 412nm band. The solution for the problems with the 705 nm band set is to use higher band set for TSM >10 g.m⁻³. For these higher concentrations the 775, 865,885 nm band set can be used. Figure 7 shows the similarity for the 885 nm band. The 865:885 band pair shows no overlap between aerosol properties for nominal concentrations >1000 g.m⁻³,

and thus is the optimal band pair for estimating α . In contrast, the 775:885 band pair is optimal and can be used to estimate ρ_{as} given an α estimate.



a) Similarity spectrum for 705 vs. 775

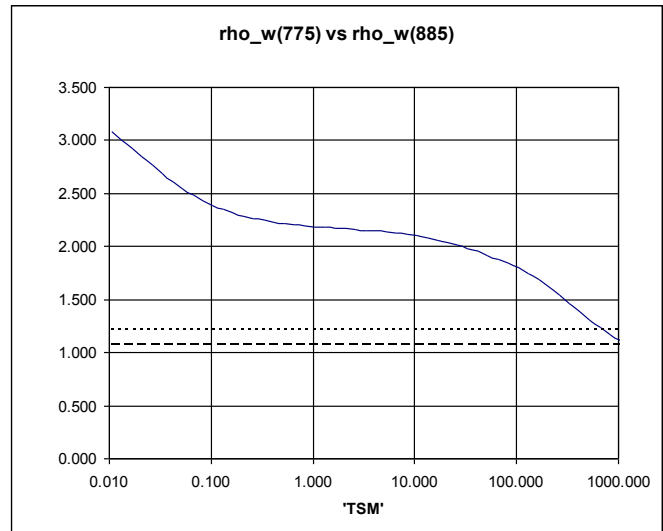
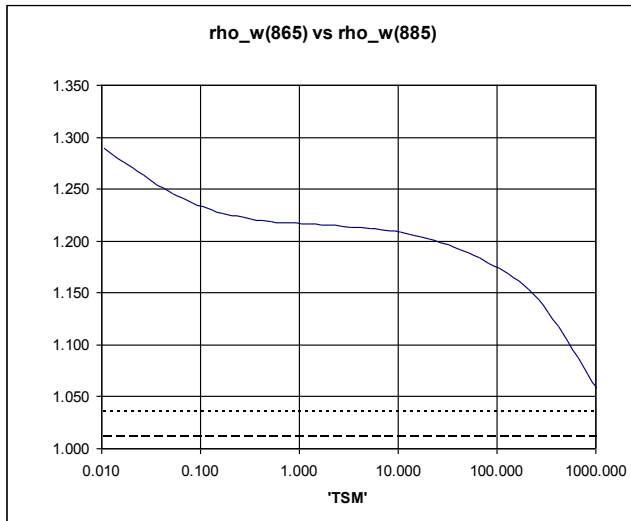
b) Similarity spectrum for 705 vs. 865



c) Similarity spectrum for 775 vs. 865

d) Modelled absorbing / non absorbing sediments

Figure 6: Similarity spectrum for low band set



a) Similarity spectrum for 865 vs 885

b) Similarity spectrum for 776 vs 885.

Figure 7: Similarity spectrum for high band set

3.3.2 Temperature and Smile

Figure 8 shows the effect of the change in the absorption coefficient of pure water on the low band set BPAC retrieval (see section 3.3.1 for information on the band set). The input a_w is adjusted for the temperature and the BPAC is run at the nominal values. The nominal alpha for the simulated data is 1.3, and it can be seen that there is a strong error in the retrieved alpha with an underestimate at TSM concentrations of $>2\text{g}\cdot\text{m}^{-3}$. The error in the alpha nominal at TSM $>12\text{g}\cdot\text{m}^{-3}$ is due to the errors implicit in using the lower band set. The result of this underestimate is to produce negative estimates of ρ_w at visible wavelengths.

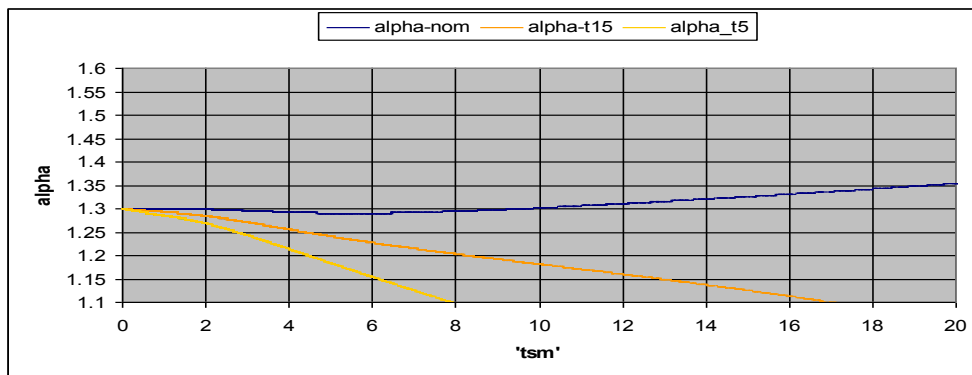


Figure 8: Sensitivity to Temperature - low band set

Figure 9 shows the effect of smile on the low band BPAC; as for Figure 8, but with the input a_w shifted by 1 nm. The smile change results in a dramatic error in the retrieved alpha at TSM concentrations of $>2 \text{ g.m}^{-3}$. This error would result in the MERIS AC being unable to determine a suitable candidate aerosol, and atmospheric correction failure.

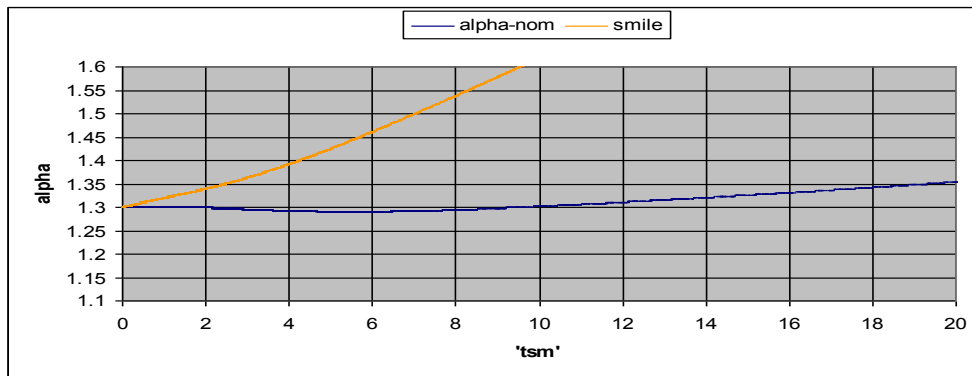
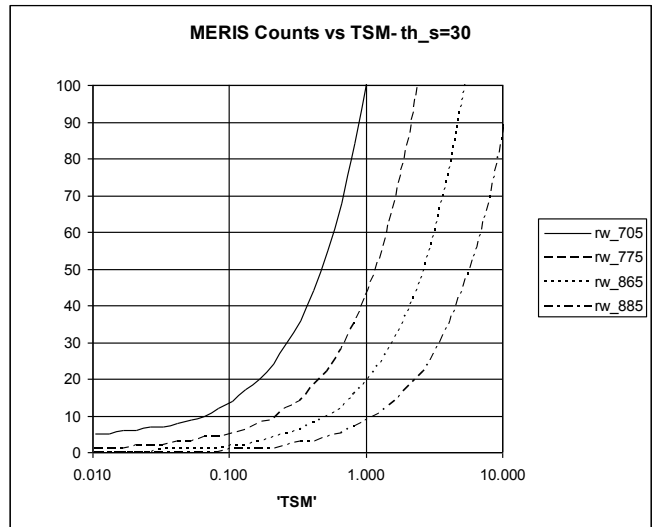
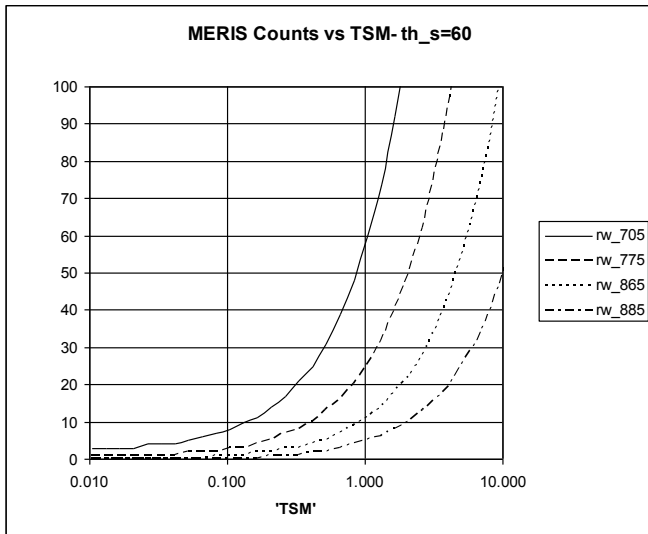


Figure 9: Sensitivity to 1 nm smile low band set

3.3.3 MERIS radiometric sensitivity and Aerosol retrieval error

During the evolutions of the BPAC there has been some debate about the appropriate threshold at which to run the BPAC correction. This threshold is not related to the water type, i.e. Case 1 / Case 2, rather it's related to the absolute backscatter in the NIR and its detectability by MERIS. Figure 10 shows the number of MERIS counts for the BPAC bands associated with nominal TSM, at solar zenith angles of 30 and 60 degrees. It can be seen that the effects of particulate scattering are detectable below 0.01 mg.m^{-3} in the 705 nm band. However, in order to successfully run the BPAC around $0.3 - 0.5 \text{ mg.m}^{-3}$ of TSM are required for the low band set, and $0.7 - 1.0 \text{ mg.m}^{-3}$ of TSM are required for the high band set. These thresholds are geometry dependant. The suggested threshold for 705 nm is 10 counts, but needs to be validated in terms of any image artefacts.

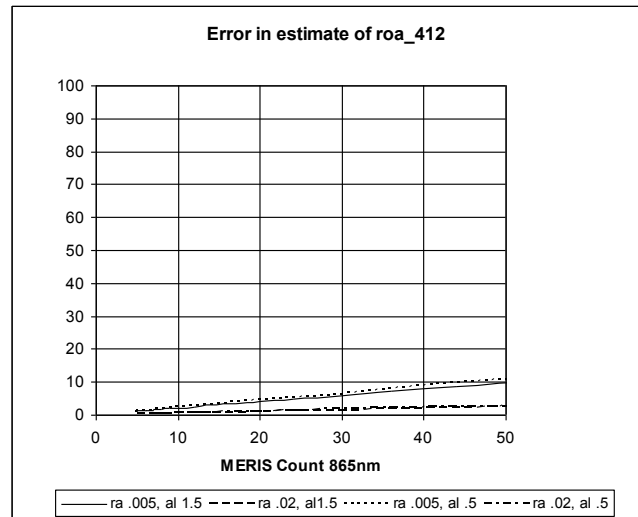
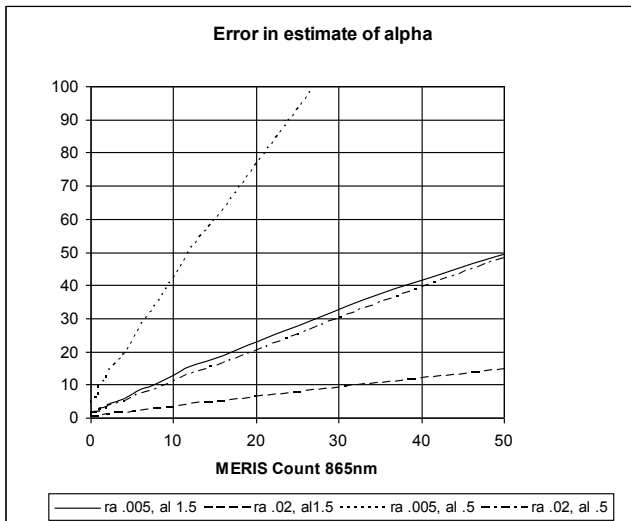


a) MERIS Counts vs. TSM at sun zenith of 60 degrees

b) MERIS Counts vs. TSM at sun zenith of 30 degrees

Figure 10: MERIS Counts vs. sediment load

Figure 11a shows the error in the estimation of alpha (α) by the BPAC for two values of α (0.5, 1.5) and two values of $\rho_{as}(705)$ (0.005, 0.02) in terms of MERIS counts at 865nm. In terms of errors, there is an interaction between ρ_{as} and α ; however, the highest error is for a low α and a low turbidity atmosphere. In terms of a single scattering, with CZCS type AC, these errors do not propagate to high errors in the estimated $\rho_{as}(412)$, Figure 11b. However, the effects on the MERIS AC are less predictable since the NIR α is used to choose the aerosol model. These preliminary results indicate a sensitivity of the BPAC to aerosols needs to be investigated using the full MERIS AC.



a) α error vs. MERIS counts

b) $\rho_{as}(412)$ error vs. MERIS Counts

Figure 11: Aerosol retrieval errors vs. MERIS Counts

3.4 Pre-processing

Compared to the original implementation of the BPAC (e.g. Lavender *et al.* 2005) where TSM was used as a state variable, the model is implemented in terms of the IOPs and the parameterisation as described in the previous sections.

3.4.1 Rayleigh correction and smile effect

In the MERIS processor, the top of atmosphere reflectance is first pre corrected for gaseous absorption and then for glint (i.e. where either no glint or the medium glint flags is asserted). There is then a combined processing to correct the Rayleigh component for the smile effect and pressure adjustment (Zagolski and Santer, 2016); note however that the residual aerosol and marine components are not corrected for smile effect at this stage. BPAC starts from this signal, $\rho_{gc}(\lambda)$, and correct it for Rayleigh scattering (at current pressure and theoretical wavelength λ):

$$\rho_{RC}(\lambda) = \rho_{gc}(\lambda) - \rho_R(\lambda)$$

This means that the aerosol and marine contribution should be evaluated, in a strict logic, at the detector wavelength λ_{pix} :

$$\rho_{RC}(\lambda) = \rho_{as}(\lambda_{pix}) + t \cdot \rho_w(\lambda_{pix})$$

In the following we will only use λ_{pix} in the aerosol term, which is analytic with respect to the wavelength. For the marine term, the uncertainty due to using the theoretical wavelength λ is negligible compared to the uncertainty of the marine model itself, hence we will use $t(\lambda)\rho_w(\lambda)$.

The Rayleigh optical thickness, τ_R , used in the diffuse transmittance, is also corrected for the actual pressure.

A further test checks that $\rho_{RC}(\lambda)$ is larger than signal of pure seawater, propagated at top of atmosphere. BPAC is launched only if this is true, as otherwise no aerosol content and particulate backscattering could be found.

3.4.2 Optional temperature and Smile Offsets

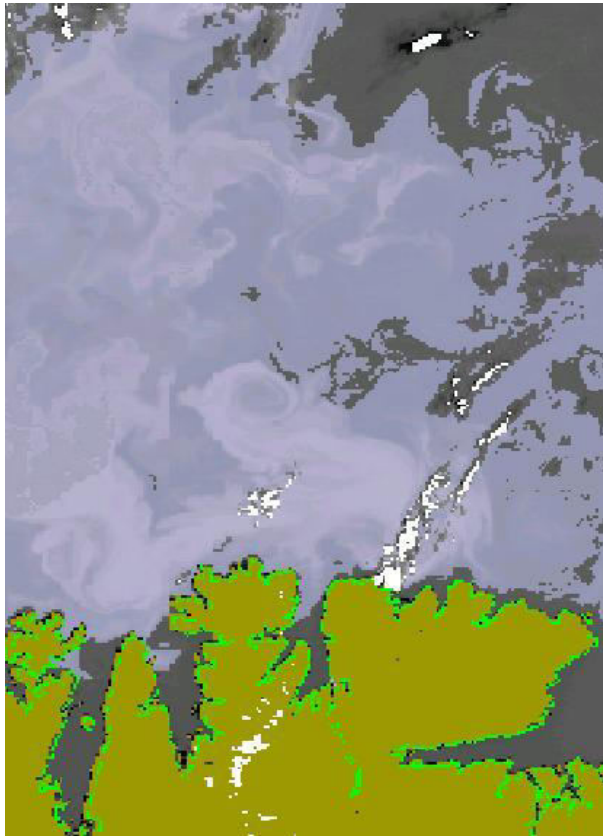
$$a_w'(\lambda_{pix}) = a_w(\lambda) + K\lambda a^*(\lambda - \lambda_{pix}) + KTa^*(22.0 - T)$$

Where λ is the theoretical wavelength of the standard water absorption, λ_{pix} is the actual MERIS wavelength and $K\lambda a$ is the rate of change of water absorption with wavelength; T is the observed temperature, 22.0 is the standard laboratory temperature for which the tables are provided and KTa is the rate of change of absorption with temperature. At present it is assumed that there is no interaction between $K\lambda a$ and KTa . It is also assumed that bb_w, bb_p, a_p have low sensitivities relative to wavelength.

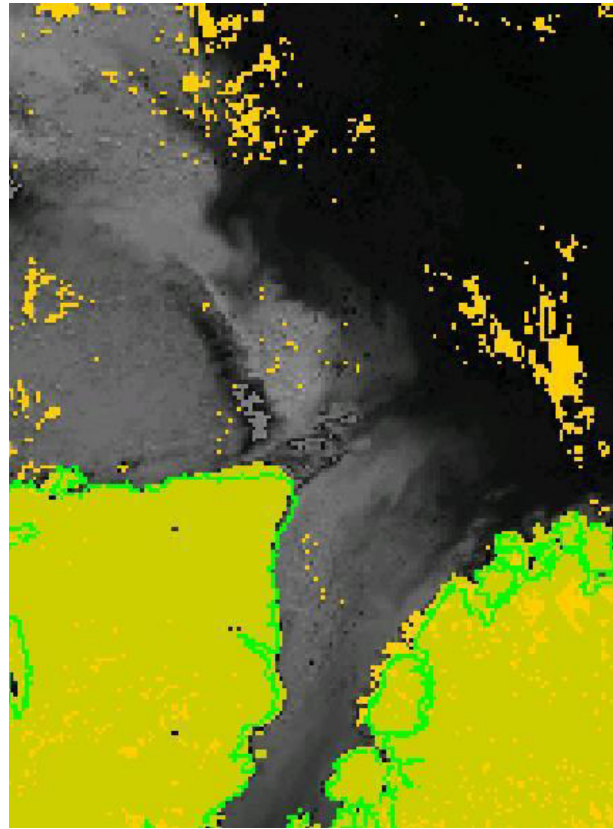
Such option is currently not implemented by lack of climatology.

3.4.3 Choice of IOPs

Although white scatterers such a coccolithophores rarely have saturation reflectance at they have significantly different scattering properties, since they do not have the levels of associated CDOM.



a) Barents sea coccolithophores bloom



b) Amazon Plume

Figure 12: White scatter Flag

The white scatterers are detected by a simple TOA log ratio flag and threshold:

The flag is:

$$\ln\left\{\frac{t_d(709)/t_d(620)}{[\rho_{rc}(620).a_w(620)] / [\rho_{rc}(709).a_w(709)]}\right\} / \ln\{620/709\}$$

The current flag threshold is 4.8. Figure 12 shows a comparison of the flag output for highly reflective coccolithophore bloom in the Barents Sea (a) compared with a highly reflective scene over the Amazon plume (b). The assertion of the flag is shown as purple in the Barents. It can be seen that the flag is not asserted in the coastal waters of the Barents sea and never asserted in the Amazon plume. Figure 13 shows the comparative 709/781 similarity slope for two scattering areas, the Barents Sea and the Severn estuary. Although the data range is different, the coccolithophores maintain a linear slope up to a $\rho_{rc}(709)$ of 0.02. This reflectance range will also encompass whitecaps and bubbles.

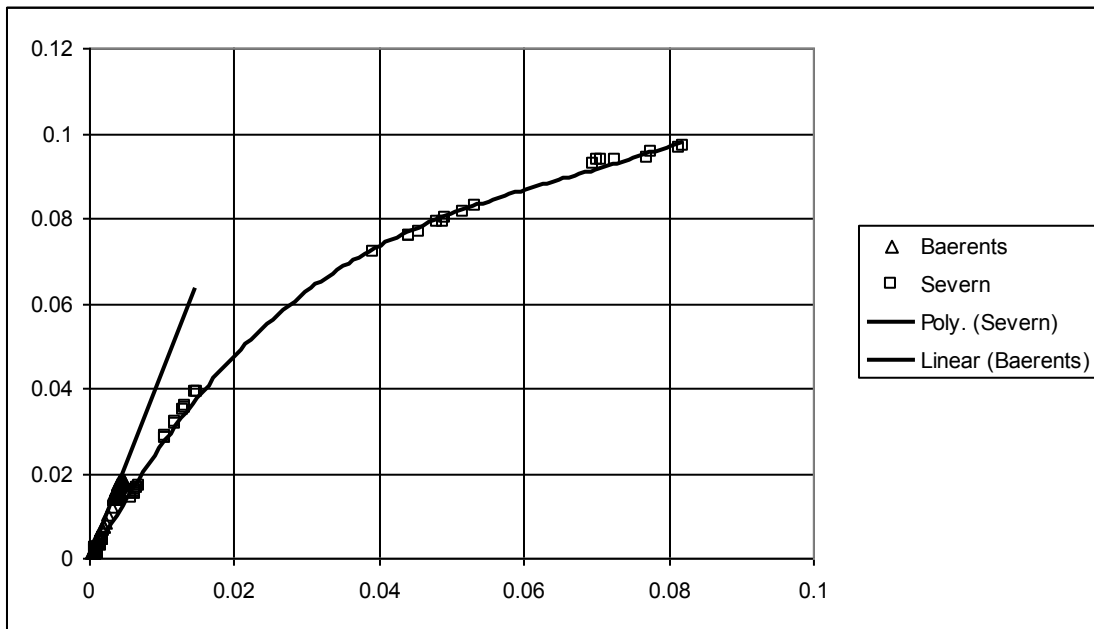


Figure 13: Comparative scattering in Severn Estuary and Barents Sea

3.5 Inversion

3.5.1 Strategy for numerical inversion

Previous implementation of the BPAC within MERIS 3rd reprocessing (Moore and Lavender 2011) has shown to fail over coastal waters when combined with the NIR vicarious calibration (Lerebourg et al 2011). A reminder of this failure is given on Figure 14 and Figure 15 below at AAOT, where we see that NIR calibration removes many valid points (up to 60 at 412 nm) and introduces new bias. Although the exact reason for such failure has not been totally understood (including the possible wrong assumption of vicarious calibration in terms of spectral band alignment), the problem demonstrates a too strong sensitivity of the BPAC to the radiometry.

In order to minimise the effect of NIR band calibration (or any miscalibration), present implementation is based on a spectral optimisation inversion. The idea is to minimise the discrepancy (χ^2 metrics) between the TOA signal and the model, with respect to some free parameters. It is worth noting that the atmospheric and bio-optical models are strictly similar to previous algorithm. Only the numerical inversion has evolved. With such approach, difficulties are to:

- Choose the free parameters
- Choose the bandset; we will here consider $\lambda_1 = 70$, $\lambda_2 = 753$, $\lambda_3 = 779$, $\lambda_4 = 865$ and $\lambda_5 = 890$
- Find a first guess close enough to the solution for ensuring convergence of the iterative minimisation
- Find realistic uncertainties weighting the χ^2 norm

In the following, the analysis is limited to 100 g/m³ TSM concentration, in line with MERIS RMD (approximately 50 g/m³ maximum in Case 2 water parameterisation).

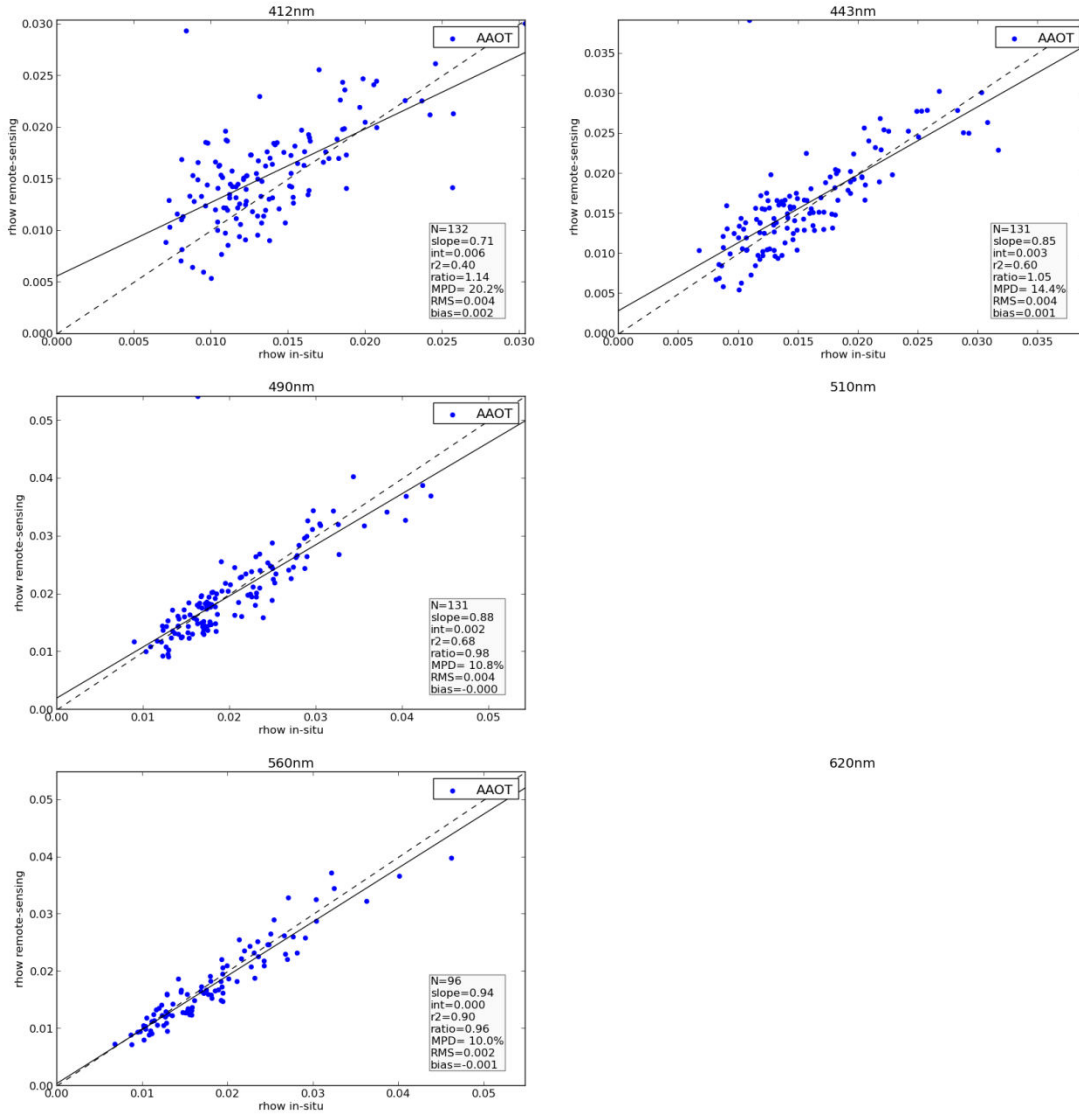


Figure 14 Validation of marine reflectance at AAOT with MERIS 3rd reprocessing when vicarious calibration is deactivated

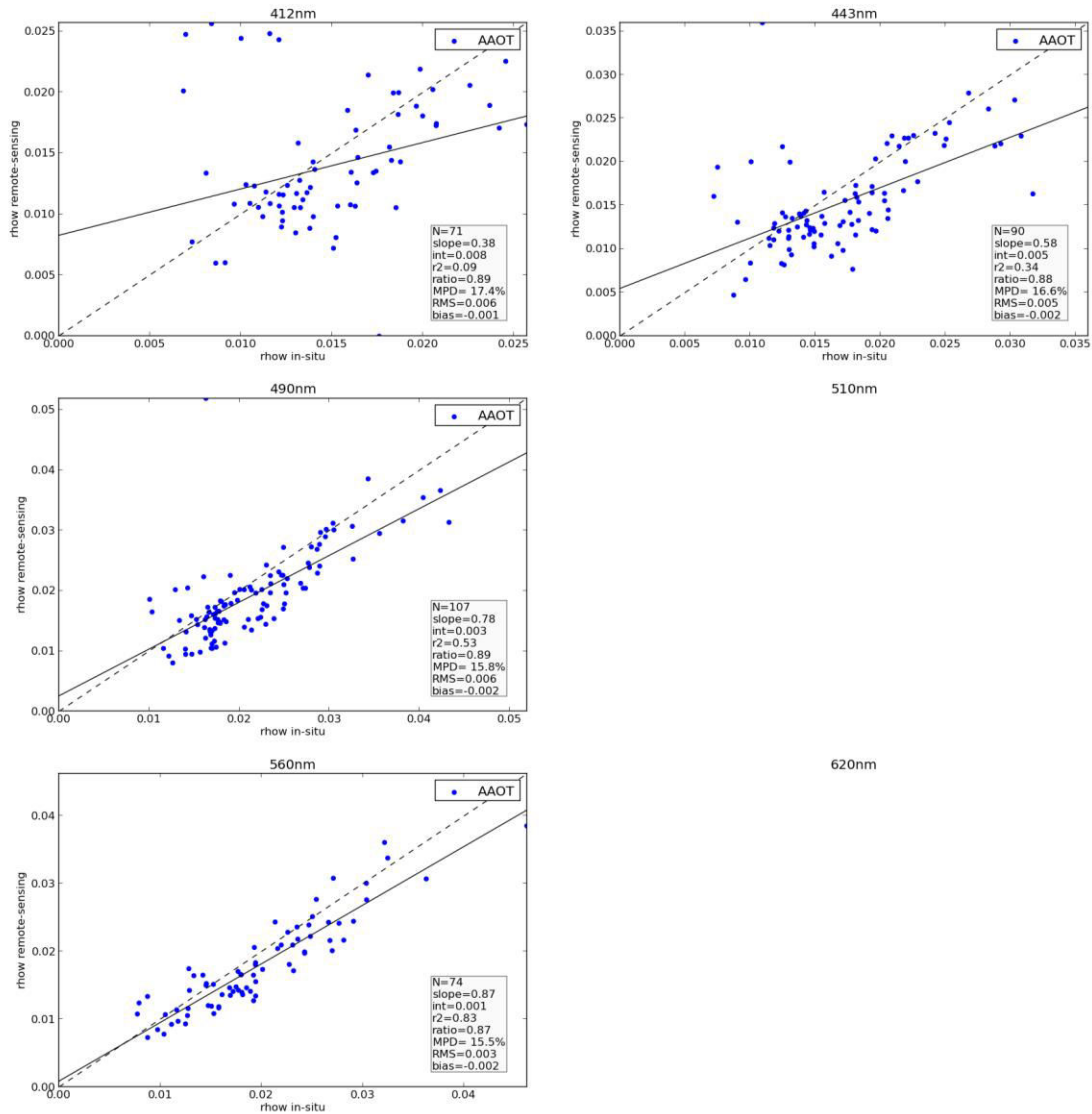


Figure 15 Validation of marine reflectance at AAOT with MERIS 3rd reprocessing when activating the NIR vicarious calibration

The complete BPAC model can be summarized by following equations, where for the sake of brevity we omit angular and wind speed dependence in the F' coefficients

$$\left. \begin{aligned}
 & b_{bp}(\lambda) = b_{bp}(\lambda_0) \left(\frac{\lambda}{\lambda_0} \right)^{-S_b} \\
 & a_p(\lambda) = a_p(\lambda_0) e^{-S_a(\lambda - \lambda_0)} \\
 & \omega(\lambda) = \frac{b_{bw}(\lambda) + b_{bp}(\lambda)}{a_w(\lambda) + a_p(\lambda) + b_{bw}(\lambda) + b_{bp}(\lambda)} \\
 & \eta(\lambda) = \frac{b_{bw}(\lambda)}{b_{bw}(\lambda) + b_{bp}(\lambda)} \\
 & F'(\lambda, \eta, \omega) = A_0(\lambda) + A_1(\lambda)\eta + a_0(\lambda) + a_1(\lambda)\omega + a_2(\lambda)\omega^2 + a_3(\lambda)\omega^3 + a_4(\lambda)\omega^4 \\
 & \rho_w(\lambda) = F'(\lambda, \eta, \omega) * \omega(\lambda) \\
 & t(\lambda) = e^{-\left(0.5\tau_R(\lambda) + (1-f\omega_a)\tau_a(\lambda_0)\left(\frac{\lambda}{\lambda_0}\right)^\alpha\right)M} \\
 & \rho_{as}(\lambda_{pix}) = \rho_{as}(\lambda_0) \left(\frac{\lambda_{pix}}{\lambda_0} \right)^\alpha \\
 & \rho_{RC}(\lambda) = t(\lambda)\rho_w(\lambda) + \rho_{as}(\lambda_{pix})
 \end{aligned} \right\}$$

We remind here that the aerosol reflectance must be computed at the detector wavelength λ_{pix} because it is not corrected for smile effect.

Particulate absorption at λ_0 (a reference band for spectral shape) is actually linked to backscattering coefficient by a linear relationship:

$$a_p(\lambda_0) = K * b_{bp}(\lambda_0)$$

If we deal with the more classical specific absorption and specific backscattering coefficient, this linear relationship writes

$$a_p(\lambda_0) = \frac{a_p^*(\lambda_0)}{b_{bp}^*(\lambda_0)} b_{bp}(\lambda_0)$$

So that the model parameter can be considered as $\frac{a_p^*(\lambda_0)}{b_{bp}^*(\lambda_0)}$ or more simply $a_p^*(\lambda_0)$ since $b_{bp}^*(\lambda_0)$ is not used in the algorithm and is somewhat arbitrary (it is only used at the very end to convert backscattering in term of TSM concentration).

Hence in all generality the BPAC model contains seven unknowns:

$$(\rho_{as}(\lambda_0), \alpha, (1 - f\omega_a)\tau_a(\lambda_0), b_{bp}(\lambda_0), S_b, a_p^*(\lambda_0), S_a)$$

For the atmospheric part, it is clear that aerosol reflectance $\rho_a(\lambda_0)$ and Angstrom exponent α are two major free parameters of the inversion. Sensitivity of the TOA signal to the aerosol optical thickness $\tau_a(\lambda_0)$, or equivalently to the product $(1 - f\omega_a)\tau_a(\lambda_0)$ in diffuse transmittance, is found relatively weak, of few percents, on the full red-NIR domain (see Figure 16). Hence $t_a(\lambda)$ can be computed once for all with fixed averaged values of $(1 - f\omega_a)\tau_a(\lambda_0)$ and Angstrom exponent.

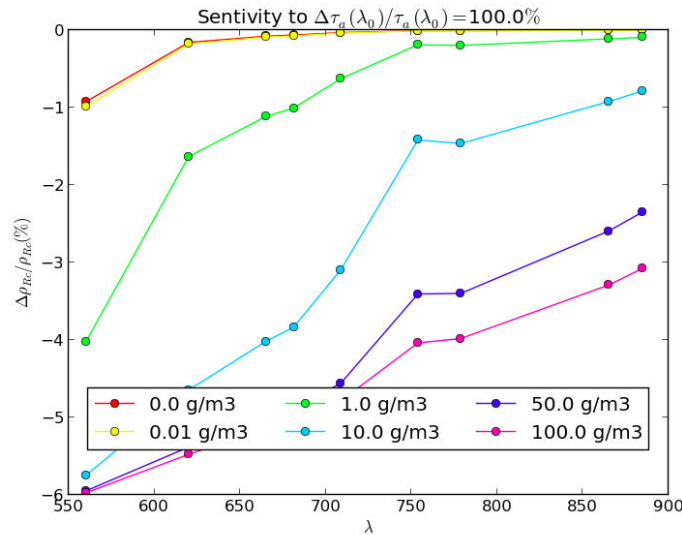


Figure 16 Sensitivity of the TOA signal $\rho_{RC}(\lambda)$ to a relative change $\frac{\Delta\tau_a(\lambda_0)}{\tau_a(\lambda_0)}$ of +100% around $\tau_a(\lambda_0)=0.1$ and $f\omega_a=0.8$, for several sediment concentrations (colours). Air mass is 2.4

The pseudo code for BPAC total transmittance is thus:

For ($\lambda=\lambda_1$; $\lambda \leq \lambda_5$; $\lambda++$) **do**

$$t(\lambda) = e^{-\left(0.5\tau_R(\lambda) + (1-f\omega_a)\overline{\tau_a(\lambda_0)}\left(\frac{\lambda}{\lambda_0}\right)^{\bar{\alpha}}\right)M}$$

Endfor

With $\overline{f\omega_a}=0.8$ and $\overline{\tau_a(865)}=0.1$ and $\bar{\alpha}=-1$.

For the marine model, a sensitivity study allows to determine which variables among $(b_{bp}(\lambda_0), S_b, a_p^*(\lambda_0), S_a)$ are the most important to retrieve. Given any variable x we are interested in the relative error

$$\frac{\Delta \rho_{RC}}{\rho_{RC}} = \frac{t \Delta \rho_w}{\rho_{RC}} \approx \frac{t}{\rho_{RC}} \frac{\partial \rho_w}{\partial x} \Delta x$$

From computation of ρ_w through F' relationship one has

$$\frac{\partial \rho_w}{\partial x} = \left(\frac{\partial F'}{\partial \omega} \omega + F' \right) \frac{\partial \omega}{\partial x} + \frac{\partial F'}{\partial \eta} \omega \frac{\partial \eta}{\partial x}$$

Where derivatives of F' are simply given by

$$\begin{cases} \frac{\partial F'}{\partial \omega}(\lambda, \eta, \omega) = a_1(\lambda) + 2a_2(\lambda)\omega + 3a_3(\lambda)\omega^2 + 4a_4(\lambda)\omega^3 \\ \frac{\partial F'}{\partial \eta}(\lambda, \eta, \omega) = C(\lambda) \end{cases}$$

Derivatives of ω and η can also be computed analytically –note that some of these computations will be useful for the χ^2 minimisation:

$$\left\{ \begin{array}{l} \frac{\partial \omega(\lambda)}{\partial b_{bp}(\lambda_0)} = \frac{\left(\frac{\lambda}{\lambda_0}\right)^{-S_b} * a_w(\lambda) - \frac{a_p^*(\lambda_0)}{b_{bp}^*(\lambda_0)} e^{-S_a(\lambda-\lambda_0)} * b_{bw}(\lambda)}{\left(a_w(\lambda) + a_p(\lambda) + b_{bw}(\lambda) + b_{bp}(\lambda)\right)^2} \\ \frac{\partial \omega(\lambda)}{\partial S_b} = -\ln \frac{\lambda}{\lambda_0} * b_{bp}(\lambda) \frac{a_w(\lambda) + a_p(\lambda)}{\left(a_w(\lambda) + a_p(\lambda) + b_{bw}(\lambda) + b_{bp}(\lambda)\right)^2} \\ \frac{\partial \omega(\lambda)}{\partial a_p^*(\lambda_0)} = -\frac{a_p(\lambda)}{a_p^*(\lambda_0)} \frac{b_{bw}(\lambda) + b_{bp}(\lambda)}{\left(a_w(\lambda) + a_p(\lambda) + b_{bw}(\lambda) + b_{bp}(\lambda)\right)^2} \\ \frac{\partial \omega(\lambda)}{\partial S_a} = a_p(\lambda) * (\lambda - \lambda_0) \frac{b_{bw}(\lambda) + b_{bp}(\lambda)}{\left(a_w(\lambda) + a_p(\lambda) + b_{bw}(\lambda) + b_{bp}(\lambda)\right)^2} \\ \frac{\partial \eta(\lambda)}{\partial b_{bp}(\lambda_0)} = -\left(\frac{\lambda}{\lambda_0}\right)^{-S_b} \frac{b_{bw}(\lambda)}{\left(b_{bw}(\lambda) + b_{bp}(\lambda)\right)^2} \\ \frac{\partial \eta(\lambda)}{\partial S_b} = \ln \frac{\lambda}{\lambda_0} * b_{bp}(\lambda) \frac{b_{bw}(\lambda)}{\left(b_{bw}(\lambda) + b_{bp}(\lambda)\right)^2} \end{array} \right.$$

Graph of figure Figure 17 shows $\frac{\Delta\rho_{RC}}{\rho_{RC}}$ for variation in each marine parameter of 100%. Such input uncertainty is realistic when considering variation in the literature (e.g. Babin et al. 2003). Obviously the most important variable is $b_{bp}(\lambda_0)$, i.e. sediment concentration. Sensitivity to other variables is strongly growing when going to the visible bands and with growing TSM, what incites us to avoid such spectral domain. When considering mainly the bands in the NIR, the order of importance of the parameters is $b_{bp}(\lambda_0)$ then $a_p^*(\lambda_0)$ then S_a and then S_b (this is true with current BPAC constants).

In view of limiting the number of free parameters, this analysis suggests to inverse only three parameters, namely $(\rho_a(\lambda_0), \alpha, b_{bp}(\lambda_0))$, as in previous BPAC, but using all available bands in the NIR: 753, 779, 865, 885. Uncertainty due to other fixed parameters can be taken into account in the χ^2 formalism, if necessary.

With fixed $(S_b, a_p^*(\lambda_0), S_a)$, we can introduce for convenience two tabulated spectral shape:

$$\left(\frac{\lambda}{\lambda_0}\right)^{-S_b} = \frac{b_{bp}^*(\lambda)}{b_{bp}^*(\lambda_0)}$$

$$a_p \cdot b_p(\lambda) = \frac{a_p(\lambda)}{b_{bp}(\lambda)} = a_p^*(\lambda_0) \frac{e^{-S_a(\lambda-\lambda_0)}}{b_{bp}^*(\lambda)}$$

In order to minimise error propagation on the spectral shape, we choose for λ_0 the central NIR band at 779 nm.

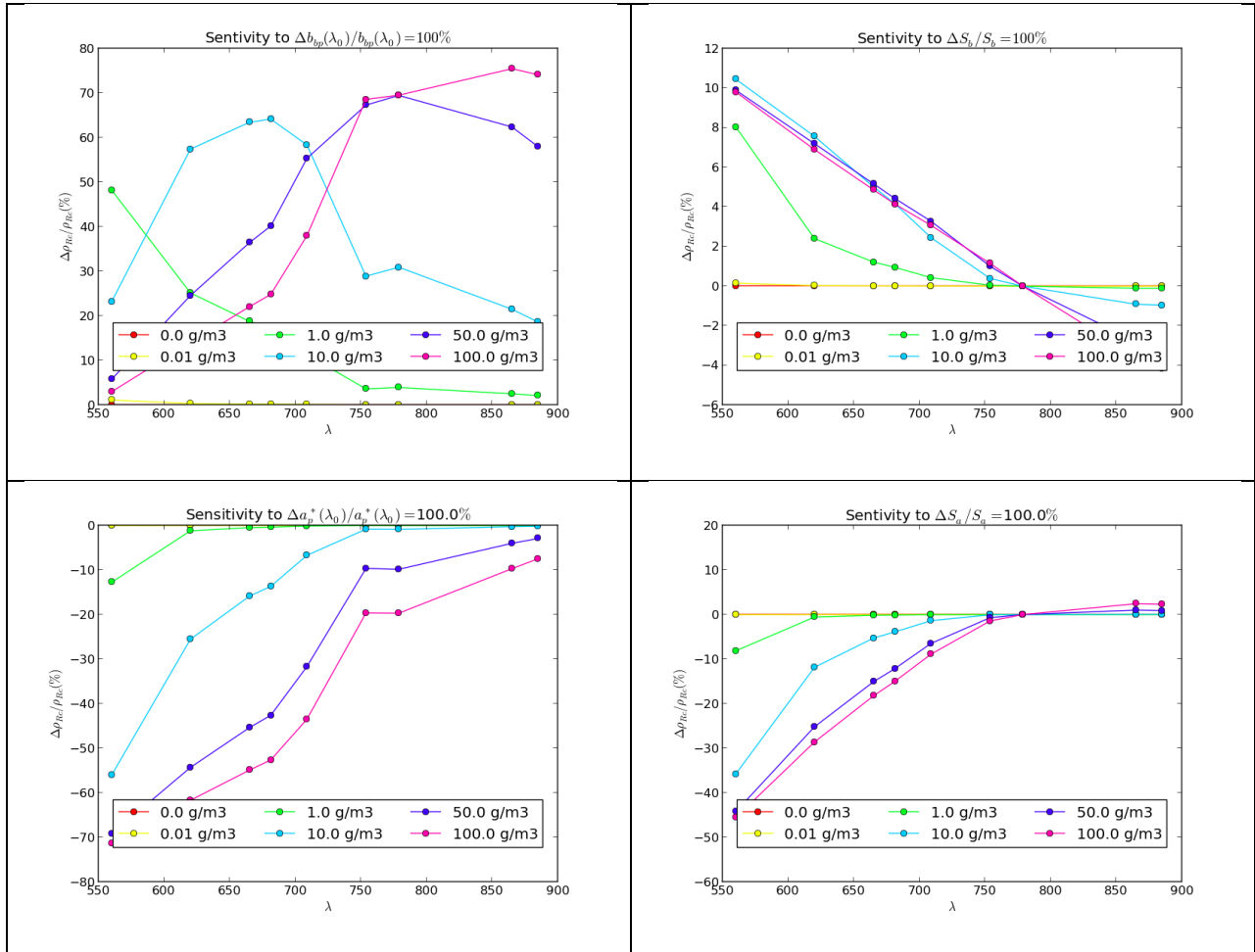


Figure 17 Sensitivity of the TOA signal $\rho_{RC}(\lambda)$ to a relative change of +100% respectively on $\frac{\Delta b_{bp}(\lambda_0)}{b_{bp}(\lambda_0)}$ (top left), on $\frac{\Delta S_b}{S_b}$ (top right), on $\frac{\Delta a_p^*(\lambda_0)}{a_p^*(\lambda_0)}$ (bottom left) and $\frac{\Delta S_a}{S_a}$ (bottom right) for several sediment concentrations from 0 to 100 g/m³ (colours). Air mass is 2.4

3.5.2 χ^2 minimisation

The χ^2 measuring discrepancy between observation and model is given by

$$\chi^2 = \sum_{\lambda} \left(\frac{r(\lambda)}{\sigma(\lambda)} \right)^2$$

Where the residual $r(\lambda)$ is

$$r(\lambda) = t(\lambda)\rho_w(\lambda) + \rho_{as}(\lambda_0) \left(\frac{\lambda_{pix}}{\lambda_0} \right)^\alpha - \rho_{RC}(\lambda)$$

And $\sigma(\lambda)$ is the associated uncertainty described in section 3.5.4.

Because turbidity and aerosol reflectance range over several orders of magnitude, their associated unknowns is expressed in base-10 logarithmic scale; this also prevents to converge towards unphysical negative values. Hence the three free parameters are:

$$\mathbf{x} = (x_1, x_2, x_3) = (\log \rho_{as}(\lambda_0), \alpha, \log b_{bp}(\lambda_0))$$

Minimisation is equivalent to find root of partial derivatives of χ^2 . Up to a factor 2, we find these derivatives to be:

$$\nabla \chi^2 = \begin{pmatrix} \frac{\partial \chi^2}{\partial x_1} \\ \frac{\partial \chi^2}{\partial x_2} \\ \frac{\partial \chi^2}{\partial x_3} \end{pmatrix} \propto \begin{pmatrix} \ln 10 \sum_{\lambda} \frac{1}{\sigma(\lambda)^2} r(\lambda) \rho_{as}(\lambda_{pix}) \\ \sum_{\lambda} \frac{1}{\sigma(\lambda)^2} r(\lambda) * \rho_{as}(\lambda_{pix}) \ln \left(\frac{\lambda_{pix}}{\lambda_0} \right) \\ \sum_{\lambda} \frac{1}{\sigma(\lambda)^2} r(\lambda) t(\lambda) \frac{\partial \rho_w(\lambda)}{\partial x_3} \end{pmatrix}$$

We propose to solve $\nabla \chi^2 = 0$ by the Newton-Raphson algorithm, which has in general a quadratic rate of convergence and is easily implementable; not that any other algorithm could be proposed (e.g. directly Levenberg-Marquardt to minimize the χ^2). Such approach needs to compute derivative of $\nabla \chi^2$, i.e. the Hessian matrix \mathcal{H} of χ^2 . By symmetry only six elements need to be computed:

$$\left\{ \begin{array}{l} \mathcal{H}_{11} = \frac{\partial^2 \chi^2}{\partial x_1^2} = (\ln 10)^2 \sum_{\lambda} \frac{1}{\sigma(\lambda)^2} (r(\lambda) + \rho_{as}(\lambda_{pix})) \rho_{as}(\lambda_{pix}) \\ \mathcal{H}_{12} = \frac{\partial^2 \chi^2}{\partial x_1 \partial x_2} = \ln 10 \sum_{\lambda} \frac{1}{\sigma(\lambda)^2} \ln \left(\frac{\lambda_{pix}}{\lambda_0} \right) \rho_{as}(\lambda_{pix}) (r(\lambda) + \rho_{as}(\lambda_{pix})) \\ \mathcal{H}_{13} = \frac{\partial^2 \chi^2}{\partial x_1 \partial x_3} = \ln 10 \sum_{\lambda} \frac{1}{\sigma(\lambda)^2} \rho_{as}(\lambda_{pix}) t(\lambda) \frac{\partial \rho_w(\lambda)}{\partial x_3} \\ \mathcal{H}_{22} = \frac{\partial^2 \chi^2}{\partial x_2^2} = \sum_{\lambda} \frac{1}{\sigma(\lambda)^2} \left(\ln \left(\frac{\lambda_{pix}}{\lambda_0} \right) \right)^2 \left(\frac{\lambda_{pix}}{\lambda_0} \right)^{\alpha} \rho_{as}(\lambda_0) (r(\lambda) + \rho_{as}(\lambda_{pix})) \\ \mathcal{H}_{23} = \frac{\partial^2 \chi^2}{\partial x_2 \partial x_3} = \sum_{\lambda} \frac{1}{\sigma(\lambda)^2} \ln \left(\frac{\lambda_{pix}}{\lambda_0} \right) \left(\frac{\lambda_{pix}}{\lambda_0} \right)^{\alpha} \rho_{as}(\lambda_0) t(\lambda) \frac{\partial \rho_w(\lambda)}{\partial x_3} \\ \mathcal{H}_{33} = \frac{\partial^2 \chi^2}{\partial x_3^2} = \sum_{\lambda} \frac{1}{\sigma(\lambda)^2} t(\lambda) \left(t(\lambda) \left(\frac{\partial \rho_w(\lambda)}{\partial x_3} \right)^2 + r(\lambda) \frac{\partial^2 \rho_w(\lambda)}{\partial x_3^2} \right) \end{array} \right.$$

Given an iterate at step (n), the Newton-Raphson algorithm defines next iterate by the solving this linear system:

$$\mathcal{H}^{(n)}(\mathbf{x}^{(n+1)} - \mathbf{x}^{(n)}) = -\nabla \chi^2^{(n)}$$

For the computation of Hessian matrix, we need second order derivative of marine signal:

$$\frac{\partial^2 \rho_w}{\partial x \partial y} = \left(\frac{\partial^2 F'}{\partial \omega^2} \omega + 2 \frac{\partial F'}{\partial \omega} \right) \frac{\partial \omega}{\partial x} \frac{\partial \omega}{\partial y} + \left(\frac{\partial F'}{\partial \omega} \omega + F' \right) \frac{\partial^2 \omega}{\partial x \partial y} + \frac{\partial F'}{\partial \eta} \left(\frac{\partial \omega}{\partial x} \frac{\partial \eta}{\partial y} + \frac{\partial \omega}{\partial y} \frac{\partial \eta}{\partial x} \right) + \frac{\partial F'}{\partial \eta} \frac{\partial^2 \eta}{\partial x \partial y} \omega$$

All five available wavelengths in the NIR are used to compute the χ^2 :

$$\lambda_1 = 709, \lambda_2 = 753, \lambda_3 = 779, \lambda_4 = 865, \lambda_5 = 890$$

The pseudo-code for χ^2 minimisation is as follows:

```

Save bbp for convergence check

bbp_old = b_bp(\lambda_0)

Start iterative loop

For (counter=0; counter<10; counter++) do

    Initialise the linear system
  
```

$\mathcal{H} = 0$. (null 3x3 matrix)

$\nabla \chi^2 = 0$ (null 3x1 vector)

Loop over band to construct the linear system

For ($\lambda = \lambda_1$; $\lambda \leq \lambda_5$; $\lambda++$) **do**

 Compute particulate backscattering

$$b_{bp}(\lambda) = b_{bp}(\lambda_0) \frac{b_{bp}^*(\lambda)}{b_{bp}^*(\lambda_0)}$$

 Compute particulate absorption

$$a_p(\lambda) = b_{bp}(\lambda) * a_{p_bp}(\lambda)$$

 Compute total attenuation

$$c(\lambda) = a_w(\lambda) + a_p(\lambda) + b_{bw}(\lambda) + b_{bp}(\lambda)$$

 Compute single scattering albedo and η

$$\omega(\lambda) = \frac{b_{bw}(\lambda) + b_{bp}(\lambda)}{c(\lambda)}$$

$$\eta(\lambda) = \frac{b_{bw}(\lambda)}{b_{bw}(\lambda) + b_{bp}(\lambda)}$$

 Compute F' factor

$$F'(\lambda) = A_0(\lambda) + C(\lambda)\eta + a_0(\lambda) + a_1(\lambda)\omega + a_2(\lambda)\omega^2 + a_3(\lambda)\omega^3 + a_4(\lambda)\omega^4$$

 Compute ρ_w

$$\rho_w(\lambda) = F'(\lambda) * \omega(\lambda)$$

 Compute derivative of F'

$$\frac{\partial F'}{\partial \omega}(\lambda) = a_1(\lambda) + 2a_2(\lambda)\omega + 3a_3(\lambda)\omega^2 + 4a_4(\lambda)\omega^3$$

$$\frac{\partial^2 F'}{\partial \omega^2}(\lambda) = 2a_2(\lambda) + 6a_3(\lambda)\omega + 12a_4(\lambda)\omega^2$$

$$\frac{\partial F'}{\partial \eta}(\lambda) = A_1(\lambda)$$

 Compute derivative of ω with respect to backscattering $x_3 = \log b_{bp}(\lambda_0)$

$$\frac{\partial \omega(\lambda)}{\partial x_3} = \frac{b_{bp}^*(\lambda)}{b_{bp}^*(\lambda_0)} \frac{a_w(\lambda) - a_p - b_p(\lambda) * b_{bw}(\lambda)}{c(\lambda)^2} b_{bp}(\lambda_0) \ln 10$$

$$\frac{\partial^2 \omega(\lambda)}{\partial x_3^2} = -2c(\lambda) \frac{a_p - b_p(\lambda) + 1}{a_w(\lambda) - a_p - b_p(\lambda) * b_{bw}(\lambda)} \left(\frac{\partial \omega(\lambda)}{\partial x_3} \right)^2 + \frac{\partial \omega(\lambda)}{\partial x_3} \ln 10$$

Compute derivative of η with respect to backscattering $x_3 = \log b_{bp}(\lambda_0)$

$$\frac{\partial \eta(\lambda)}{\partial x_3} = - \frac{b_{bw}(\lambda)}{(b_{bw}(\lambda) + b_{bp}(\lambda))^2} b_{bp}(\lambda_0) \ln 10$$

$$\frac{\partial^2 \eta(\lambda)}{\partial x_3^2} = 2 \frac{b_{bw}(\lambda) + b_{bp}(\lambda)}{b_{bw}(\lambda)} \left(\frac{\partial \eta(\lambda)}{\partial x_3} \right)^2 + \frac{\partial \eta(\lambda)}{\partial x_3} \ln 10$$

Compute derivative of ρ_w with respect to backscattering $x_3 = \log b_{bp}(\lambda_0)$

$$\frac{\partial \rho_w(\lambda)}{\partial x_3} = \left(\frac{\partial F'}{\partial \omega} \omega + F' \right) \frac{\partial \omega}{\partial x_3} + \frac{\partial F'}{\partial \eta} \frac{\partial \eta}{\partial x_3} \omega$$

$$\frac{\partial^2 \rho_w(\lambda)}{\partial x_3^2} = \left(\frac{\partial^2 F'}{\partial \omega^2} \omega + 2 \frac{\partial F'}{\partial \omega} \right) \left(\frac{\partial \omega}{\partial x_3} \right)^2 + \left(\frac{\partial F'}{\partial \omega} \omega + F' \right) \frac{\partial^2 \omega}{\partial x_3^2} + 2 \frac{\partial F'}{\partial \eta} \frac{\partial \omega}{\partial x_3} \frac{\partial \eta}{\partial x_3} + \frac{\partial F'}{\partial \eta} \frac{\partial^2 \eta}{\partial x_3^2} \omega$$

Compute aerosol residual

$$\rho_{as}(\lambda_{pix}) = \rho_{as}(\lambda_0) \left(\frac{\lambda_{pix}}{\lambda_0} \right)^\alpha$$

Compute χ^2 residual

$$r(\lambda) = t(\lambda) \rho_w(\lambda) + \rho_{as}(\lambda_0) \left(\frac{\lambda_{pix}}{\lambda_0} \right)^\alpha - \rho_{RC}(\lambda)$$

Compute $\nabla \chi^2$ sequentially

$$(\nabla \chi^2)_1 = (\nabla \chi^2)_1 + \frac{1}{\sigma(\lambda)^2} \ln 10 r(\lambda) \rho_{as}(\lambda_{pix})$$

$$(\nabla \chi^2)_2 = (\nabla \chi^2)_2 + \frac{1}{\sigma(\lambda)^2} r(\lambda) \rho_{as}(\lambda_{pix}) \ln \left(\frac{\lambda_{pix}}{\lambda_0} \right)$$

$$(\nabla \chi^2)_3 = (\nabla \chi^2)_3 + \frac{1}{\sigma(\lambda)^2} r(\lambda) t(\lambda) \frac{\partial \rho_w(\lambda)}{\partial x_3}$$

Compute \mathcal{H} sequentially

$$\mathcal{H}_{11} = \mathcal{H}_{11} + \frac{1}{\sigma(\lambda)^2} (\ln 10)^2 \left(r(\lambda) + \rho_{as}(\lambda_{pix}) \right) \rho_{as}(\lambda_{pix})$$

$$\mathcal{H}_{12} = \mathcal{H}_{12} + \frac{1}{\sigma(\lambda)^2} \ln 10 \ln \frac{\lambda_{pix}}{\lambda_0} \left(r(\lambda) + \rho_{as}(\lambda_{pix}) \right) \rho_{as}(\lambda_{pix})$$

$$\mathcal{H}_{13} = \mathcal{H}_{13} + \frac{1}{\sigma(\lambda)^2} \ln 10 \rho_{as}(\lambda_{pix}) t(\lambda) \frac{\partial \rho_w(\lambda)}{\partial x_3}$$

$$\mathcal{H}_{22} = \mathcal{H}_{22} + \frac{1}{\sigma(\lambda)^2} \left(\ln \frac{\lambda_{pix}}{\lambda_0} \right)^2 \left(r(\lambda) + \rho_{as}(\lambda_{pix}) \right) \rho_{as}(\lambda_{pix})$$

$$\mathcal{H}_{23} = \mathcal{H}_{23} + \frac{1}{\sigma(\lambda)^2} \ln \frac{\lambda}{\lambda_0} \rho_{as}(\lambda_{pix}) t(\lambda) \frac{\partial \rho_w(\lambda)}{\partial x_3}$$

$$\mathcal{H}_{33} = \mathcal{H}_{33} + \frac{1}{\sigma(\lambda)^2} t(\lambda) \left(t(\lambda) \left(\frac{\partial \rho_w(\lambda)}{\partial x_3} \right)^2 + r(\lambda) \frac{\partial^2 \rho_w(\lambda)}{\partial x_3^2} \right)$$

Endfor

Compute symmetric terms

$$\mathcal{H}_{21} = \mathcal{H}_{12}$$

$$\mathcal{H}_{31} = \mathcal{H}_{13}$$

$$\mathcal{H}_{32} = \mathcal{H}_{23}$$

Solve the linear system

$$status = Lin_solv(\mathcal{H}, \nabla \chi^2, X)$$

Update solution, dealing with exception

If (status=0 and $|X_1| < 3$ and $|X_3| < 3$) **then**

$$\rho_{as}(\lambda_0) = \rho_{as}(\lambda_0) * 10^{-X_1}$$

$$\alpha = \alpha - X_2$$

$$b_{bp}(\lambda_0) = b_{bp}(\lambda_0) * 10^{-X_3}$$

Else

$$\rho_{as}(\lambda_0) = \rho_{as}(\lambda_0)_{init}$$

$$\alpha = \alpha_{int}$$

$$b_{bp}(\lambda_0) = b_{bp}(\lambda_0)_{init}$$

Break

Endif

Check convergence

If $|b_{bp}(\lambda_0) - bbp_old|/b_{bp}(\lambda_0) < 10^{-3}$ **then**

Break

Endif

$bbp_old = b_{bp}(\lambda_0)$

Endfor *End of iterative loop*

3.5.3 Final marine reflectance output

After convergence (or failure) of the iterative process, the final marine reflectance of BPAC is deduced from ρ_{Rc} and ρ_{as} , the latter being computed at the theoretical wavelength λ (and not λ_{pix} as before), to correct it directly for smile effect:

$$t(\lambda)\rho_{wc2}(\lambda) = \rho_{Rc}(\lambda) - \rho_{as}(\lambda_0) \left(\frac{\lambda}{\lambda_0}\right)^\alpha$$

The interest of this formulation is that it provides to the clear water atmospheric correction an atmospheric path signal spectrally smooth (see section 4.1.4). If we neglect the smile correction in the aerosol term, it also amounts to removing the residual from the modeled marine signal, i.e. $t(\lambda)\rho_{wc2}(\lambda) \approx t(\lambda)\rho_w(\lambda) - r(\lambda)$.

The pseudo-code is as follows:

Compute marine reflectance at band 779 and 865 for downstream clear water atmospheric correction. Note here that the theoretical wavelength should be used in the aerosol reflectance to get an atmospheric contribution fully corrected for smile effect.

$$\rho_{wc2}(779) = \left(\rho_{Rc}(779) - \rho_{as}(\lambda_0) \left(\frac{779}{\lambda_0}\right)^\alpha\right) / t(779)$$

$$\rho_{wc2}(865) = \left(\rho_{Rc}(865) - \rho_{as}(\lambda_0) \left(\frac{865}{\lambda_0}\right)^\alpha\right) / t(865)$$

3.5.4 Input uncertainty estimate

Uncertainty terms $1/\sigma(\lambda)$ weighting the χ^2 function play a significant role in the minimization. As we deal here with a spectral matching algorithm, it is important to estimate the spectral variation of this uncertainty, rather than its absolute value (which would only scale the χ^2). We consider there is no error in the independent variables λ , and only uncertainties in the dependent variables $\rho_{Rc}(\lambda)$, or equivalently in $\rho_{gc}(\lambda)$ if we deal with absolute error and assume no error in the Rayleigh subtraction. Hence a natural choice is to take

$$\sigma(\lambda) = \sigma_{\rho_{gc}}(\lambda)$$

Error in the modeling is potentially important at high turbidity, as discussed in section 3.5.1 concerning the fixed parameters, but in practice we have observed that its spectral variation is weaker than that of $\rho_{RC}(\lambda)$ radiometry. Indeed over turbid waters there is a large uncertainty at 709 nm and, in a less extent at 885 nm, due to erroneous water vapour correction, which does not take into account the ocean's brightness (Lindstrot 2011). This is illustrated on Figure 18 over Rio de la Plata, showing an error of around 4% on water vapour transmittance at 709 nm. This example shows that uncertainty must be computed on a pixel-by-pixel basis: over the turbid zone, bands 709 and 885 nm must be penalized in the χ^2 , while over clearer pixel radiometry at 709 nm is correct and informative about the marine contribution.

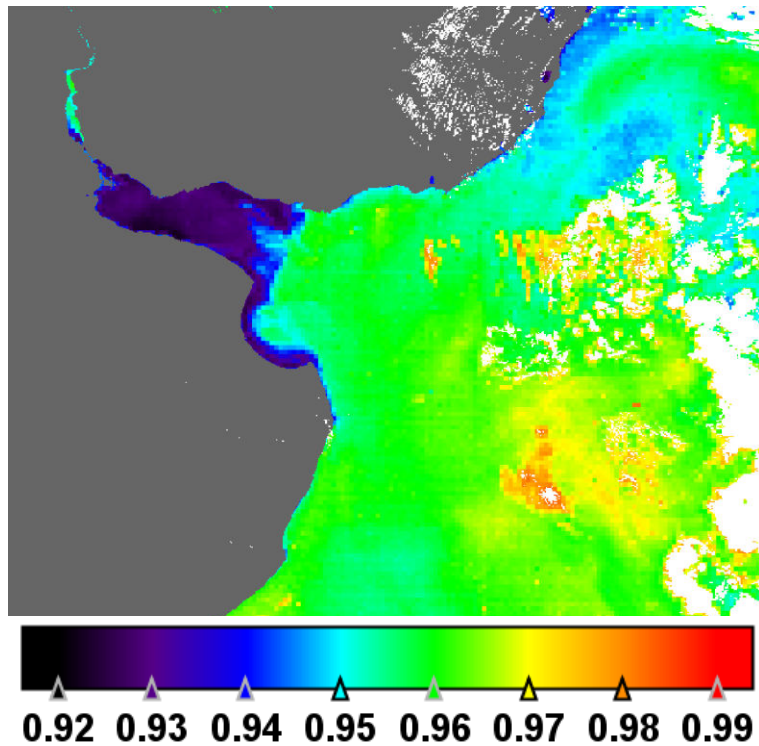


Figure 18 Water vapour transmittance at 709 nm over Rio de la Plata, as from MERIS 3rd reprocessing

The dynamic balance between bands is achieved by considering the general formulation of gaseous transmittance:

$$\rho_{gc}(\lambda) = t_g(\lambda)\rho_{toa}(\lambda) \quad \text{with } t_g(\lambda) = e^{-k(\lambda)*U*M}$$

Where $k(\lambda)$ is the effective absorption coefficient defined for a standard content, U is the actual absorber content and M the air-mass fraction of the actual viewing geometry. An uncertainty σ_U on the gas content implies an uncertainty on ρ_{gc} of

$$\begin{aligned}\sigma_{\rho_{gc}}(\lambda) &= -k(\lambda) * M * \sigma_U * t_g(\lambda) \rho_{toa}(\lambda) \\ &= \ln(t_g(\lambda)) \frac{\sigma_U}{U} \rho_{gc}(\lambda)\end{aligned}$$

This shows that as soon as there is any gas content, $t_g(\lambda) \neq 1$ and $\sigma_{\rho_{gc}}(\lambda) \neq 0$.

Because we are only interested in the spectral shape of σ , we can drop the unknown $\frac{\sigma_U}{U}$. Eventually we normalize the uncertainty so that the sum of the χ^2 weights amounts to N (number of bands). The pseudo-code is:

Compute rho_gc uncertainty and normalization factor

$\bar{w}=0$

$N=0$

For ($\lambda=\lambda_1; \lambda \leq \lambda_5; \lambda++$) **do**

$$\sigma_{\rho_{gc}}(\lambda) = \ln(t_g(\lambda)) \rho_{gc}(\lambda)$$

$N = N+1$

$$\bar{w} = \bar{w} + \frac{1}{(\sigma_{\rho_{gc}}(\lambda))^2}$$

Endfor

Normalize uncertainty

$\bar{w} = \bar{w}/N$

For ($\lambda=\lambda_1; \lambda \leq \lambda_5; \lambda++$) **do**

$$\sigma^2(\lambda) = (\sigma_{\rho_{gc}}(\lambda))^2 * \bar{w}$$

Endfor

3.5.5 First guess retrieval

The goal of the first guess retrieval is to find a realistic estimate of $(\rho_{as}(\lambda_0), \alpha, b_{bp}(\lambda_0))$, crucial for proper convergence of the χ^2 multidimensional minimisation. However without any a priori classification for

clear/turbid water, computing such first guess is a difficult task because the particulate backscattering can potentially cover a large range of variation.

A tentative procedure, based on MERIS 2nd reprocessing scheme, consists in starting from pure seawater and increasing progressively the sediment load with a 3-bands iterative scheme. The first drawback of such approach is a low convergence for very turbid waters. Second, the choice of the 3-bands may converge to totally wrong estimate, with artificially high aerosol load and low marine signal. The reason is that inverting $(\rho_{as}(\lambda_0), \alpha, b_{bp}(\lambda_0))$ from three bands is an ambiguous problem at high turbidity, as illustrated on Figure 19 with 709, 779 and 865 nm. In this example, starting from pure seawater would converge to the first minima (TSM ~ 25 mg/L), and lead to a wrong first guess. Hence such 3-band iterative approach is not retained.

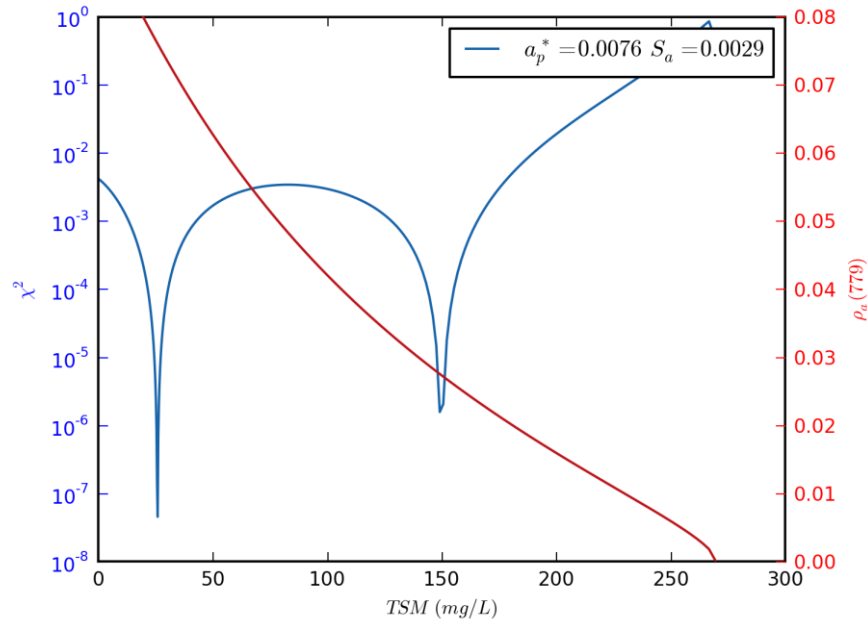


Figure 19 Multiple-minima issue of the 3-band iterative scheme over a turbid pixel. Blue curves displays χ^2 constructed by 3 bands (709, 779, 865) as function of TSM. Red curve is the associated aerosol content at 779 nm.

A more robust way is to search for a realistic range of $b_{bp}(\lambda_0)$ allowed by the TOA radiometry. For this the idea is to rely on the domain of validity of the aerosol content, which is more constrained than the marine signal. From the basic relationship $\rho_{RC}(\lambda) = t(\lambda)\rho_w(\lambda) + \rho_{as}(\lambda)$, any bound on the aerosol can be transferred to ρ_w . In most atmospheric conditions, $\rho_{as}(\lambda_0)$ and α are bounded:

$$\rho_{as0_min} \leq \rho_{as}(\lambda_0) \leq \rho_{as0_max}$$

$$\alpha_{min} \leq \alpha \leq \alpha_{max}$$

The minimum value ρ_{a0_min} is theoretically zero (no aerosol at all) and set to 1.E-6 in the following. Radiative transfer look-up tables of the clear water atmospheric correction (Antoine and Morel 1999) provide the other bounds used in MERIS:

$$\rho_{as0_max} = 0.08, \quad \alpha_{min} = -2.5 \quad \text{and} \quad \alpha_{max} = +0.5$$

We then deduce the domain of validity of $\rho_{as}(\lambda)$ at any band, thanks to its linear spectral shape in log/log scale (equation not detailed, see Figure 20).

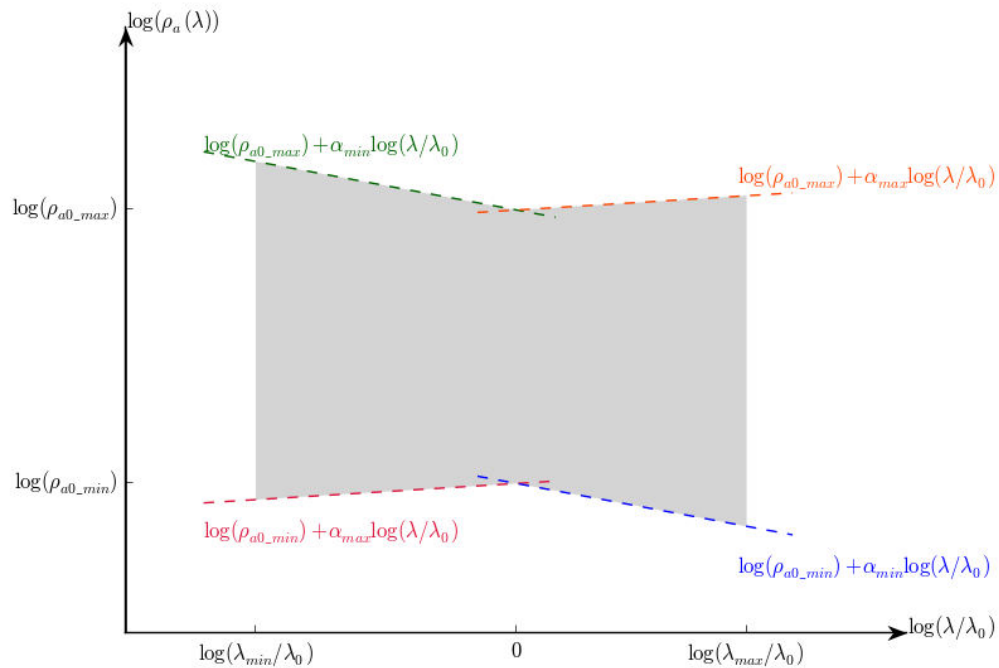


Figure 20 Domain of validity of $\rho_a(\lambda)$, in grey, as a function of wavelength, in log/log scale, due to bounds in $\rho_{as}(\lambda_0)$ and α .

Bounds on aerosol can be directly transferred on the marine reflectance:

$$\left\{ \begin{array}{l} \frac{\rho_{RC}(\lambda) - \rho_{as0_max} \left(\frac{\lambda_{pix}}{\lambda_0}\right)^{\alpha_{max}}}{t(\lambda)} \leq \rho_w(\lambda) \leq \frac{\rho_{RC}(\lambda) - \rho_{as0_min} \left(\frac{\lambda_{pix}}{\lambda_0}\right)^{\alpha_{min}}}{t(\lambda)} \quad \text{when } \lambda \geq \lambda_0 \\ \frac{\rho_{RC}(\lambda) - \rho_{as0_max} \left(\frac{\lambda_{pix}}{\lambda_0}\right)^{\alpha_{min}}}{t(\lambda)} \leq \rho_w(\lambda) \leq \frac{\rho_{RC}(\lambda) - \rho_{as0_min} \left(\frac{\lambda_{pix}}{\lambda_0}\right)^{\alpha_{max}}}{t(\lambda)} \quad \text{when } \lambda \leq \lambda_0 \end{array} \right.$$

For each band, the four associated $b_{bp}(\lambda)$ are retrieved using the inversion of $\rho_w(\lambda)$ described in section 3.5.6. The admissible minimum and maximum $b_{bp}(\lambda_0)$ are then computed over all bands, and the mean is taken as first guess.

Eventually, first guess values of $\rho_{as}(\lambda_0)$ and α result from fitting the aerosol power-law shape on $\rho_{RC}(\lambda) - t(\lambda)\rho_w(\lambda)$, over all five bands and taking into account uncertainties, where $\rho_w(\lambda)$ is computed by the above mean $b_{bp}(\lambda_0)$. This is a linear least-square problem in log/log scale for variables (x_i, y_i) defined by:

$$x_i = \ln \frac{\lambda_{pix,i}}{\lambda_0} \quad \text{and} \quad y_i = \ln(\rho_{RC}(\lambda_i) - t(\lambda_i)\rho_w(\lambda_i))$$

The solution is simply given by

$$\alpha = \frac{cov(x, y)}{var(x)}, \quad \ln \rho_{as}(\lambda_0) = mean(y) - \alpha * mean(x)$$

Where all statistical operators (covariance, variance, mean) are weighted by the uncertainties $1/\sigma(\lambda_i)$.

An example of such procedure is provided on Figure 21. Over clear water (left image), the range of admissible turbidity expressed in TSM unit goes from nearly zero to 8 mg/L, yielding to an average TSM of 4 mg/L, close to the optimal solution of about 0.6 mg/L. Over very turbid water (right image), the admissible range is [20, 270] with an average of about 145 mg/L, in good accordance with the optimum of about 210 mg/L.

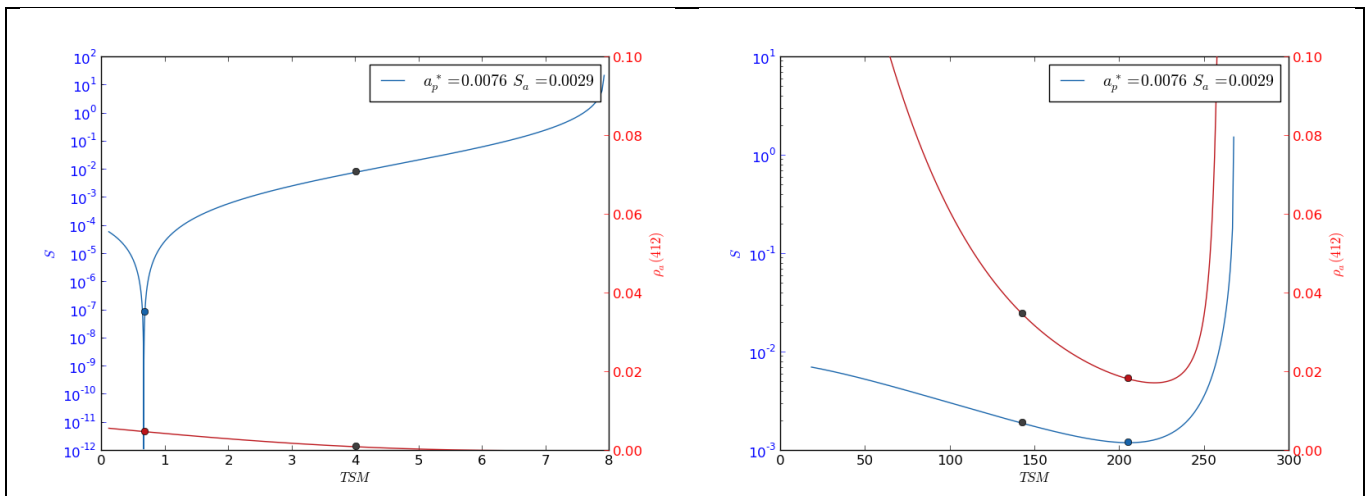


Figure 21 Range of admissible TSM (x-axis) found by the first guess retrieval for a clear pixel (left) and a turbid pixel (right). Blue curve represents the χ^2 on five bands as function of TSM, red curves is the associated aerosol signal. Grey dots is the first guess value, averaged from TSM extrema. Blue and red dots correspond to the χ^2 minimum.

The pseudo-code for the first guess retrieval is as follows. The tabulated range for bbp is $bbp0_range = \{0.001; 10\}$.

Initialise min and max bbp

bbp0_min = bbp0_range(0)

bbp0_max = bbp0_range(1)

Loop over bands

For ($\lambda = \lambda_1$; $\lambda \leq \lambda_5$; $\lambda++$) **do**

Compute min rhow

If $\lambda \leq \lambda_0$ **do**

$$\rho_w(\lambda) = \frac{\rho_{RC}(\lambda) - \rho_{aso_max} \left(\frac{\lambda_{pix}}{\lambda_0} \right)^{\alpha_{min}}}{t(\lambda)}$$

Else

$$\rho_w(\lambda) = \frac{\rho_{RC}(\lambda) - \rho_{aso_max} \left(\frac{\lambda_{pix}}{\lambda_0} \right)^{\alpha_{max}}}{t(\lambda)}$$

Endif

Retrieve min bbp

If $\rho_w(\lambda) > 0$ **do**

$$b_{bp}(\lambda) = rhow_to_bbp(\rho_w(\lambda), \lambda)$$

$$b_{bp}(\lambda_0) = b_{bp}(\lambda_1) \frac{b_{bp}^*(\lambda_0)}{b_{bp}^*(\lambda)}$$

$$bbp0_min = \max(bb p0_min, b_{bp}(\lambda_0))$$

Endif

Compute max rhow

If $\lambda \leq \lambda_0$ **do**

$$\rho_w(\lambda) = \frac{\rho_{RC}(\lambda) - \rho_{aso_min} \left(\frac{\lambda_{pix}}{\lambda_0} \right)^{\alpha_{max}}}{t(\lambda)}$$

Else

$$\rho_w(\lambda) = \frac{\rho_{RC}(\lambda) - \rho_{as0_min} \left(\frac{\lambda_{pix}}{\lambda_0} \right)^{\alpha_{min}}}{t(\lambda)}$$

Endif

Retrieve max bbp

If $\rho_w(\lambda) > 0$ **do**

$$b_{bp}(\lambda) = r_{how_to_bbp}(\rho_w(\lambda), \lambda)$$

$$b_{bp}(\lambda_0) = b_{bp}(\lambda_1) \frac{b_{bp}^*(\lambda_0)}{b_{bp}^*(\lambda)}$$

$$bbp0_max = \min(bbp0_max, b_{bp}(\lambda_0))$$

Endif

Endfor

Average bbp

$$b_{bp}(\lambda_0) = (bbp0_min + bbp0_max) / 2$$

Compute marine signal at all bands

For ($\lambda = \lambda_1; \lambda \leq \lambda_5; \lambda++$) **do**

Compute particulate backscattering

$$b_{bp}(\lambda) = b_{bp}(\lambda_0) \frac{b_{bp}^*(\lambda)}{b_{bp}^*(\lambda_0)}$$

Compute particulate absorption

$$a_p(\lambda) = b_{bp}(\lambda) * a_{p_bp}(\lambda)$$

Compute single scattering albedo and η

$$\omega(\lambda) = \frac{b_{bw}(\lambda) + b_{bp}(\lambda)}{a_w(\lambda) + a_p(\lambda) + b_{bw}(\lambda) + b_{bp}(\lambda)}$$

$$\eta(\lambda) = \frac{b_{bw}(\lambda)}{b_{bw}(\lambda) + b_{bp}(\lambda)}$$

Compute F' factor

$$F'(\lambda, \eta, \omega) = A_0(\lambda) + C(\lambda)\eta + a_0(\lambda) + a_1(\lambda)\omega + a_2(\lambda)\omega^2 + a_3(\lambda)\omega^3 + a_4(\lambda)\omega^4$$

Compute marine reflectance

$$\rho_w(\lambda) = F'(\lambda, \eta, \omega) * \omega(\lambda)$$

Endfor

Compute rhoa0 and alpha by a linear least-square fit in log/log scale

$$mean_x = 0$$

$$mean_y = 0$$

$$var_x = 0$$

$$cov_xy = 0$$

For ($\lambda=\lambda_1$; $\lambda \leq \lambda_5$; $\lambda++$) **do**

$$mean_x = mean_x + \ln\left(\frac{\lambda_{pix}}{\lambda_0}\right) / \sigma^2(\lambda)$$

$$mean_y = mean_y + \ln(\rho_{RC}(\lambda) - t(\lambda)\rho_w(\lambda)) / \sigma^2(\lambda)$$

Endfor

$$mean_x = mean_x / N$$

$$mean_y = mean_y / N$$

For ($\lambda=\lambda_1$; $\lambda \leq \lambda_5$; $\lambda++$) **do**

$$var_x = var_x + \left(\ln\left(\frac{\lambda_{pix}}{\lambda_0}\right) - mean_x\right)^2 / \sigma^2(\lambda)$$

$$cov_xy = cov_xy + \left(\ln\left(\frac{\lambda_{pix}}{\lambda_0}\right) - mean_x\right) \left(\ln(\rho_{RC}(\lambda) - t(\lambda)\rho_w(\lambda)) - mean_y\right) / \sigma^2(\lambda)$$

Endfor

$$\alpha = cov_xy / var_x$$

$$\rho_{as}(\lambda_0) = e^{mean_y - \alpha * mean_x}$$

Save first guess

$$\rho_{as}(\lambda_0)_{init} = \rho_{as}(\lambda_0)$$

$$\alpha_{init} = \alpha$$

$$b_{bp}(\lambda_0)_{init} = b_{bp}(\lambda_0)$$

3.5.6 Determination of bb from $\rho_w(\lambda)$

The algorithm needs to invert the marine reflectance at one band into b_{bp} ; this is achievable due to the monotonous variation of marine signal (see e.g. Figure 1) and in practice we use exactly the same *rhow_to_bbp* routine as that implemented for 3rd reprocessing reminded hereafter.

Given:

$$\rho_w(\lambda) = F \cdot a(\lambda) / [a(\lambda) + bb_w(\lambda) + bb_p(\lambda)]$$

bb_p can be inverted as :

$$bb_p(\lambda) = [\rho_w(\lambda) \cdot a(\lambda)] / [F' - \rho_w(\lambda)] - bb_w(\lambda)$$

In Case 1 waters this does not present a problem since $\rho_w(\lambda) \ll F'$, and the can be iterated since $a(\lambda) = aw'(\lambda) + \alpha_{bb}^*(\lambda) * bb_p(\lambda)$, convergence is simple achieved using $\Delta bb_p(\lambda)$ as a convergence criteria.

Highly turbid Case 2 waters present a problem, since $\rho_w(\lambda)$ can be $>$ or equal F' , as a result there is either an arithmetic error, where the denominator above becomes zero or a negative $bb_p(\lambda)$ is determined. In this case an estimate of $bb_p(\lambda)$ is obtained F , where:

$$F = F' \cdot a(\lambda) / [a(\lambda) + bb(\lambda) + bb_w(\lambda)]$$

and:

$$bb_p(\lambda) = [\rho_w(\lambda) \cdot a(\lambda)] / F - bb_w(\lambda)$$

This is iterated using the above relationship for $a(\lambda)$, and convergence is achieved when $F' > \rho_w(\lambda)$. Thereafter, the Case 1 iterative method is used.

3.6 Validation

3.6.1 Numerical check against simulated data

We have checked perfect convergence of the full algorithm (i.e. first guess followed by χ^2) against simulated data of various atmospheric and marine content, when the TOA signal exactly match the model (Figure 22). In these simulations TSM ranges from 10^{-2} (virtually zero) to 100 g/m³, Angstrom exponent takes values of -0.5, -1.5 and -2.5 and aerosol reflectance takes values of 0.005, 0.08 and 0.15. Results are shown in term of marine reflectance at 779 nm (same results at 865 nm) and in logarithmic scale, since it is important to retrieve all order of magnitude of the marine signal.

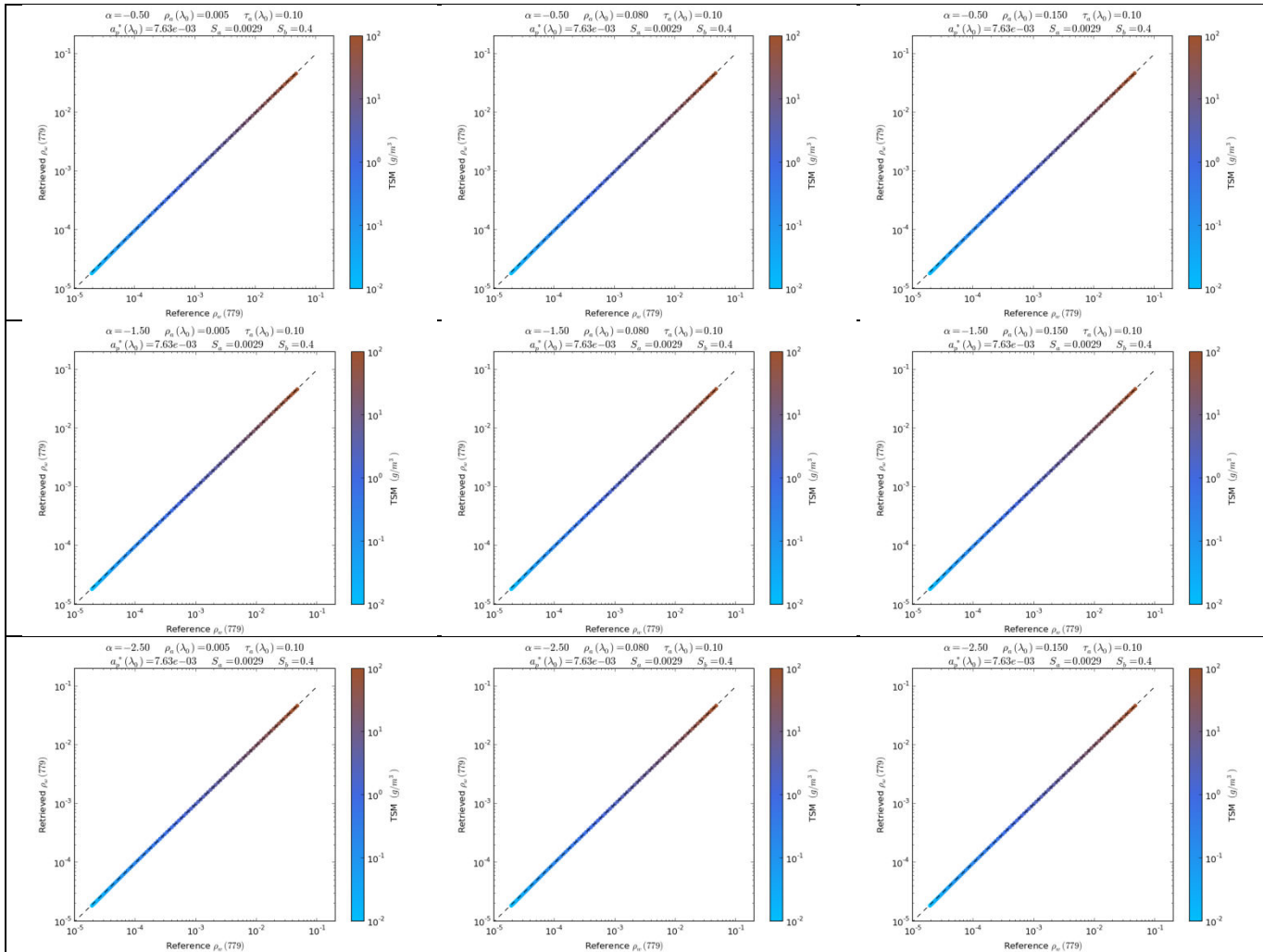


Figure 22 Comparison of retrieved marine reflectance (y-axis) with reference reflectance (x-axis) at 779 nm for simulated TOA spectra perfectly fitting the model. Color is TSM (from blue 10^{-2} to brown $100 g/m^3$). Rows from top to bottom are respectively for $\alpha = -0.5, -1.5, -2.5$ and columns from left to right are respectively for $\rho_{as}(\lambda_0) = 0.005, 0.08, 0.15$

3.6.2 Visual inspection over MERIS scenes

We present here inversion of real MERIS data over three different water types: the North Mediterranean Sea, the English Channel/Brittany and the Amazon River plume. Each scene is processed by two algorithms: nominal 3rd reprocessing versus current BPAC evolution and under two configurations: without vicarious calibration and with NIR vicarious calibration. All other parameters are strictly identical to MERIS 3rd reprocessing configuration. Figure 23 to Figure 31 compare these four processing chains for Angstrom exponent (retrieved by clear water atmospheric correction, after BPAC), marine reflectance at 443 nm and chlorophyll_1 concentration

On overall there is no drastic change in term of coverage or main visual aspect. A more detailed analysis shows however that:

- Activation of NIR vicarious calibration has less impact in the present evolution (visible in particular on the Angstrom coefficient);
- On the English Channel scene we now manage to converge on most of the Severn estuary with more realistic marine reflectance; there are however failure at the very entry of the estuary;
- For even more turbid water, the algorithm also manages to invert some arms of the Amazon River; there are still failures on the most of the plume, possibly because of absorption modelling.
- Adjacency effects seems to be automatically corrected with new approach – this is clearly visible in particular around Corsica.
- Camera interface and noise are also reduced (visible on the Amazone scene)

Quantitative performance is given in next section with matchups.

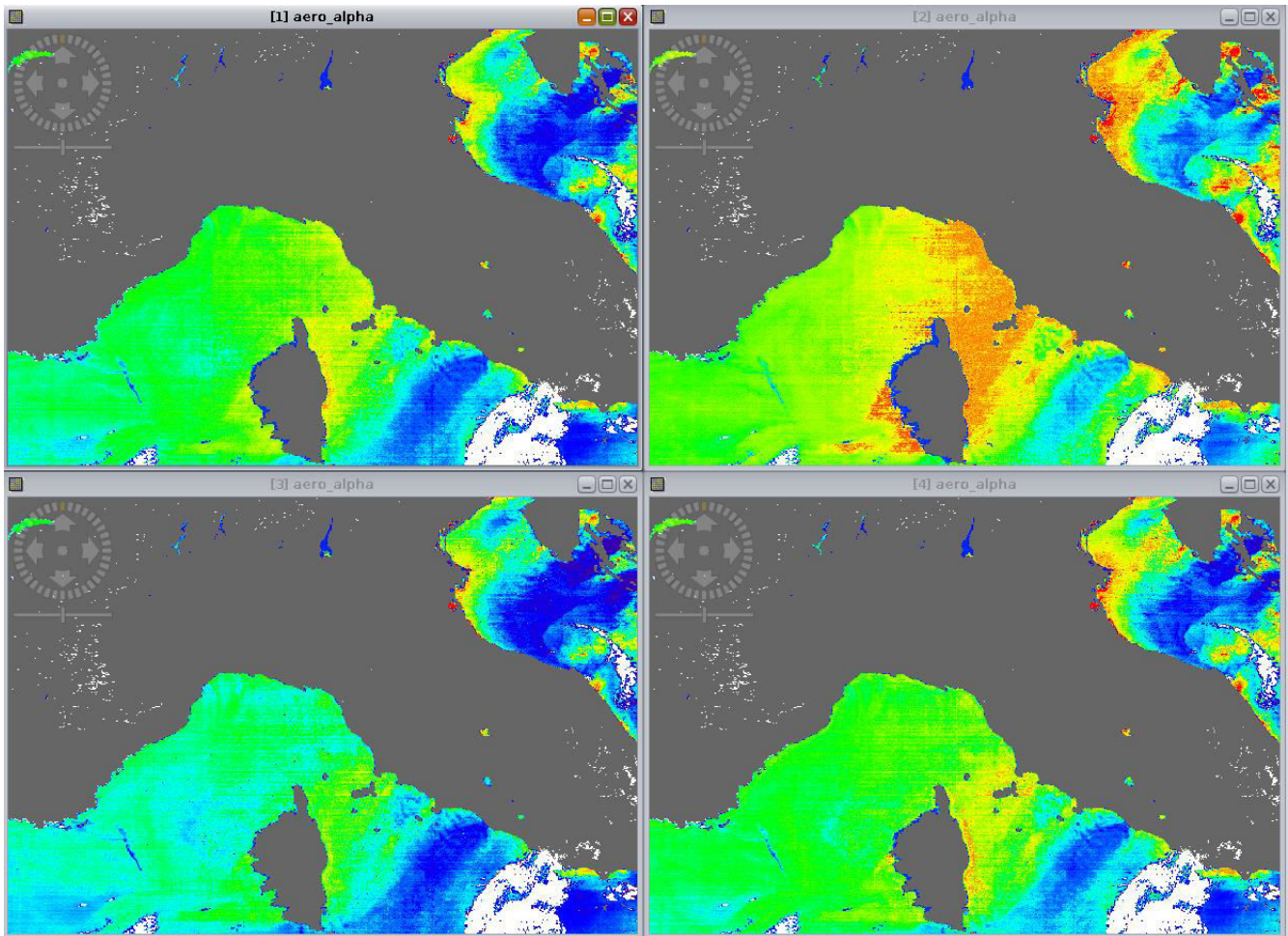


Figure 23 Angstrom exponent over the Mediterranean Sea with standard 3rd reprocessing BPAC (top) and present evolution (bottom), without vicarious calibration (left) and with NIR vicarious calibration (right)

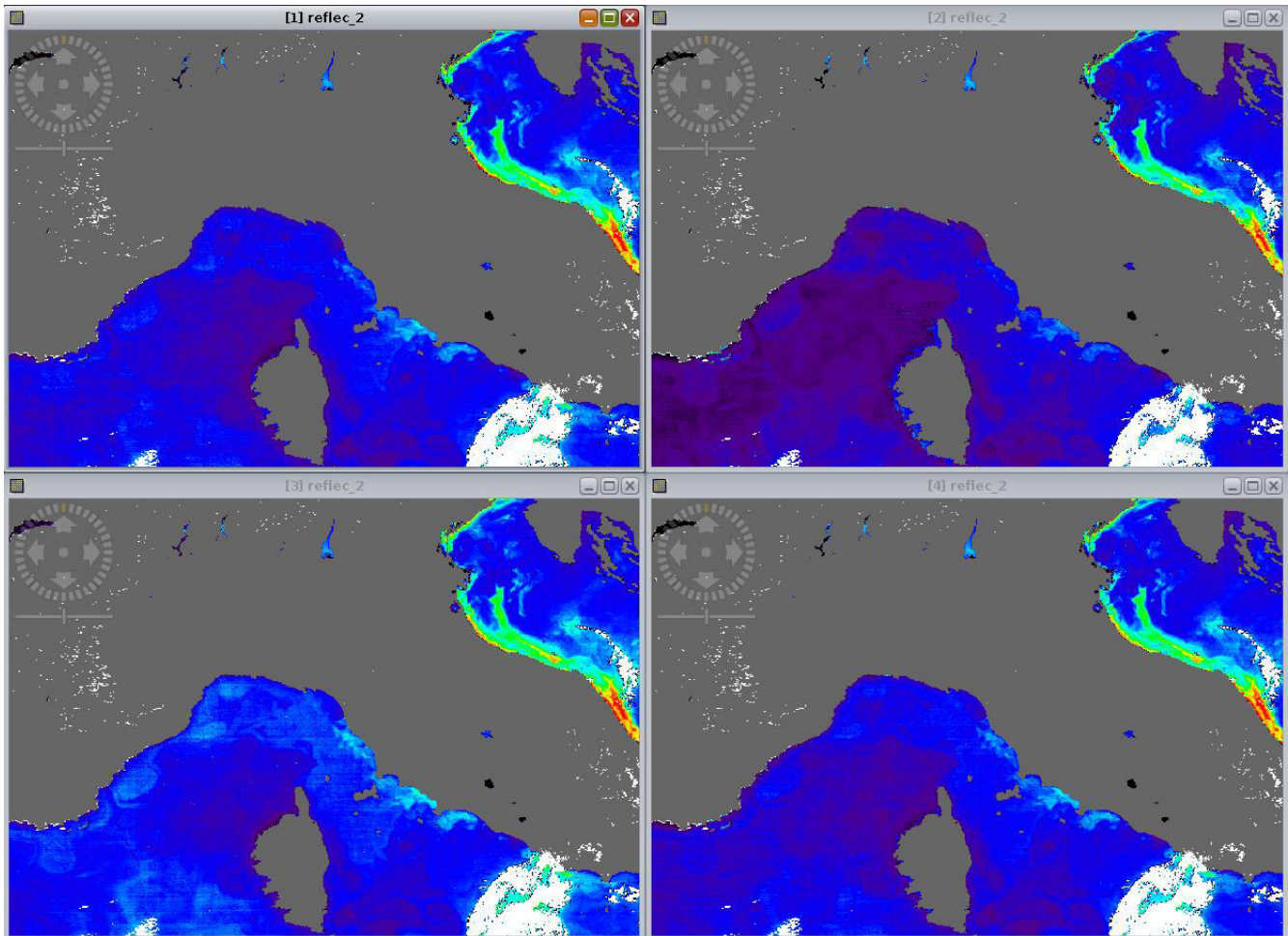


Figure 24 Marine reflectance at 443 nm over the Mediterranean Sea with standard 3rd reprocessing BPAC (top) and present evolution (bottom), without vicarious calibration (left) and with NIR vicarious calibration (right)

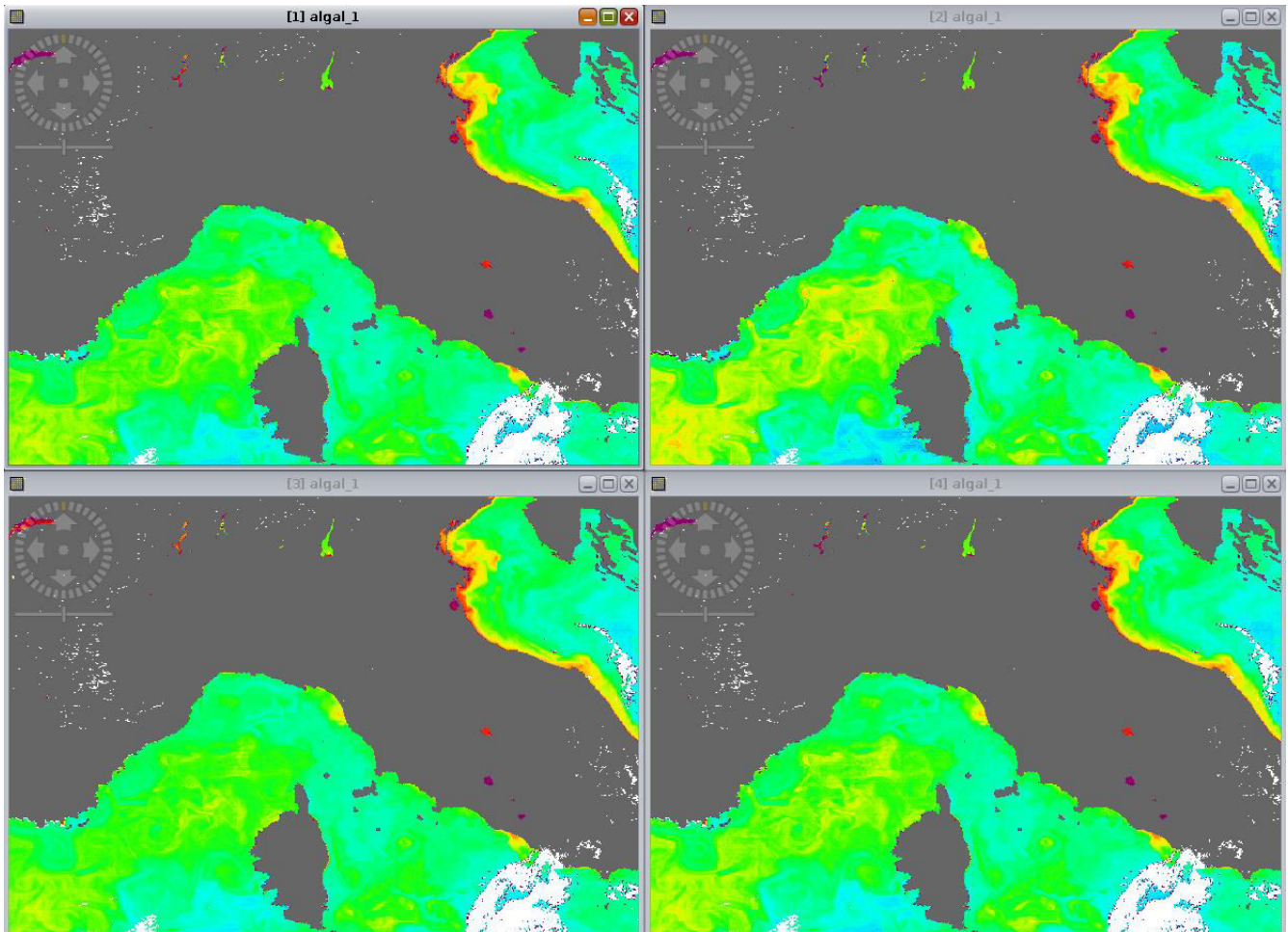


Figure 25 Chlorophyll_1 concentration over the Mediterranean Sea with standard 3rd reprocessing BPAC (top) and present evolution (bottom), without vicarious calibration (left) and with NIR vicarious calibration (right)

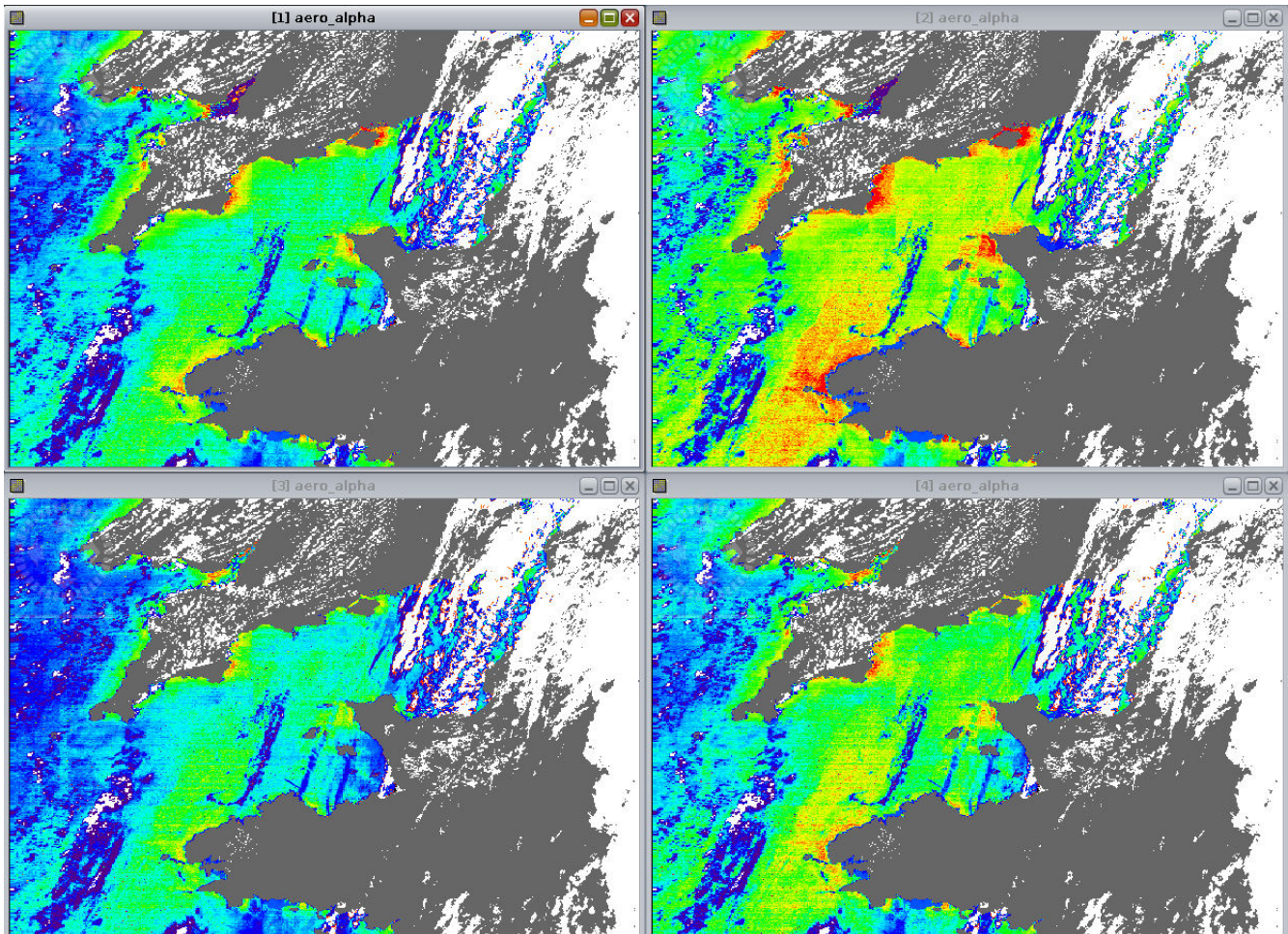


Figure 26 Angstrom exponent over the English Channel/Brittany with standard 3rd reprocessing BPAC (top) and present evolution (bottom), without vicarious calibration (left) and with NIR vicarious calibration (right)

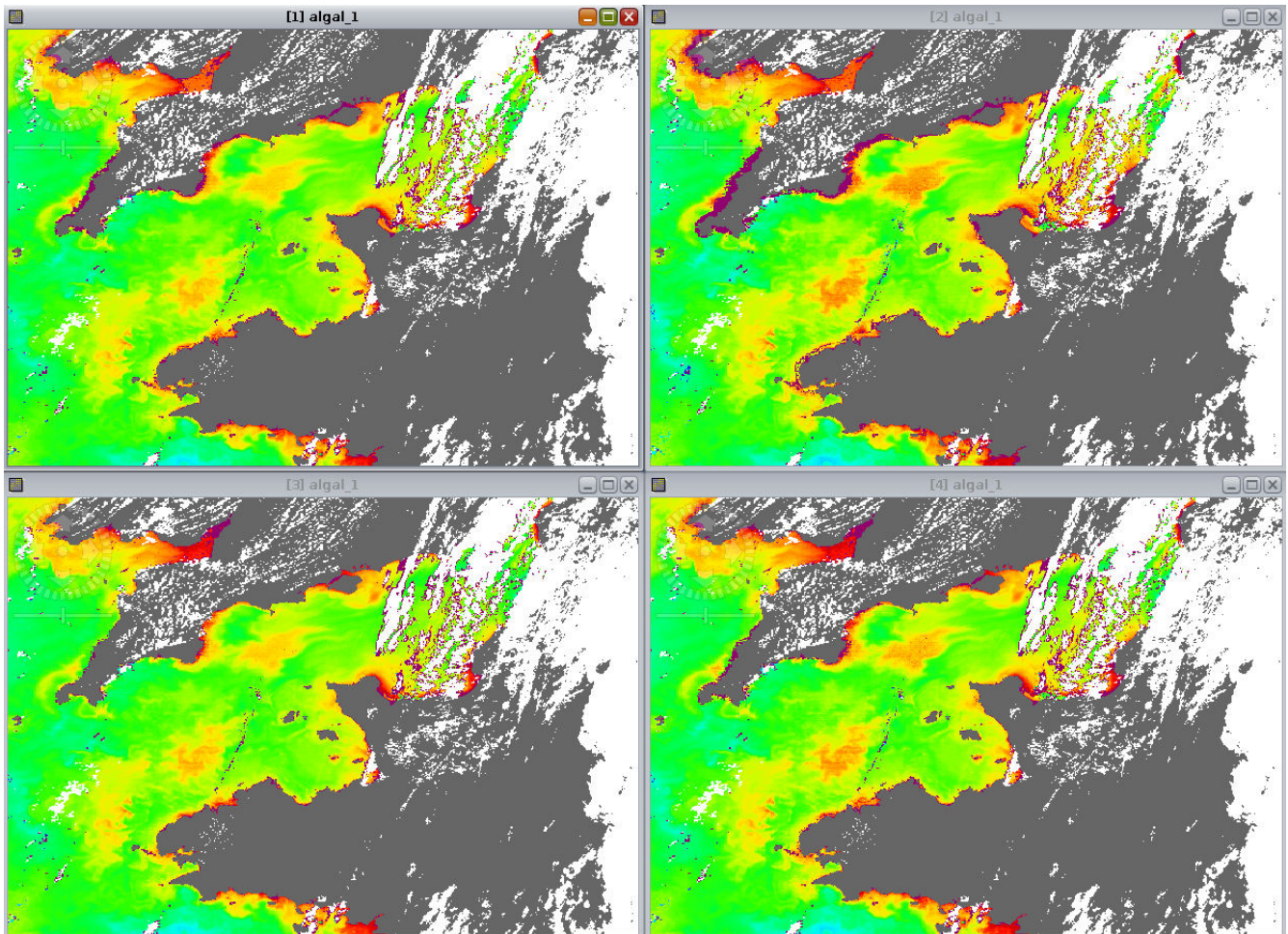


Figure 27 Chlorophyll_1 concentration over the English Channel/Brittany with standard 3rd reprocessing BPAC (top) and present evolution (bottom), without vicarious calibration (left) and with NIR vicarious calibration (right)

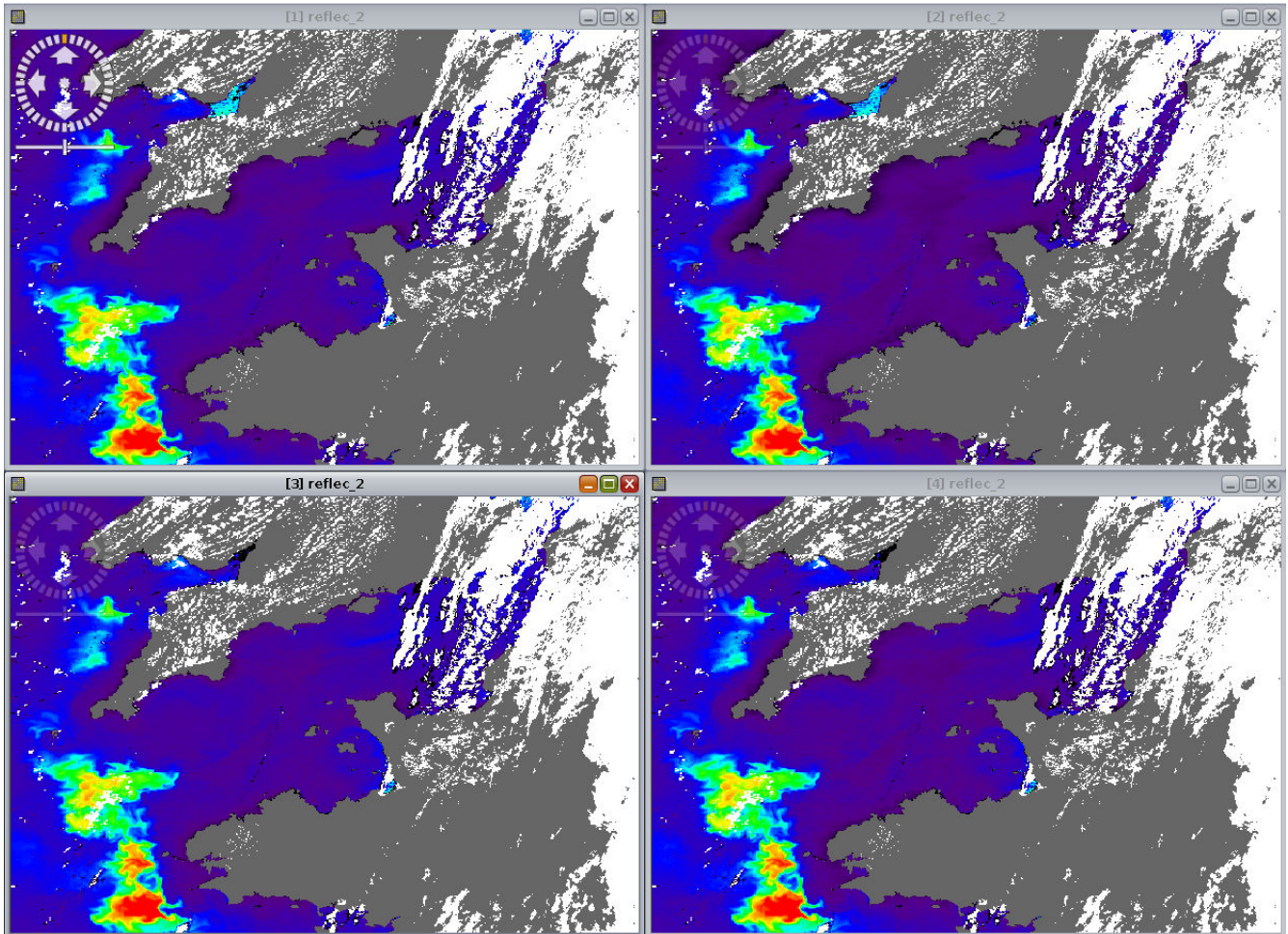


Figure 28 Marine reflectance at 443 nm over the English Channel/Brittany with standard 3rd reprocessing BPAC (top) and present evolution (bottom), without vicarious calibration (left) and with NIR vicarious calibration (right)

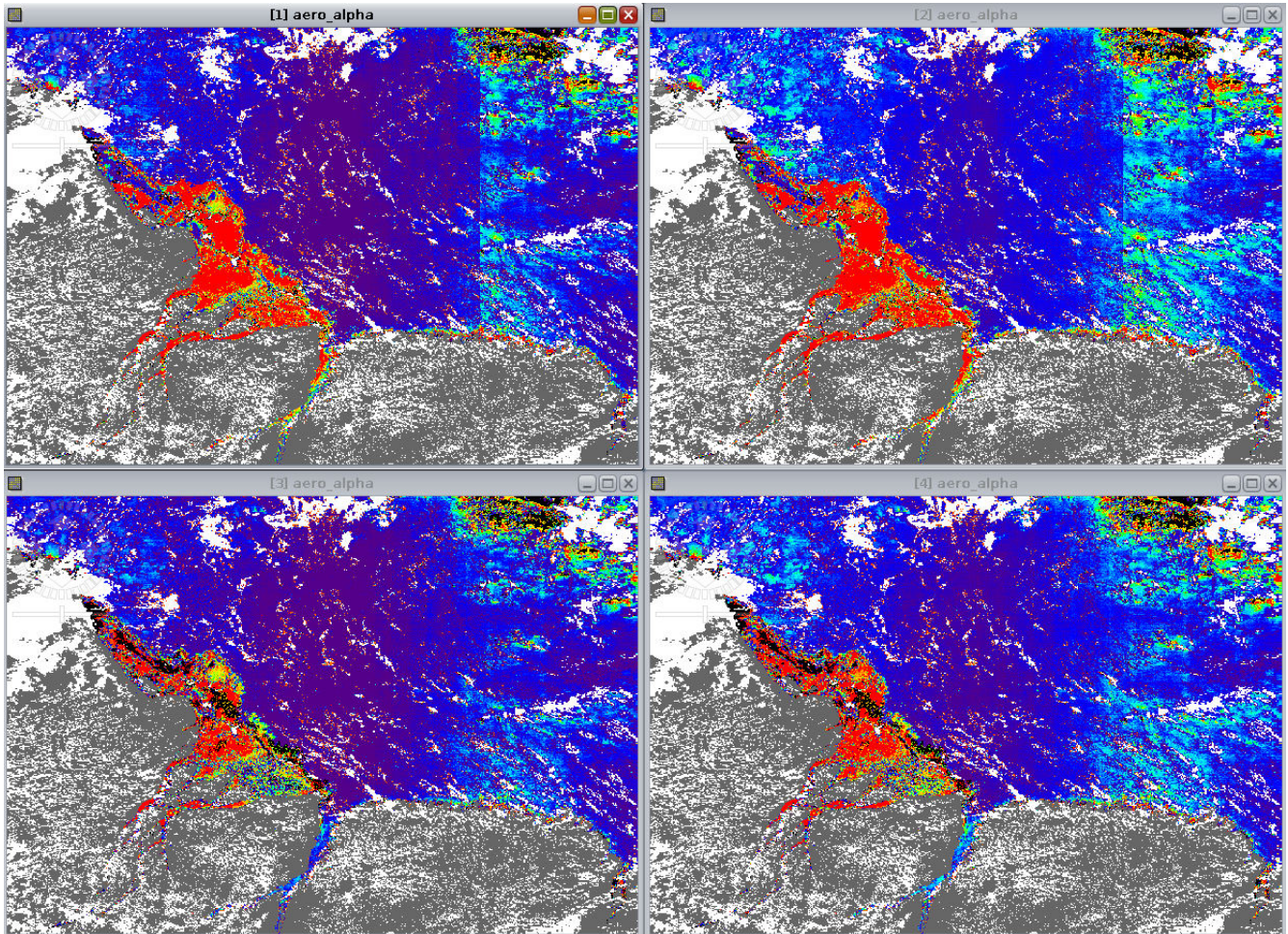


Figure 29 Angstrom exponent over the Amazon River with standard 3rd reprocessing BPAC (top) and present evolution (bottom), without vicarious calibration (left) and with NIR vicarious calibration (right)

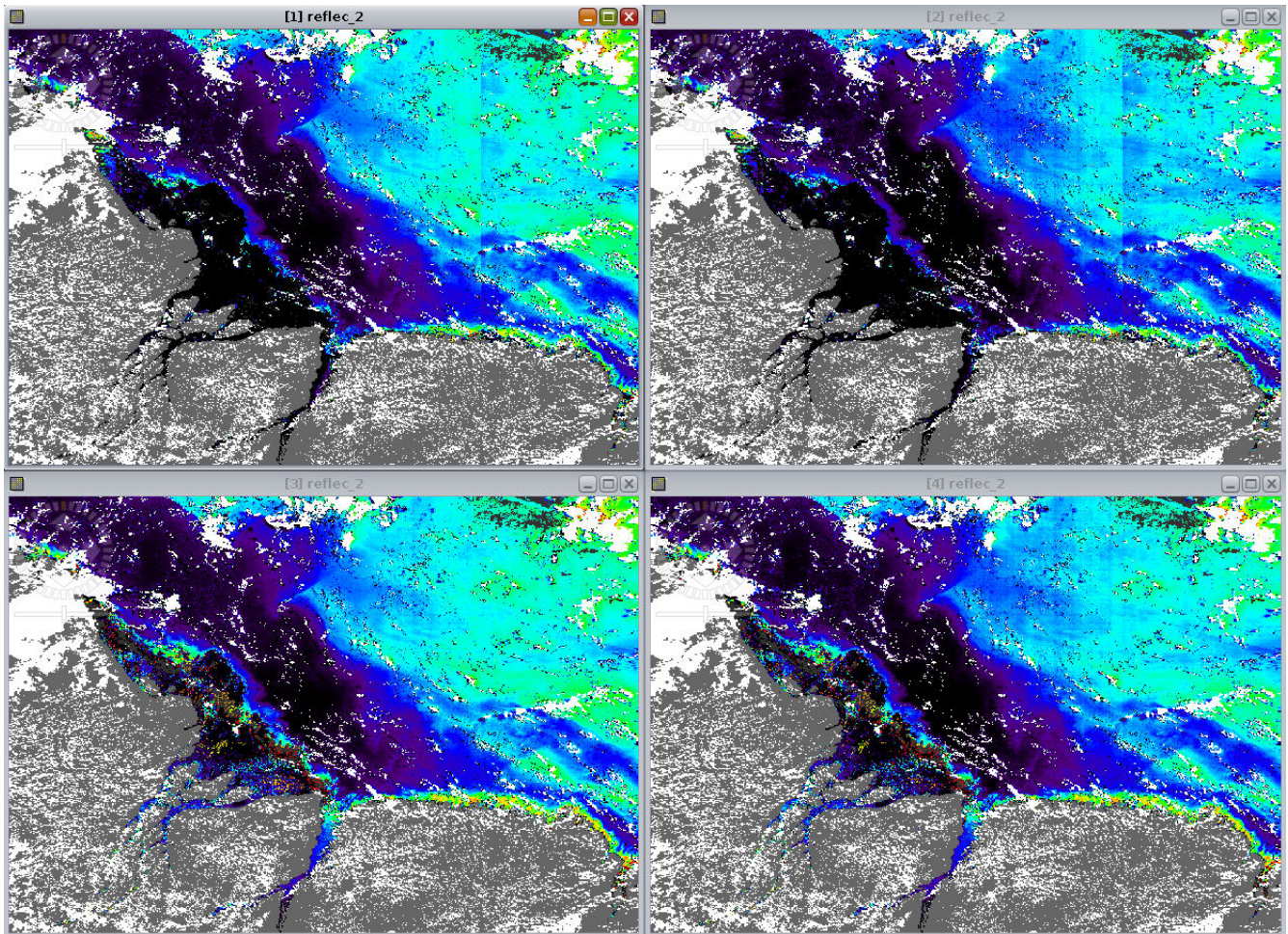


Figure 30 Marine reflectance at 443 nm over the Amazon River with standard 3rd reprocessing BPAC (top) and present evolution (bottom), without vicarious calibration (left) and with NIR vicarious calibration (right)

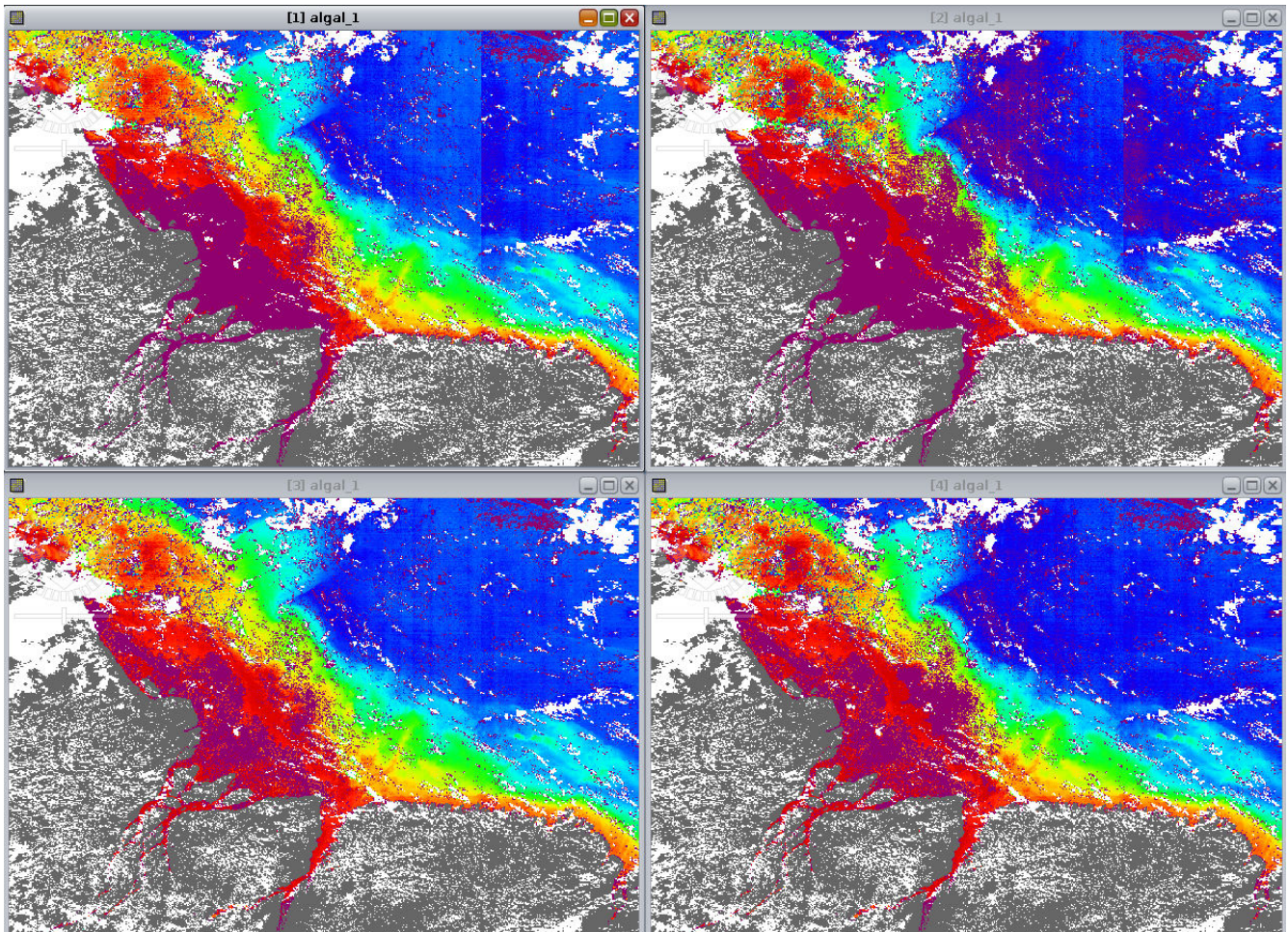


Figure 31 Chlorophyll_1 concentration over the Amazon River with standard 3rd reprocessing BPAC (top) and present evolution (bottom), without vicarious calibration (left) and with NIR vicarious calibration (right)

3.6.3 Validation against in-situ data

Quantitative validation is based on MERIS match-ups with in-situ data provided by the MERMAID database. We consider AAOT, BOUSSOLE and MOBY measurements. We accept 5x5 RR macro-pixel having less than 50% pixel flagged by either cloud, ice haze, medium glint, high glint or PCD_1_13.

Validation at AAOT on Figure 32 and Figure 33 are to be compared to respectively Figure 14 and Figure 15. The number of good data with vicarious NIR calibration is now as high as in the previous implementation without calibration and proves much better robustness of the approach to the NIR radiometry. It is worth noting that deactivating the calibration still brings new points in the present approach (about 150 points in the blue band).

Independently of more points, the r^2 coefficient is roughly the same between both implementations when deactivating NIR calibration. Without vicarious calibration the 3rd reprocessing at AAOT is less biased, which could be a first sight a better behaviour. However when looking simultaneously at AAOT, BOUSSOLE and MOBY validation, 3rd reprocessing yields to different bias at 412, 443 and 490 nm (reflectance clearly overestimated for MOBY and BOUSSOLE whereas aligned for AAOT), contrary to the new implementation showing consistent positive bias for all sites (Figure 34 versus Figure 36). Hence in view of visible vicarious calibration there is more chance to derive consistent gains for different water types with new implementation (possibly without any NIR calibration).

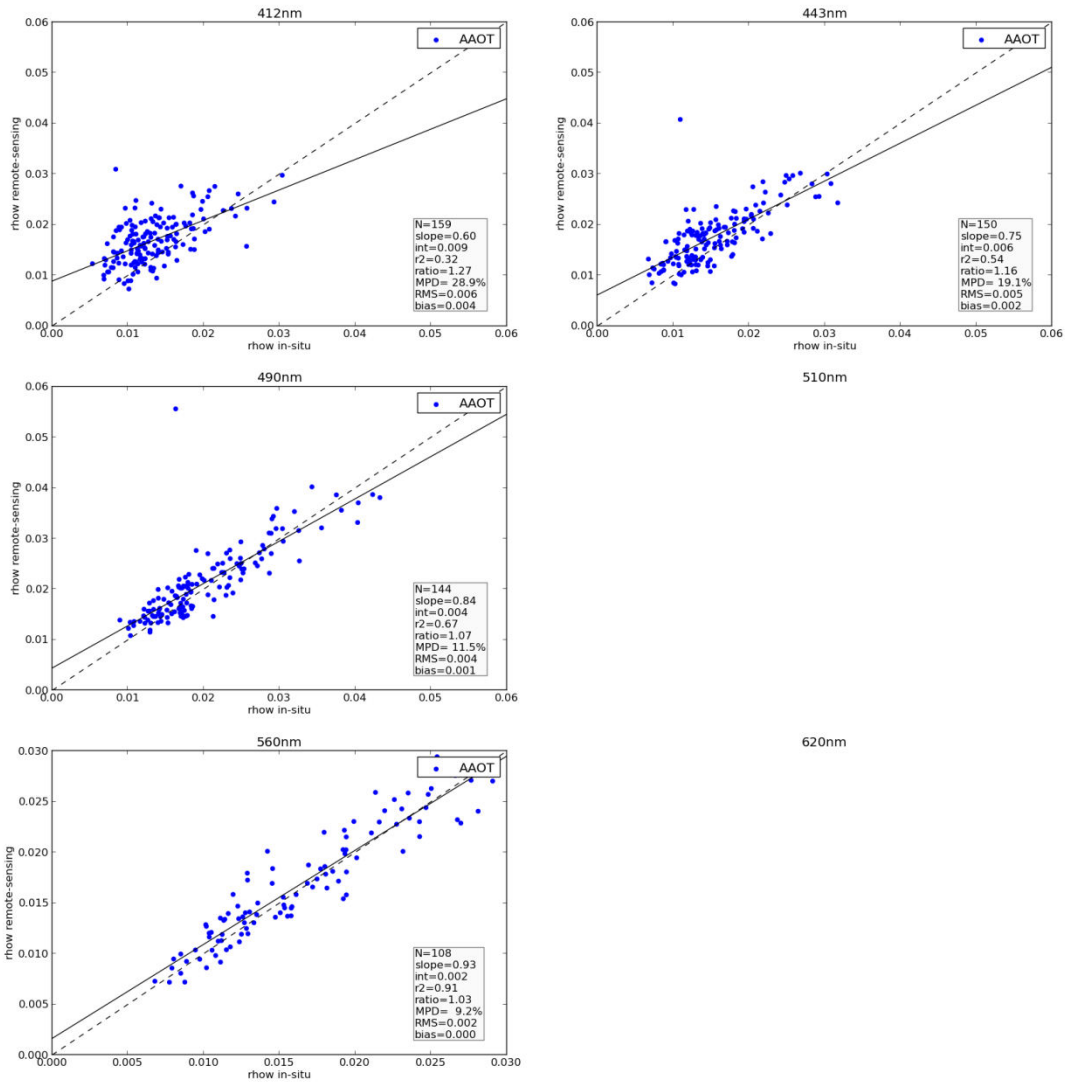


Figure 32 Validation of marine reflectance at AAOT with new implementation when vicarious calibration is deactivated

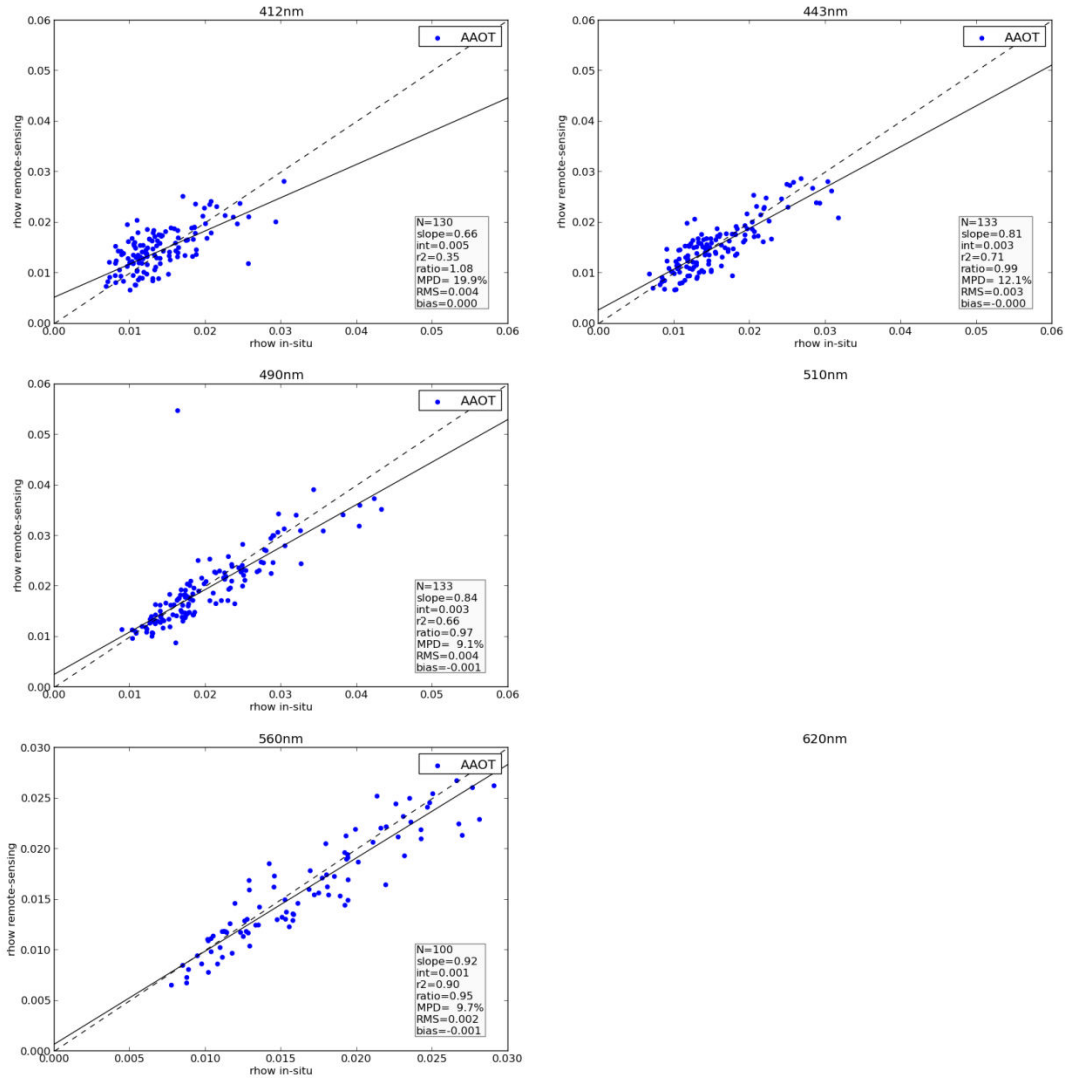


Figure 33 Validation of marine reflectance at AAOT with new implementation when activating NIR vicarious calibration

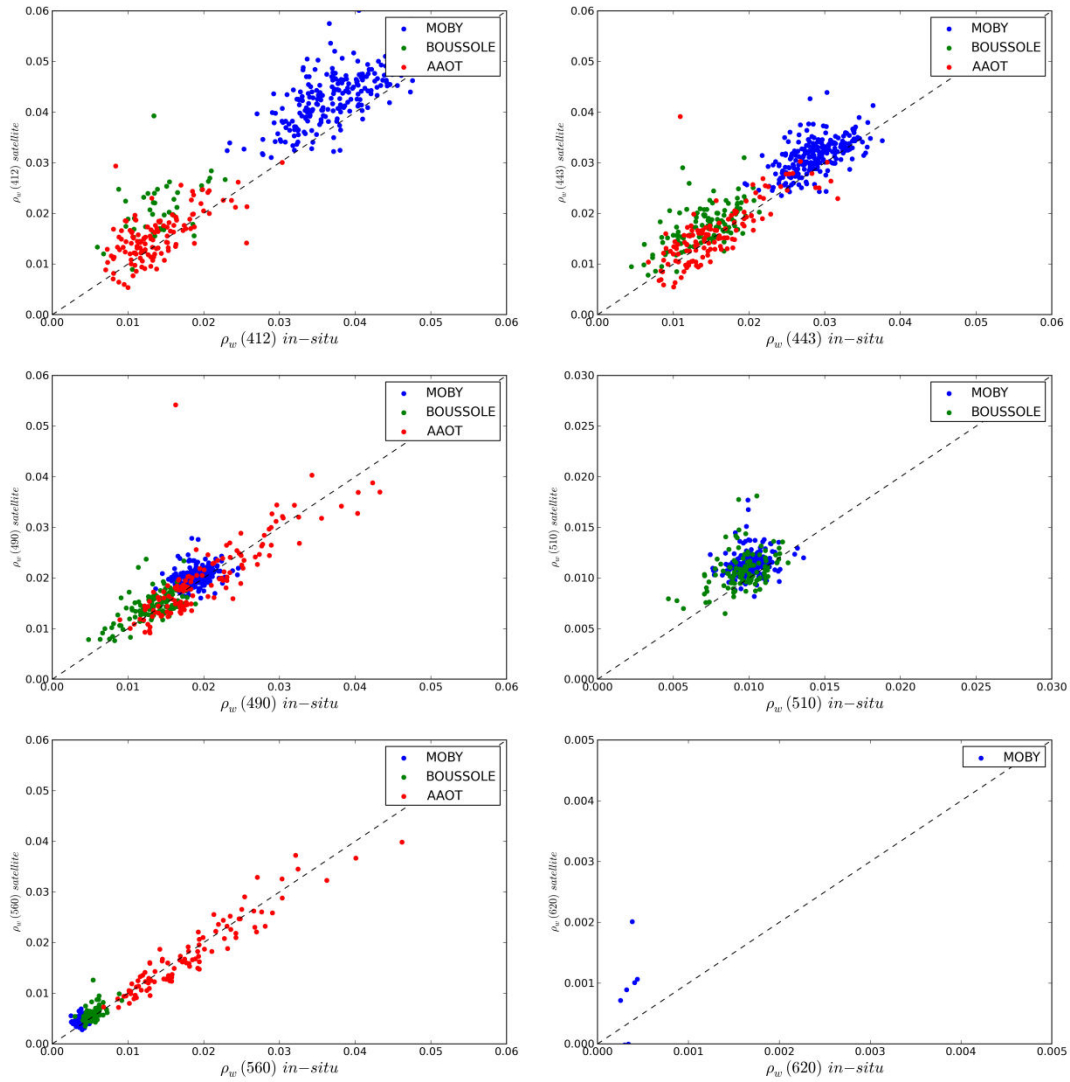


Figure 34 Validation of marine reflectance at MOBY, BOUSSOLE and AAOT with 3rd reprocessing implementation when vicarious calibration is deactivated

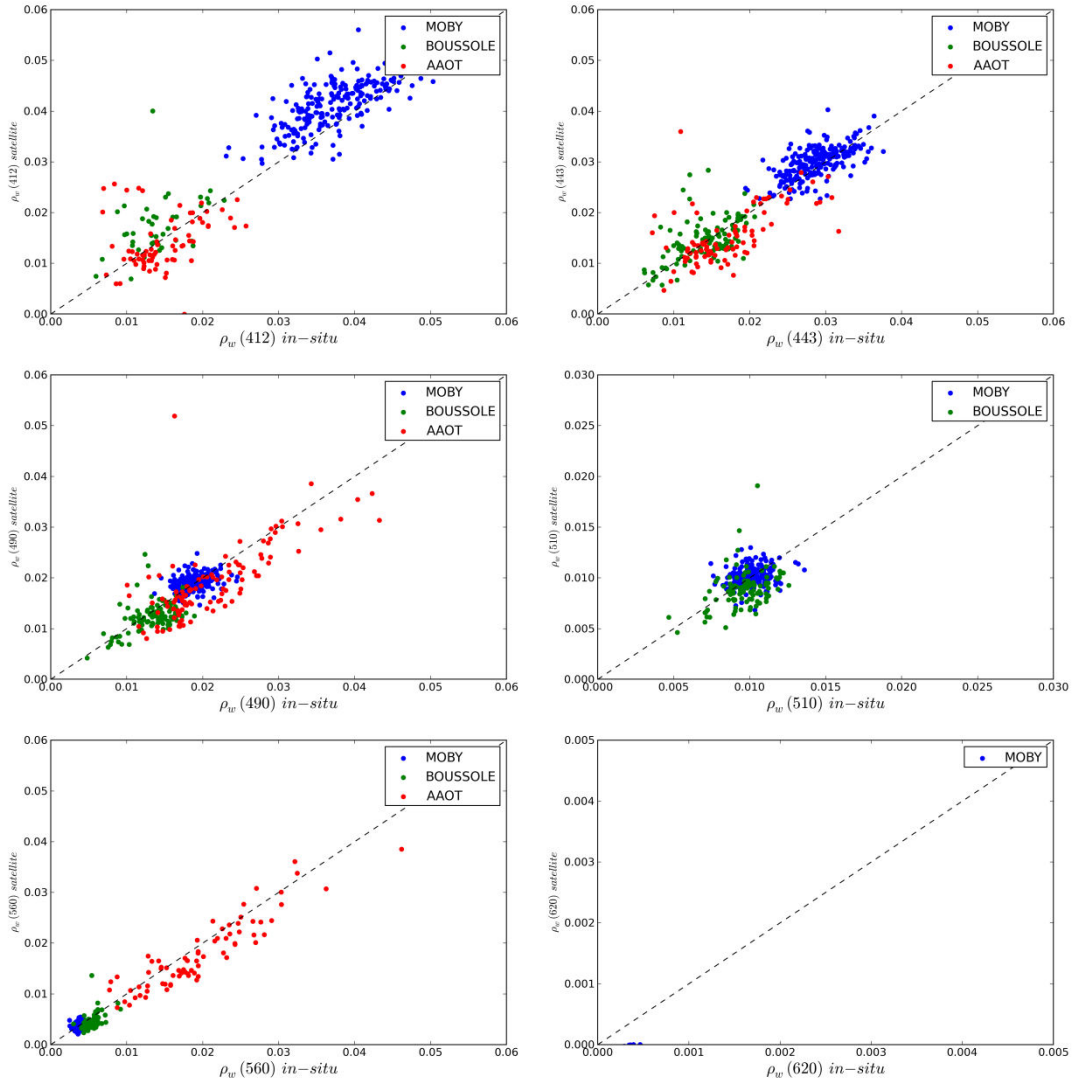


Figure 35 Validation of marine reflectance at MOBY, BOUSSOLE and AAOT with 3rd reprocessing implementation when activating NIR vicarious calibration

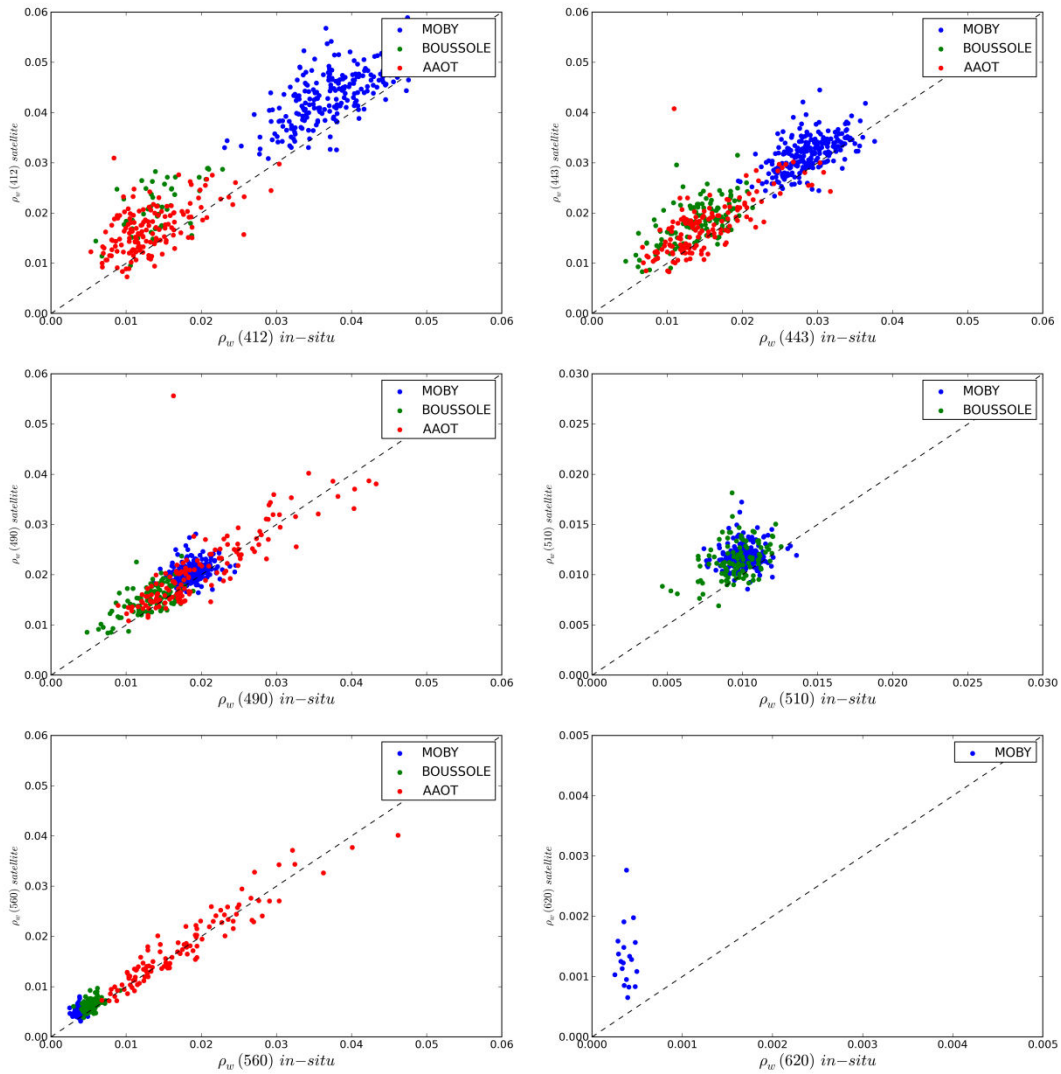


Figure 36 Validation of marine reflectance at MOBY, BOUSSOLE and AAOT with new implementation when vicarious calibration is deactivated

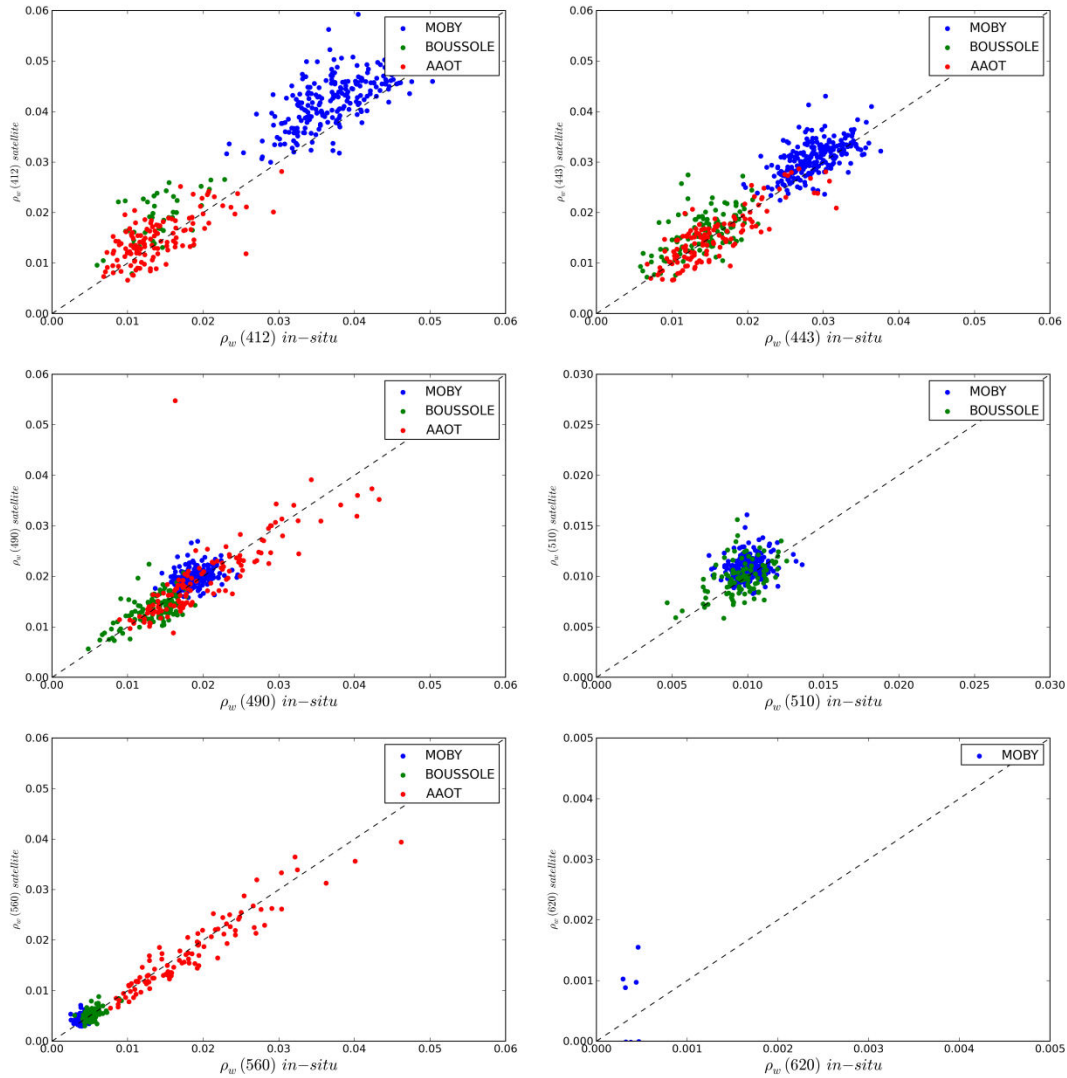


Figure 37 Validation of marine reflectance at MOBY, BOUSSOLE and AAOT with new implementation when activating NIR vicarious calibration

3.6.4 Discussion

Our tests have demonstrated the new implementation to be more robust to radiometry, while keeping all elements of previous BPAC modelling. We emphasize in particular that there is no need to update any LUT or auxiliary parameter. Regarding practical consideration, computational time is very similar: on a single 3GHz core, processing water pixels of the Amazon scene (mixing very turbid and clear waters) takes 119 seconds for current implementation versus 111 seconds for 3rd reprocessing algorithm; time is respectively 72 seconds versus 71 seconds for the water pixels of the Mediterranean scene.

Our results suggest two possible strategies for the vicarious calibration:

- Either keep 3rd reprocessing NIR vicarious calibration. This is probably not the optimal choice as resulting marine reflectance biases differ among validation sites and would produce heterogeneous visible gain; the alternative BPAC is still robust and would improve image quality and number of valid data on coastal areas.
- Or deactivate NIR vicarious calibration (or change it), considering that new BPAC can deal with NIR radiometric uncertainty. This would yield to consistent biases in the visible and a single set of vicarious visible gains would be suited for different water types. This is not (less) the case with 3rd reprocessing BPAC implementation.

4. Parameter Description

Symbol	Descriptive Name	I/O	Range/Reference/Remarks
$t([705,775,865,885], \theta_v, \theta_s, \Delta_\phi)$	Atmospheric diffuse total transmittance	I	Calculated Internally
$F(\lambda, a, bb_w, bb_p, \theta_v, \theta_s, \Delta_\phi)^1$	Water reflectance above surface factor - polynomials	I	Database Lookup Table
$a(TSM)$	Sediment absorption	I	Database Lookup Table
$b(TSM)$	Sediment backscatter	I	Database Lookup Table
c	Aerosol extrapolation parameter	-	Calculated Internally
$\rho_{as}([705,775,865], \theta_v, \theta_s, \Delta_\phi)$	Single scattering reflectance	I	From Rayleigh Correction
$\rho'_{as}([705,775,865], \theta_v, \theta_s, \Delta_\phi)$	Single scattering corrected reflectance	O	From Iterative Procedure
$\varepsilon(705,865, \theta)$	ρ_{rc} Ratio	-	Calculated Internally
$\varepsilon(775,865, \theta)$	ρ_{rc} ratio	-	Calculated Internally
TSM	Sediment load	-	From Procedure
θ_s	Solar zenith angle	I	From Navigation
Δ_ϕ	Azimuth difference	I	From Navigation
θ_v	Viewing angle	I	From Navigation
$\theta \equiv [\theta_v, \theta_s, \Delta_\phi]$	Viewing / solar angles	-	Naming Convention

4.1.1 Error Budget Estimates

Within Lavender *et al.* (2005) a set of simulated ρ_{rc} data were generated to test the BPAC iterative inversion method. The simulated data had a uniformly distributed set of viewing geometries, TSM concentration varied randomly between 0.1 and 200 g m⁻³ and $\rho'_a(865)$ was allowed to vary uniformly between 0.005 and 0.030. Varying amounts of noise (between 0 and 5%) were introduced to the modelled ρ_{rc} values for NIR bands to simulate absolute SeaWiFS measurement uncertainties. The retrieval performance was excellent when there was

no measurement noise: the mean difference was <0.2%, root-mean-square (RMS) difference was ~10% and over 95% of the retrievals were within 20% of the actual value. At 0.5% noise, the RMS difference increased to ~30% and less than 70% of the retrievals were within 20%. At 5% noise, the RMS error in the retrieval was more than 25% and <30% of the retrievals were within 20% of the actual values.

4.1.2 Practical Considerations

The algorithm requires LUTs and is performed on a pixel-by-pixel basis.

4.1.3 Sensitivity to IOPs

Results (e.g. Bale *et al.*, 1994) show that although the exact value of TSM iterated within the turbid water correction procedure may vary according to sediment properties, the relationships between the remote sensed reflectances are robust and independent of sediment type.

4.1.4 Output Product

BPAC products are only internal and not stored in standard MERIS Level2 files.

TOA marine reflectances at 779 and 865 nm are used for the downstream clear water atmospheric correction. Note that these reflectance can be negative because they come from the correction of the signal for Rayleigh and aerosol (positive reflectance), through an optimisation algorithm. This has no consequence, as the downstream path reflectance is defined by

$$\begin{aligned}
 \rho_{path}(\lambda) &= \rho_{GC}(\lambda) - t(\lambda)\rho_{WC2}(\lambda) \\
 &= \rho_{GC}(\lambda) - (\rho_{RC}(\lambda) - \rho_{as}(\lambda)) \\
 &= \rho_R(\lambda) + \rho_{as}(\lambda)
 \end{aligned}$$

TSM is used for Case 2 flagging (see next section) and is estimated by:

$$TSM = bb_p(775) / bb_p^*(775)$$

Note that a number of intermediate variables are available as netCDF outputs through the ODESA software (Optical Data processor of the ESA, <http://earth.eo.esa.int/odesa/>), e.g. TSM_BR, T_RHO_W_C2...; their description / definition can be found in the corresponding MERIS DPM.

4.1.5 Derived flags

Two flags, derived by the BPAC, are written in the MERIS Level-2 product: BPAC_ON and CASE2_S, described below.

Because the algorithm is currently turned on at all times (i.e. for all pixels), BPAC_ON flag indicates effective activation of the BPAC: it is only false if pre-processing fails, namely if Rayleigh correction yields to negative signal.

The CASE2_S flag, which indicates high scattering, is raised when the TSM calculated here above is greater than a threshold. In the MERIS 3rd reprocessing, the threshold was set to 0.75mg.l⁻¹. However it should be noted that this flag reflects scattering in the NIR and as such does not strictly refer to the Case 1 / Case 2 distinction,

since the flag can be raised by high levels of phytoplankton in mesotrophic waters. In the 4th reprocessing, the new BPAC minimisation algorithm generally yields higher TSM, even over clear waters, and needs a revised threshold. Indeed the bb_p may compensate for any source of scattering not properly corrected, like white caps or Sun glint, which does not follow an atmospheric shape. An example is shown in Figure 38 over the South Pacific Gyre, where TSM can now reach values larger than $1.\text{mg.l}^{-1}$ over the glint (North-East region).

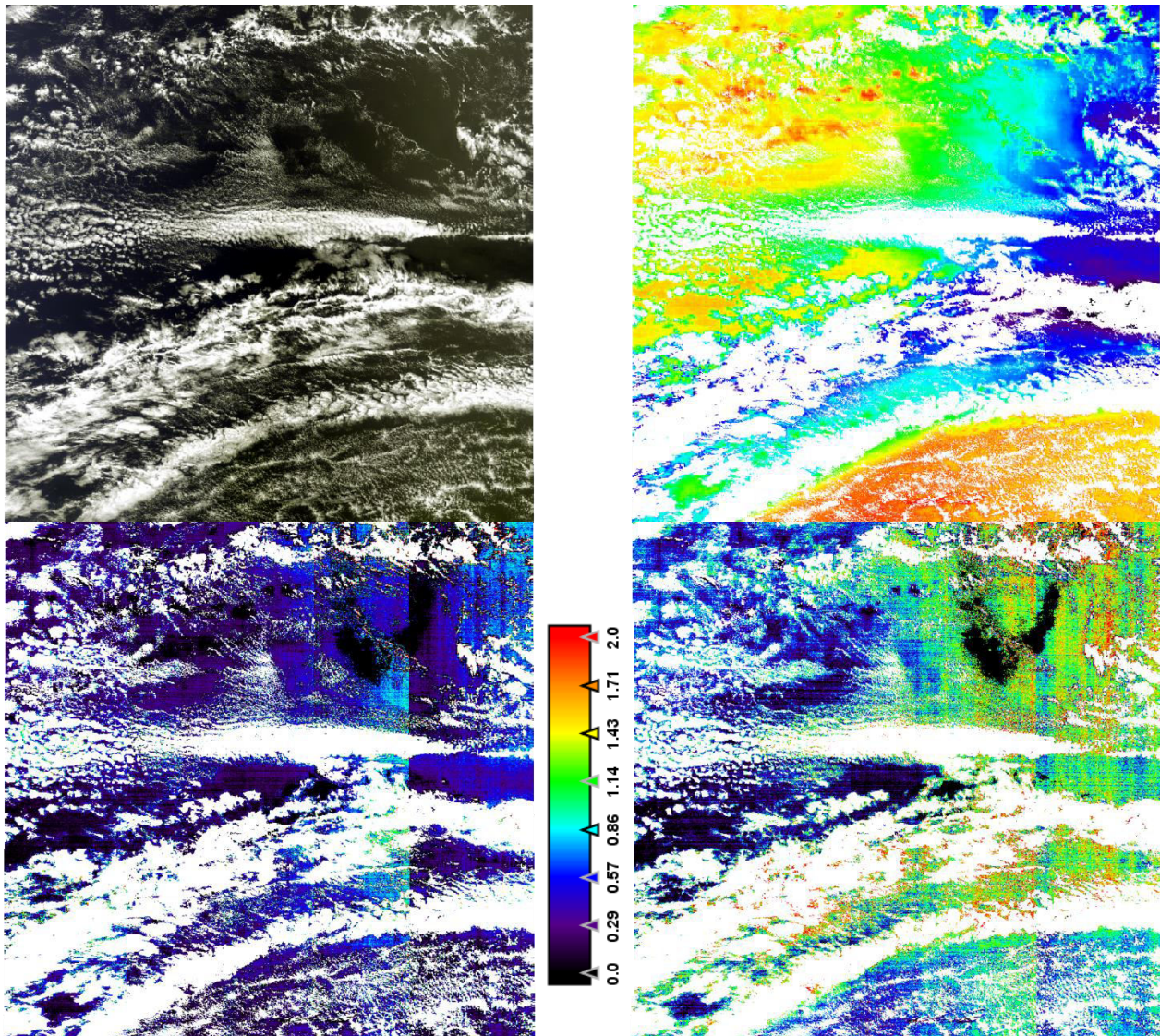


Figure 38 Example of BPAC inversion over the Shouth Pacific Gyre. Top left: RGB image of the Level-1 data. Top right: water vapour transmittance at 709 nm. Bottom: TSM retrived by 3rd (left) and 4th (right) reprocessing BPAC.

As already explained in section 3.5.4, the water vapour transmittance is erroneously low over the glint, of easily 3%. As a consequence, the ρ_{gc} and ρ_{RC} signal are erroneously too high at 709 nm. This affects the bb_p , but not the aerosol content thanks to the residual of the optimisation.

An extended analysis over the MOBY and BOUSSOLE site is provided on Figure 39. Clearly, the previous threshold of 0.75mg.l^{-1} is essentially reached when the pixels are impacted by HIGH GLINT, UNCORRECTED_GLINT (defined by HIGH_GLINT AND NOT MEDIUM_GLINT) and CLOUD_AMBIGUOUS (dotted line). These conditions are outside the domain of applicability of BPAC and should not artificially raise the CASE_2S flags. In the 4th reprocessing, the threshold has thus been increased to 1.5mg.l^{-1} (dashed line); furthermore the CASE_2S flag is never raised in case of CLOUD_AMBIGUOUS or UNCORRECTED_GLINT:

CASE2_S = 1 if SPM > 1.5 AND NOT CLOUD_AMBIGUOUS AND NOT (HIGH_GLINT AND NOT MEDIUM_GLINT)

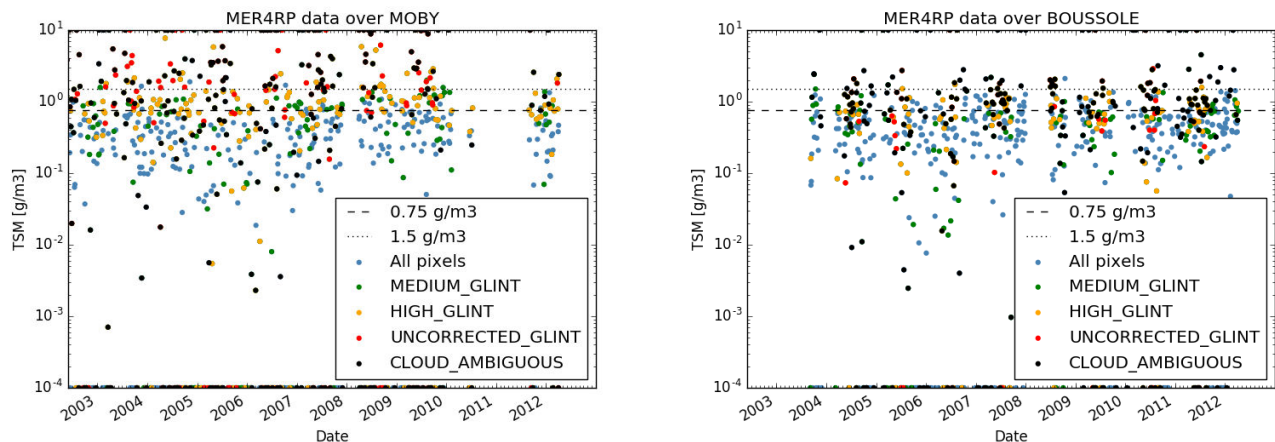


Figure 39 TSM computed by 4th reprocessing BPAC over the MOBY (left) and BOUSSOLE (right) sites. Colours depict the 4th reprocessing flags (see legend).

5. Assumptions and Limitations

At present, knowledge of NIR absorption is limited and needs to be improved using Mie modelling. Alternatively there could be a try to inverse specific particulate absorption (future work). Also white scatterers are not currently parameterised.

A deeper evolution of the BPAC could also concern the atmospheric model, e.g. consider a polynomial law to better take into account multiple scattering.

 <p>European Space Agency</p>	<h1>MERIS</h1>	<p>Doc: MERIS ATBD 2.6 Name: Case II.S Bright Pixel Atmospheric Correction Issue: 5.3 Release Date: 31 March 2017 Page: 73</p>
--	----------------	---

6. Acknowledgements

We are grateful to the team at ESA, ACRI and ARGANS for the MERMAID facility (<http://hermes.acri.fr/mermaid>) and we particularly acknowledge the following PIs whose in situ data are used in present validation:

- Giuseppe Zibordi (Joint Research Center, Italy) for the AAOT dataset (Zibordi et al. 2009a, Zibordi et al. 2009b);
- David Antoine (Laboratoire d'Océanographie de Villefranche, France) for the BOUSSOLE dataset (Antoine et al. 2006, Antoine et al. 2008);
- Ken Voss (University of Miami) and Kent Hughes (NOAA) for the MOBY dataset (Clark et al. 2003);
- Jeremy Werdell (NASA) for the NOMAD dataset (Werdell and Bailey 2005) together with contributing PIs: Larry Harding (University of Maryland, US), Antonio Mannino (NASA), Ajit Subramaniam (University of Maryland, US), Dariusz Stramski (University of California, US), Greg Mitchell (University of California, US), William Balch (Bigelow Laboratory for Ocean Sciences, US), Frank Muller-Karger (University South Florida, US), Ru Morrison (Woods Hole Oceanographic Institution, US), Zhongping Lee (Naval Research Laboratory), Ken Carder (Professor Emeritus University South Florida, US), Norman Nelson (University of California, US), Richard Gould (Naval Research Laboratory, US), Robert Arnone (Naval Research Laboratory, US) and Stan Hooker (NASA).

Results on real MERIS data were obtained by implementing the algorithm into the ODESA software (Optical Data processor of the ESA, <http://earth.eo.esa.int/odesa/>).

7. References

- Antoine, D. and A. Morel, 1999. A multiple scattering algorithm for atmospheric correction of remotely-sensed ocean colour (MERIS instrument): principle and implementation for atmospheres carrying various aerosols including absorbing ones. *International Journal of Remote Sensing*, 20(9): 1875-1916.
- Antoine, D., M. Chami, H. Claustre, F. D'Ortenzio, A. Morel, G. Bécu, B. Gentili, F. Louis, J. Ras, E. Roussier, A. J. Scott, D. Tailliez, S. B. Hooker, P. Guevel, J.-F. Desté, C. Dempsey and D. Adams, 2006. BOUSSOLE: a joint CNRS-INSU, ESA, CNES and NASA Ocean Color Calibration And Validation Activity. *NASA Technical memorandum N° 2006 – 214147*.
- Antoine, D., P. Guevel, J.-F. Desté, G. Bécu, F. Louis, A.J. Scott and P. Bardey, 2008. The «BOUSSOLE» buoy, a new transparent-to-swell taut mooring dedicated to marine optics: design, tests and performance at sea, *Journal of Atmospheric and Oceanic Technology*, 25, 968-989.
- Arnone, R.A., Martinolich, P., Gould, R.W., Stumpf, R. and S. Ladner, 1998. Coastal optical properties using SeaWiFS. In *SPIEE Ocean Optics XIV*, edited by S. Ackleson and Cambell.
- Babin, M., A. Morel, V. Fournier-Sicre, F. Fell and D. Stramski, 2003. Light scattering properties of marine particles in coastal and oceanic waters as related to the particle mass concentration. *Limnology and Oceanography*, 48, 843-859
- Bale, A.J., Tocher, M.D., Weaver, R., Hudson, S.J. and J. Aiken, 1994. Laboratory measurements of the spectral properties of estuarine suspended particles. *Netherlands Journal of Aquatic Ecology*, 28: 237-244.
- Blondeau-Patissier, D., Tilstone, G.H., Martinez-Vicente, V. and G.F. Moore, 2004. Comparison of bio-physical marine products from SeaWiFS, MODIS and a bio-optical model with in situ measurements from Northern European waters. *Journal of Optics A: Pure and Applied Optics*, 6: 875–889.
- Bricaud, A., A. Morel, M. Babin, K. Allali And H. Claustre, 1998. Variations of light absorption by suspended particles with Chlorophyll-a concentration in oceanic (case 1) waters: Analysis and implications for bio-optical models, *Journal of Geophysical Research*, 103: 31033-31044
- Clark, D. K., M. A. Yarborough, M. E. Feinholz, S. Flora, W. Broenkow, Y. S. Kim, B. C. Johnson, S. W. Brown, M. Yuen, and J. L. Mueller, 2003. MOBY, A Radiometric Buoy for Performance Monitoring and Vicarious Calibration of Satellite Ocean Colour Sensors: Measurements and Data Analysis Protocols. In *Ocean Optics Protocols for Satellite Ocean Colour Sensor Validation*, *NASA Technical memorandum 2003-211621/Rev4*, VolVI, 3-34 (Eds J. L. Muller, G. Fargion and C. McClain). Greenbelt, MD.: NASA/GSFC.
- Gordon, H.R, 1979). Diffuse reflectance of the ocean: the theory of its augmentation by chlorophyll a fluorescence at 685 nm. *Applied Optics*, 18: 1161-1166.
- Gordon, H.R., and M. Wang, 1994. Retrieval of water-leaving radiances and aerosol optical thickness over the oceans with SeaWiFS: a preliminary algorithm. *Applied Optics*, 33: 443-452.
- Kou, L., D. Labrie, et al. 1993. Refractive indices of water and ice in the 0.65-2.5 μm spectral range. *Applied Optics* 32: 3531-3540.

- Lavender, S.J., 1996. Remote Sensing of Suspended Sediment. PhD Thesis. Institute of Marine Studies, University of Plymouth and in collaboration with Plymouth Marine Laboratory.
- Lavender, S.J., Pinkerton, M.H., Moore, G.F., Aiken, J and D. Blondeau-Patissier, 2005. Modification to the Atmospheric Correction of SeaWiFS Ocean Colour Images over Turbid Waters. *Continental Shelf Research* 25: 539-555.
- Lerebourg, C., Mazeran, C., Huot, J.-P. and D. Antoine, 2011, Vicarious adjustment of the MERIS Ocean Colour Radiometry, MERIS ATBD 2.24, Issue 1.0
- Lindstrot RL, 2011, DUE GlobVapour ATBD D7, Ref. GlobVapour_D07_ATBD_L2_MERIS_v2.1.
- Mobley, C.D., 1995. *Hydrolight 3.0 Users Guide*, SRIRI Project 5632. SRI International, Menlo Park, CA, United States.
- Moore, G.F., Aiken, J., and S.J. Lavender, 1999. The atmospheric correction of water colour and the quantitative retrieval of suspended particulate matter in Case II waters: application to MERIS. *International Journal of Remote Sensing* 20(9): 1713-1733.
- Morel, A. and B. Gentili, 1993. Diffuse reflectance of oceanic waters, II. Bidirectional aspects. *Applied Optics* 32(33): 6864–6879.
- Morel, A., 1974. Optical properties of pure seawater. *Optical aspects of Oceanography*. Ed Jerlov, N.G. and Nielsen, S.E. Academic Press: London.
- Petzold, T.J., 1972. Volume scattering functions for selected ocean waters. *Scripps Inst. Oceanogr. Rep.* 72-78: 79.
- Pope, R.M. and E.S Fry, 1997. Absorption spectrum (380–700 nm) of pure water, III. Integrating cavity measurements. *Applied Optics*, 36: 8710–8723.
- Press, W.H., Teukolsky, S.A., Vetterling, W.T. and B.P. Flannery, 1992. *Numerical Recipes in C*, Second Edition, Cambridge University Press, 994.
- Ruddick, K. G., V. De Cauwer, et al. 2006. Seaborne measurements of near infrared water-leaving reflectance: The similarity spectrum for turbid waters. *Limnology and Oceanography* 51: 1167-1179.
- Ruddick, K.G., Ovidio, F. and M. Rijkeboer, 2000. Atmospheric correction of SeaWiFS imagery for turbid and inland waters. *Applied Optics* 39: 897-912.
- Siegel, D.A., Wang, M., Maritorena, S. and W. Robinson, 2000. Atmospheric correction of satellite ocean color imagery: the black pixel assumption. *Applied Optics* 39: 3582-3591.
- Stumpf, R.P., Arnone, R.A, Gould, R.W., Martinolich, P. and V. Ransibrahmanakul, 2002. A partially-coupled ocean-atmosphere model for retrieval of water-leaving radiance from SeaWiFS in coastal waters. In *Algorithm Updates for the Fourth SeaWiFS Data Reprocessing*, Vol. 22, S. B. Hooker and E. R. Firestone, eds. (NASA Tech. Memo. 2002-206892, NASA Goddard Space Flight Center, Greenbelt, MD, 2003).
- Wang, M. and W. Shi, 2005. Estimation of ocean contribution at the MODIS near-infrared wavelengths along the east coast of the U.S.: Two case studies. *Geophysical Research Letters* 32: L13606.

- Werdell, P. J. and S. W. Bailey, 2005. An improved bio-optical data set for ocean color algorithm development and satellite data product validation. *Remote Sensing of Environment*, 98(1), 122-140.
- Whitlock, C.H., Poole, L.R., Usry, J.W., Houghton, W.M., Witte, W.G., Morris, W.D. and E.A. Gurganus, 1981. Comparison of reflectance with backscatter and absorption parameters for turbid waters. *Applied Optics*, 20: 517-522.
- Zagolski, F., and R. Santer, 2016. Pressure adjustment over water in the MERIS level-2 processing chain (MEGS-9). ParBleu/ULCO-ATBD for ESA/MERIS Ground-Segment (Issue 1, Rev. 6): 34p.
- G. Zibordi, B. Holben, I. Slutsker, D. Giles, D. D'Alimonte, F. Mélin, J.-F. Berthon, D. Vandemark, H. Feng, G. Schuster, B. Fabbri, S. Kaitala, J. Seppälä, 2009. AERONET-OC: a network for the validation of Ocean Color primary radiometric products. *Journal of Atmospheric and Oceanic Technology*, 26, 1634-1651.
- G. Zibordi, J.- F.Berthon, F.Mélin, D. D'Alimonte and S.Kaitala, 2009. Validation of satellite ocean color primary products at optically complex coastal sites: northern Adriatic Sea, northern Baltic Proper and Gulf of Finland. *Remote Sensing of Environment*, 113, 2574-2591.

8. Appendix A - Chlorophyll Absorbance and Fluorescence

Preliminary data from hyper-spectral radiometer measurements, where there is a strong fluorescence peak, indicate that there is potential contamination of the 705 nm band by the fluorescence signal. However, quantitative analysis of these results awaits an adequate stray-light correction scheme for these instruments. At present we assume that the Gaussian formulation of Gordon (1979) is appropriate.

Figure 40 shows the normalised chlorophyll fluorescence and absorption parameters described in the MERIS RMD. The absorption curve is from Bricaud *et al* (1998) and the fluorescence curve is from the standard Gaussian in the MERIS RMD. Also shown for reference is the shifted absorption curve, since this may better match the chlorophyll fluorescence shown *in vivo*. It can be seen that there is significant overlap at the 705 nm band. The extra reflectance at 705 nm, due to fluorescence rather than particle scattering, results in an overestimate of $\rho_w(\text{NIR})$ and the consequent error in the BPAC.

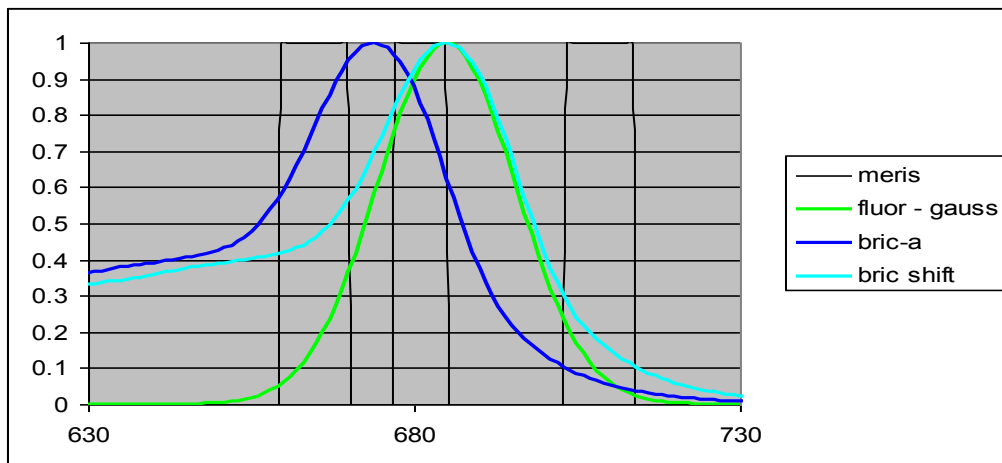
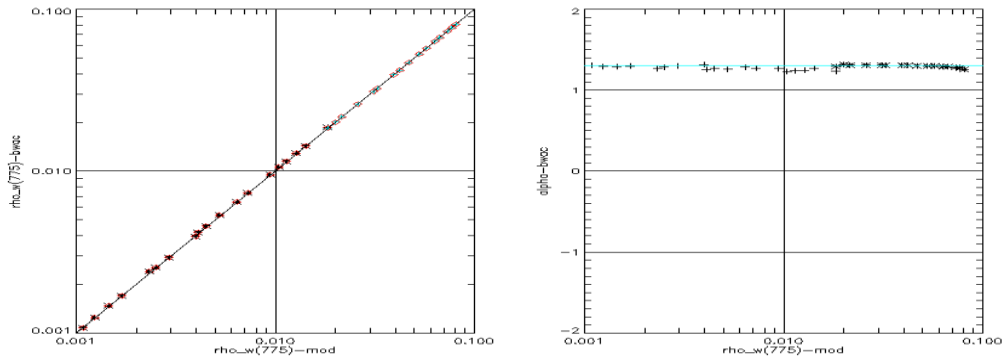
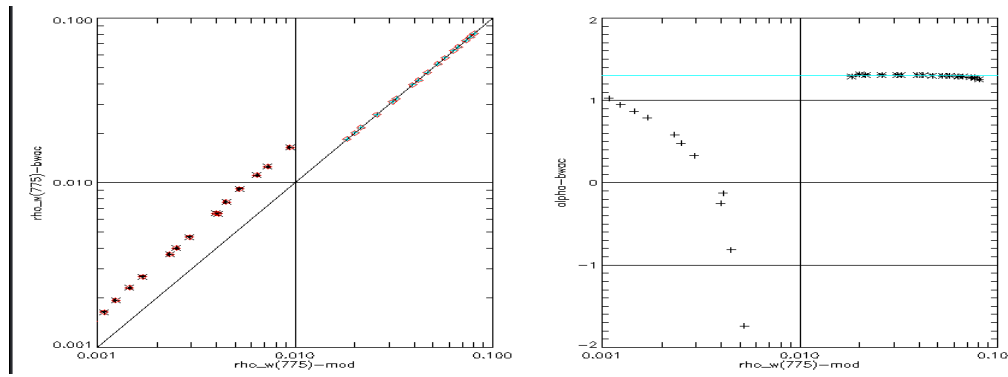


Figure 40: Chlorophyll fluorescence and absorption for MERIS Bands

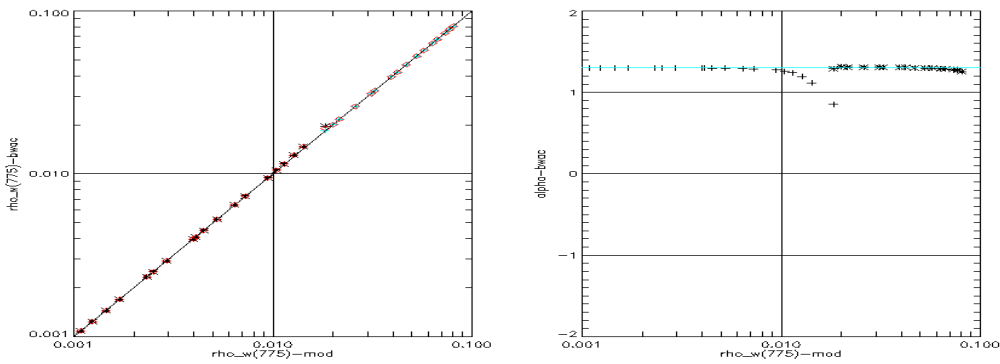
The effect can be corrected by using the first estimate of $bb_p(705)$. It's assumed that there is no fluorescence and thus the corrected reflectance $\rho'_w(\lambda)$ is equal to $\rho_w(\lambda)$ and that initially $a_p(670)$ is zero. The solution is iterated until the relative change in $\rho_f(685)$ is less than 0.01%. If $\rho_f(685) \leq 0$ then the calculation is terminated since fluorescence correction is unnecessary. The $bb_p(705)$ estimated from the fluorescence corrected reflectance is then returned to the BPAC. The iterative procedure typically takes around 5 iterations.



a) The nominal BPAC Correction – without natural fluorescence



b) The nominal BPAC Correction – with natural fluorescence



c) The BPAC Correction – with the fluorescence corrections and natural fluorescence

Figure 41: Effects of natural fluorescence on BPAC

$a_p(670)$ is estimated as follows:

$$bb_p(670) = bb_p^*(670) \cdot bb_p(705) / bb_p^*(705) \quad (F1)$$

$$a(670) = a_p(670) + a_w'(670) + bb_p(670) \cdot a_{bb}^*(670) \quad (F2)$$

$$F' = F'(670, \theta_v, \theta_s, \Delta\Phi, a(670), bb_w(670), bb_p(670)) \quad (F3)$$

$$a_p(670) = [bb_p(670) + bb_w(670)] \cdot [F' / \rho_w'(670) - 1] - a_w'(670) - bb_p(670) \cdot a_{bb}^*(670) \quad (F4)$$

$\rho_w'(685)$ is estimated as follows:

$$bb_p(685) = bb_p^*(685) \cdot bb_p(705) / bb_p^*(705) \quad (F5)$$

$$a_p(685) = a_p^*(685) \cdot a_p(670) / a_p^*(670) \quad (F6)$$

$$a(685) = a_w'(685) + a_p(685) + bb_p(685) \cdot a_{bb}^*(685) \quad (F7)$$

$$F' = F'(685, \theta_v, \theta_s, \Delta\Phi, a(685), bb_w(685), bb_p(685)) \quad (F8)$$

$$\rho_w'(685) = F' \cdot [bb_p(685) + bb_w(685)] / [bb_p(685) + bb_w(685) + a(685)] \quad (F9)$$

The fluorescence is estimate as follows, assuming $K(\lambda) \approx a(\lambda)$:

$$\rho_f(685) = \rho_w(685) - \rho_w'(685) \quad (F10)$$

$$\rho_f(\lambda) = \rho_f(685) \cdot Lfn(\lambda) \cdot E0(685) \cdot a(685) / Lfn(685) \cdot E0(\lambda) \cdot a(\lambda) \quad (F11)$$

where $Lfn(\lambda)$ is the normalised fluorescence spectra derived from the Gaussian, and since $E0(\lambda)$ is a constant, the fluorescence spectrum that is adjusted for $E0(\lambda)$, $\rho fn(\lambda)$ can be used.

The fluorescence corrected reflectance $\rho_w'(\lambda)$ is derived as:

$$\rho_w'(\lambda) = \rho_w(\lambda) - \rho_f(\lambda) \quad (F12)$$

From this a new estimate of $bb_p(705)$ is calculated according to section 0 and iteration resumes at (F1).

Table 1 shows provisional values for the relative fluorescence height and for the chlorophyll specific absorption.

Band(nm)	$Lfn(\lambda)$	$\rho fn(\lambda)$	$a_p(\lambda)$
670	0.1884	0.1810	0.3129
685	0.9135	0.9135	0.2053
709	0.1448	0.1514	0.0176

Table 1: Fluorescence height and phytoplankton absorption

SUMMARY SHEET

Product Name	Case II.S (Sediment) Bright Water Correction.
Product Code	Internal to ocean atmospheric correction.
Product Level	2
Product Parameters	
Spatial Coverage	Coastal waters, coccolithophore blooms and mesotrophic waters.
Packaging	
Units	Reflectance – dimensionless, TSM g.m^{-3}
Range	
Sampling	
Resolution	Any
Accuracy	Estimates from tests with CASI data indicated that the accuracy is within the radiometric calibration of CASI ($\pm 5\%$). For simulated data and 5% noise, the RMS error in the retrieval was more than 25% and <30% of the retrievals were within 20% of the actual values (see Section 4.1.1).
Geo-location Requirements	Angle of View
Format	Internal I/O
Appended Data	
Frequency of Generation	As per atmospheric correction.
Size of Product	N/A [16bit if TSM output implemented]
Additional Information	

Identification of Bands	[705,775,865,895]
Assumptions on MERIS Input Data	Rayleigh Corrected and gaseous absorption corrected.
Output Data	$\rho_{as}[705,775,865,895]$, <i>TSM estimate for flagging.</i>
Identification of Ancillary and Auxiliary Data	Temperature climatology and MERIS actual wavelength for smile and temperature aw correction.
Assumptions of Ancillary and Auxiliary Data	Temperature +/- 2°C